THE UNIVERSITY *of* EDINBURGH

Additive Engineering Mechanisms for Antimony Chalcogenide Solar Cells

Matthew Sutton

A thesis submitted for the degree of Doctorate of Philosophy at

The University of Edinburgh

December 2024

Acknowledgements

This PhD has been quite a journey, and I have definitely grown immensely as a person because of the experiences I have had. While a lot of my work has necessarily been independent, there are a large number of people who enabled and supported me during this work, and who without which, it would not be what it is today.

Firstly, I would like to thank Prof. Tayebeh Ameri for the opportunity to embark on this journey, and for guiding me throughout the PhD, while also giving me the independence and confidence to make the research what I wanted it to be. While at first, I found it tough not having direct and detailed instruction, I very quickly reached an equilibrium and am now able to work fully independently on whatever task comes my way, which is an invaluable skill.

Thanks to Prof. Neil Robertson for the opportunity of performing my Masters project with him and his group. It was that opportunity which led to my introduction to Tayebeh and this PhD project. Additionally, the use of the various laboratories and the involvement in his group enabled this ambitious project to be performed.

Thanks also to Dr. Jane Blackford, who was my third supervisor, but whom I know much more closely through my teaching responsibilities in the Materials 2 engineering course. I am very glad to have worked on this course particularly, as the unique and brilliant teaching style Jane used not only enabled me to use the chemical knowledge I had, but also to learn a lot about materials and how interesting they are from both the other team members and the students themselves. The opportunity to work in a more course-organisation style role also gave me experience which I can now bring forward into the world of work, for which I am very grateful.

Thanks also to Prof. Prashant Valluri for additional supervision provided after Tayebeh had returned to Germany.

Thanks to Dr. Amir Amin Abs Yousefi and Shaharyar Shafiq Waliullah for their assistance in setting up a complicated (and often frustrating) photoconductor and EQE setup.

Thanks to all of the technicians for their help with equipment, particularly Dr. Justin Elliott for help setting up my glovebox, Dr. Richard York and Dr. Juraj Bella for help with NMR measurements, Dr. Gary Nichol for help with XRD measurements, Dr. Andrei Gromov for help

with Raman measurements and Dr. Nicola Cayzer for help with SEM and EDS measurements. A particularly big thank you to the School of Chemistry technicians George Steedman and Lloyd Mitchell, who saved me on many a last-minute-panic occasion during equipment setup and maintenance, and to whom I became infamous for the multitude of issues my equipment was facing.

Thanks to both the Robertson group and Ameri group, past and present, for giving me someone to talk through my research problems with and some great chats and good laughs to break up the work.

I would also like to thank the School of Engineering for funding and supporting my research through Tayebeh's staff seed fund, which allowed for me to perform my research without financial worry.

Finally, I would like to thank my family for their ongoing support and encouragement, my friends for giving me perspective on my PhD problems (many of them were going through the same things), and to my partner, Eleanor, for putting a positive spin on things when the research was feeling hopeless.

Abstract

Antimony chalcogenide solar cells are an attractive thin film solar technology with a tuneable bandgap, high inherent stability and a large absorption coefficient. They are often solution-processed, allowing for the easy employment of chemical additives. Though many additives have already been utilised, the underlying chemical mechanisms are often poorly understood. The formation of unwanted side phases, most notably Sb_2O_3, are also largely not understood. Here, the chemical mechanism of an additive of proven efficacy, EDTA, is investigated through the use of NMR spectroscopy and a solution-based chemical aggregation test, as well as the use of various techniques including powder-XRD, SEM and Raman spectroscopy on Sb_2S_3 films formed using EDTA. These tests demonstrated that EDTA can control the deposition of Sb_2S_3 films, while suppressing the formation of the undesired Sb_2O_3 side-phase. The solution-based chemical aggregation test was further developed into a screening process to find additives which rival and exceed EDTA. After the discovery of successful additives using this screening process, a chemical mechanism for the suppression of Sb_2O_3 formation was found by correlating improvement of solar cell performance with the pH of the additive. The mechanism proposed in the literature for the control of film deposition by EDTA was that through the sequestration of Sb^{3+}, EDTA was effectively changing the deposition mechanism from per-nanoparticle to per-ion deposition, thus forming more compact and large crystal grains. By relating the capability of an additive to bind Sb^{3+} to its relevant solar cell performance, this mechanism is further evidenced and expanded. The deeper understanding of these additive mechanisms afforded by this investigation will allow for more focussed and informed development of additives for efficient antimony chalcogenide solar cells in the future, particularly those using a benign and abundant TiO_2 electron transport layer.

Lay Summary

Climate change is causing more extreme and frequent weather events worldwide, and energy generation from fossil fuels is a large contributor to the greenhouse gases which are causing climate change. By utilising clean, renewable sources of energy, emissions of greenhouse gases can be reduced, thus limiting the weather effects caused. Solar energy is the most abundant energy source we have, with the sun providing abundant energy to the side of the Earth which is in daylight. Solar energy can be captured by a technology called a solar cell. When several solar cells are combined, they make up the panels which we see on rooftops and in solar farms. Silicon is an optimal material for solar conversion, as it can achieve very high power conversion efficiencies (the ratio of incoming solar energy to output electrical energy) and output a stable amount of power for decades. However, due to an inherent property known as an 'indirect bandgap', silicon cells require a greater amount of material to absorb all of the incoming light, and this means that they are too heavy to use in electric vehicles.

Antimony chalcogenides are a family of materials consisting of the general chemical formula of two antimony atoms and three of any mixture of sulfur or selenium atoms. They are a promising material to solve the above issue with silicon cells, as they have a 'direct bandgap', allowing them to be orders of magnitude thinner than silicon, whilst still being highly stable. They also absorb in a different colour range than silicon, allowing for the 'sandwiching' of the two technologies in a tandem structure to achieve even higher efficiencies than either one on its own. The current issue with antimony chalcogenides is that despite them theoretically reaching the maximum thermodynamic limit of power conversion efficiency, the value currently achieved is less than half that of silicon. Each of the current leading solar cell configurations based on antimony chalcogenides utilise different chemical additives in a hydrothermal synthesis procedure, whereby the antimony chalcogenide starter materials are mixed together with the additive in water and then heated in a pressurised chamber to form a thin film of the antimony chalcogenide. Because of the prevalence and success of the use of chemical additives in antimony chalcogenide solar cells, particularly using this hydrothermal process, the study of additives and their working mechanisms are of great importance for finding ways to improve the power conversion efficiency of antimony chalcogenide solar cells.

This thesis investigates the underlying mechanisms by which one of these additives, EDTA, works, and using that understanding, discover other additives which work by the same mechanism. Then, by correlating the structures of the additives with those with similar behaviour, detailed chemical mechanisms underlying their operation are proposed and justified. Acidic additives were found to lead to a suppression of the unwanted side-product antimony oxide (which is known to decrease power conversion efficiency), while additives with a basic pH conversely promoted the growth of antimony oxide. However, too high an acidity damaged the film. Additionally, the greater the ability of the additive to chemically attach to antimony, the better the additive performed. With an understanding of these dynamics, the high performance of EDTA is well explained. It is very effective at binding to antimony and is acidic enough to suppress antimony oxide, without being so acidic as to damage the antimony chalcogenide film. Several additional additives were also explored, and some achieved even higher power conversion efficiency than EDTA. The additives which achieved the highest efficiencies had similar acidity to EDTA, but a greater ability to bind to antimony than EDTA.

An effective additive must not damage the antimony chalcogenide film or cause the formation of unwanted antimony oxide, and it must help in forming a high quality and efficient antimony chalcogenide solar cell. The work done here paves the way for future additive development for antimony chalcogenide solar cells, as it highlights both the importance of the pH of the additive, and the importance of the additive's capability to bind to antimony in fulfilling both of these goals.

Table of Contents

List of Abbreviations

Common Solar Cell Terms

CIGS	$Cu(In,Ga)Se_2$
c-Si	Crystalline silicon
ETL	Electron transport layer
FF	Fill factor
HTL	Hole transport layer
MPP	Maximum power point
PCE	Power conversion efficiency

Techniques

AFM	Atomic force microscopy
CBD	Chemical bath deposition
EDS	Energy-dispersive X-ray spectroscopy
EQE	External quantum efficiency
HT	Hydrothermal
ICSD	Inorganic crystal structure database
J-V	Current density-voltage
NMR	Nuclear magnetic resonance
P-XRD	Powder X-ray diffraction
RP	Resultant powder
SEM	Scanning electron microscopy
SIMS	Secondary ion mass spectroscopy

TGA	Thermogravimetric analysis
XRD	X-ray diffraction
XRF	X-ray fluorescence

Reagents and Chemicals

1111E	1,1',1'',1'''-(ethane-1,2-diylbis(azanetriyl))tetrakis(propan-2ol)
12-ADA	12-Aminododecanoic acid
34910-P	3,4,9,10-Perylenetetracarboxylic dianhydride
4-n	4-nitrophenol
44D	4,4'-dithiobutyric acid
45-d-2-n	4,5-dimethyl-2-nitroaniline
AA	Acetic acid
CA	Citric acid
Creat	Creatinine
DETAP	Diethylenetriaminepentakis(methylphosphonic acid) solution
DGA	Diglycolic acid
ED	Ethylenediamine
EDTA	Ethylenediaminetetraacetic acid
FTO	Fluorine-doped tin oxide
LTA	L-(+)-Tartaric acid
NTA	Nitrilotriacetic acid
NTMP	Nitrilotris(methylenephosphonic) acid
PA	Pentetic acid

PAT	Potassium antimony tartrate
PFNB	Pentafluoronitrobenzene
PHA	Phosphoric acid
PMDTA	N,N,N',N',N'-Pentamethyldiethyldiethylenetriamine
SBA	Sebacic acid
Spiro	Spiro-OMeTAD
STS	Sodium thiosulfate
TEA	Triethanolamine
TETAH	Triethylenetetramine-N,N,N',N'',N''',N'''-hexaacetic acid

List of Symbols

B_0	External magnetic field
c	Speed of light in a vacuum
d	Diffraction spacing
δ	Chemical shift
e^-	Electron
E	Electric field
E_g	Bandgap
γ_N	Gyromagnetic ratio
h	Planck's constant
ħ	Reduced Planck's constant
h^+	Hole (absence of electron)
H	Spectral irradiance
I	Powder X-ray diffraction peak intensity
I	Spin quantum number
J	Coupling constant
J_{SC}	Short circuit current density
k	Boltzmann's constant
k_f	Bond force constant
λ	Wavelength
m	Mass
m_I	Orbital magnetic quantum number
M^+	Positively charged metal ion

μ	Effective mass
n	Ideality factor
n_d	Diffraction order
P	Power
ϕ	Photon flux
q	Electron charge
R_q	Roughness
R_s	Series resistance
R_{sh}	Shunt resistance
ν	Frequency
$\tilde{\nu}$	Wavenumber
ω	Angular frequency
T	Temperature
TC_{hkl}	Texture coefficient for reflection hkl
θ	Diffraction angle
V	Voltage
V_{OC}	Open circuit voltage

List of Figures

Figure 6.11: Number of oxygen atoms on additive available to bind to Sb^{3+} vs the average PCE of Sb_2S_3 solar cells made using that additive

List of Tables

1. Introduction

1.1. Climate Change and Energy Demand

In 1896, Prof. Svante Arrhenius showed that heat-absorbing gases, such as CO_2, have the ability to alter the temperature of the Earth's surface[1]. He explained that heat absorbing gases in the atmosphere will trap radiation in what we now know as a 'greenhouse effect', and that without this effect, the Earth's temperature would fall to around -200 °C. While this effect is necessary for our survival, it is also the cause of one of the greatest modern concerns; climate change. In 1956, Gilbert Plass published 'The Carbon Dioxide Theory of Climatic Change'[2], in which he explains that the Earth goes through a cyclic pattern of atmospheric CO_2 concentrations, leading to alternating glacial (ice age) and inter-glacial periods, and how this balance has recently been heavily skewed by anthropogenic sources of CO_2. Atmospheric CO_2 levels have sharply risen from 365 ppm in 2002 to over 420 ppm in 2024, leading to an approximate 0.5 °C increase in global surface air temperature in the same period[3]. This seemingly small change in average global temperature has already had myriad consequences including but not limited to rising sea levels, extreme weather events and the destruction of natural habitats[4, 5]. A large contributor of this CO_2 emission is energy production, particularly from fossil fuel sources[4, 5]. Therefore, 'cleaner' sources of energy are required, and one of these clean sources is solar energy conversion. We already make good use of solar energy, and it has been rapidly increasing in recent years, with global consumption of solar power reaching 4264 TWh (2.33% of total) in 2022, up from 3446 TWh (1.92% of total) the previous year[6, 7]. However, overall global power consumption is still increasing. Data centres (used for technologies such as search engines and artificial intelligence) on their own used 460 TWh in 2022, with that number projected to increase to 1000 TWh in 2026. This amount would account for nearly a quarter of all solar power consumption in 2022. Another sector which might utilise solar in the future is that of electric vehicles, which are projected to add 37 TWh to energy consumption in the EU alone between 2024-2026[8]. Evidently, a ramping up of solar production is required to meet this demand. Furthermore, technologies must be developed to allow for increased solar conversion efficiency per unit of weight, lower costs and/or easier manufacture.

1.2. Solar Power Generation

Solar power is generated via the excitation of an electron by an incoming photon to form an electron-hole pair known as an exciton. The device requires an internal electric field to guide the excited electron to an electrode, and to guide another electron from the other electrode to fill in the hole (in essence, moving the hole to that second electrode). By connecting the device to an external circuit, these charges create an electrical flow. The process is illustrated in *Figure 1.1*.

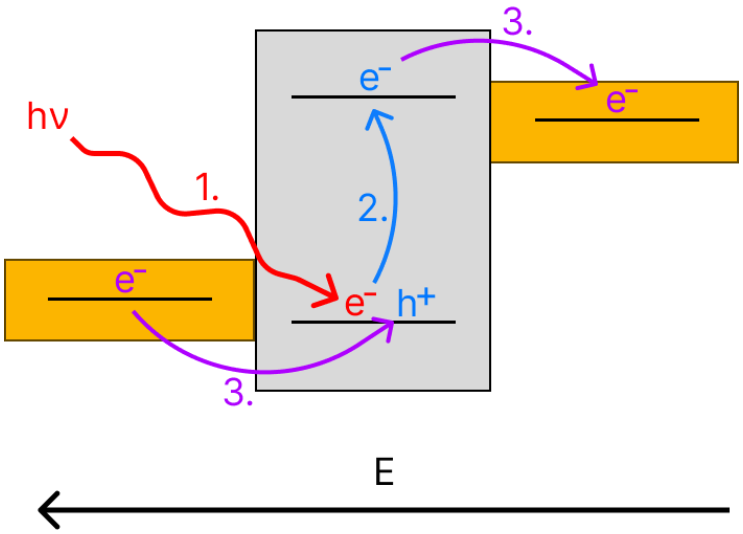

Figure 1.1: *Process of solar energy generation; 1. incoming solar radiation (h ν) is absorbed by an electron, 2. excitation of electron to form an exciton (e^--h^+ pair), 3. movement of electron and hole via internal electric field (E) to respective electrodes to generate electricity.*

1.2.1. Bandgap and Efficiency Limits

The energy of photons that a material can absorb depends on the gap between that material's occupied and unoccupied electronic energy levels. In semiconductors, the type of material used for solar energy generation, the minimum energy is given by its bandgap (E_g). E_g is the gap between the lowest energy level of the conduction band and the highest energy level of the valence band. E_g determines the wavelengths of light that a solar absorber is able to absorb. An incoming photon with energy less than E_g does not have the energy to excite an electron from the conduction to the valence band. E_g also helps to define the maximum thermodynamic limit of efficiency, known as the Shockley-Queisser limit. The Shockley-

Queisser limit for solar cells sits at ~33% efficiency for a solar cell with an E_g of approximately 1.3 - 1.4 eV[9].

A bandgap can either be direct or indirect, depending on the crystalline structure of the material you are dealing with. If the bandgap is direct, the transition of an electron from the valence band to the conduction band to form an exciton is relatively likely to occur, whereas an indirect bandgap makes this transition less likely to occur, requiring assistance from lattice vibrations (phonons) for it to absorb at the same energy as the direct bandgap equivalent. As a result, indirect bandgap materials need a thicker layer of material in order to absorb the same amount of light as direct bandgap materials. *Figure 1.2* shows an illustration of this effect.

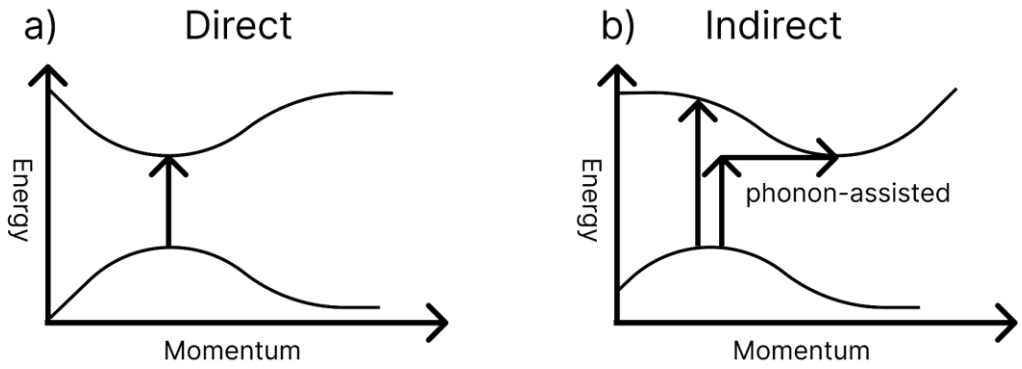

Figure 1.2: *Illustration of bandgap types; a) direct, which allows an easy transition, and b) indirect, which must have either higher energy, or transition by assistance from a lattice vibration (phonon).*

1.2.2. Charge Recombination

One of the reasons solar cell efficiencies are limited to ~33% by the Shockley-Queisser limit is charge recombination. When an exciton is formed, the charge carriers (electron/hole) may recombine together, or combine with another charge carrier generated as part of an exciton. When this happens, the charge that would have been extracted to generate electricity is lost. This energy can be released either radiatively or non-radiatively. Recombination is thermodynamically inevitable, so ideally all recombination within a solar cell will occur radiatively, as this radiation may once again be absorbed to produce another exciton. The

extent of recombination depends on the lifetime (how long before it recombines) and mobility (how fast it moves towards the electrode) of the charge carriers.

Three forms of recombination mechanisms exist, and are displayed in *Figure 1.3*. The first and simplest form of recombination is radiative, where the electron drops back down to the valence band edge, re-releasing the same amount of energy as was absorbed. The second for is trap-assisted recombination, also known as Shockley-Read-Hall. This is a non-radiative recombination where, by emitting radiation of lower energy than was absorbed, the charge carrier ends up at an energy level in between the conduction band and valence band, potentially becoming trapped. If this occurs, it eventually combines with another charge carrier. These intermediate energy levels arise from crystalline defects, or additional materials being present within the charge-generating material. The third and final form of recombination is Auger recombination, whereby the energy from one of the other two forms of recombination is instead given to another electron which moves to a higher excited state, then non-radiatively thermalises back down to the conduction band edge by dissipating energy into vibrational modes.

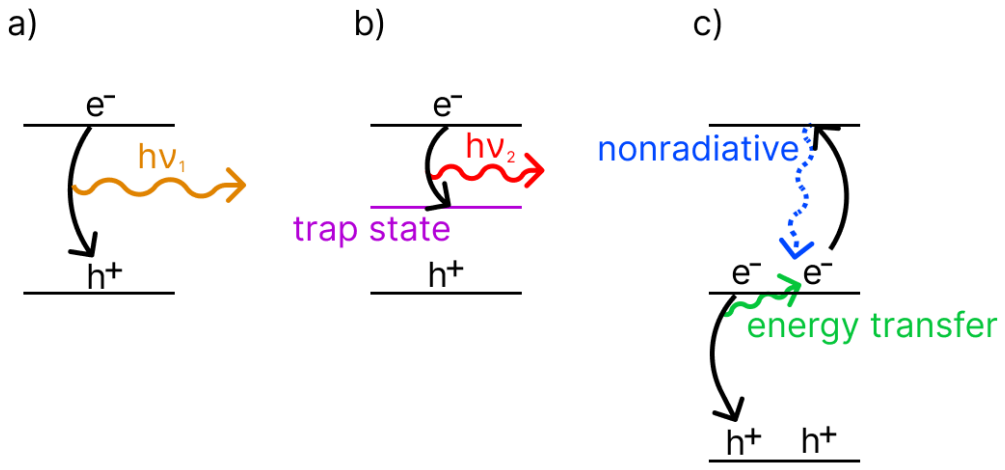

Figure 1.3: *Recombination modes in a solar cell; a) radiative recombination, where the bandgap energy is rereleased ($h\nu_1$), b) trap-assisted recombination, whereby an intermediate trap state allows an electron to emit radiation of lower energy than was absorbed ($h\nu_2$) later leading to recombination with another charge carrier, and c) Auger recombination, whereby recombination by other modes instead results in an energy transfer to a different electron, which non-radiatively dissipates its energy by thermalising back down to the original excited state.*

1.2.3. Solar Cell Generations

Solar cell developments were classified into three generations by Martin Green in 2001. First generation solar cells comprise the current market leader, crystalline Si solar cells. Second generation cells make use of thin film materials with a direct bandgap, with the aim of reducing the amount of material used. Third generation cells aim to surpass the Shockley-Queisser limit for 'single-junction' cell efficiency by adding additional absorber layers to create a 'multi-junction' solar cell[10].

In a solar cell, the charge must escape the absorber material and make its way to either electrode in order to generate electricity. To make this happen, an electric field must be present across the device. In silicon cells, this field is generated by selectively doping one side with group III elements such as boron (to have extra 'holes', or absences of electrons; 'p-type'), or group V elements such as phosphorus (to have extra electrons; 'n-type'). In second generation solar cells utilising thin film technologies, this approach is not as practical for every solar absorber material which is utilised, due to the materials often not being able to be easily and/or effectively doped as with silicon. To circumvent this, the electric field can instead be generated by applying an external 'hole-transport' layer (HTL) and 'electron-transport' layer (ETL) to opposite faces of the absorber layer. These layers effectively play the same role as doping does in Si cells; they generate an electric field to drive electrons towards one electrode and holes towards the other.

In third generation solar cells, the limited absorption range of a single material is expanded through the use of another, complementary material. Each absorber material absorbs a specific spectral range of light. By adding another material to the device structure with a 'complementary' absorption spectrum, the range of wavelengths which are not covered, or are covered poorly by the first material can be absorbed by the second. The fact that, due to the varied energies of the incoming photons, a single material cannot absorb all incoming light is another reason that solar cell efficiency is limited to ~33%. Therefore, by adding another material to expand the absorption range, the 33% limit can actually be surpassed. The current record efficiencies for common solar cell technologies are shown in *Figure 1.4*. Hybrid tandem (2-junction) solar cells with silicon and thin film inorganic absorbers have achieved a maximum of 36.1%. Silicon on its own only achieves 26.1%, so finding stable and cheap materials with a complementary absorption profile to silicon could be used to increase the efficiency of existing

silicon cell technologies. This would yield benefits such as decreased land use for solar farms and decreased demand on expensive resources used in the fabrication of full-scale modules, such as the silver used in electrodes.

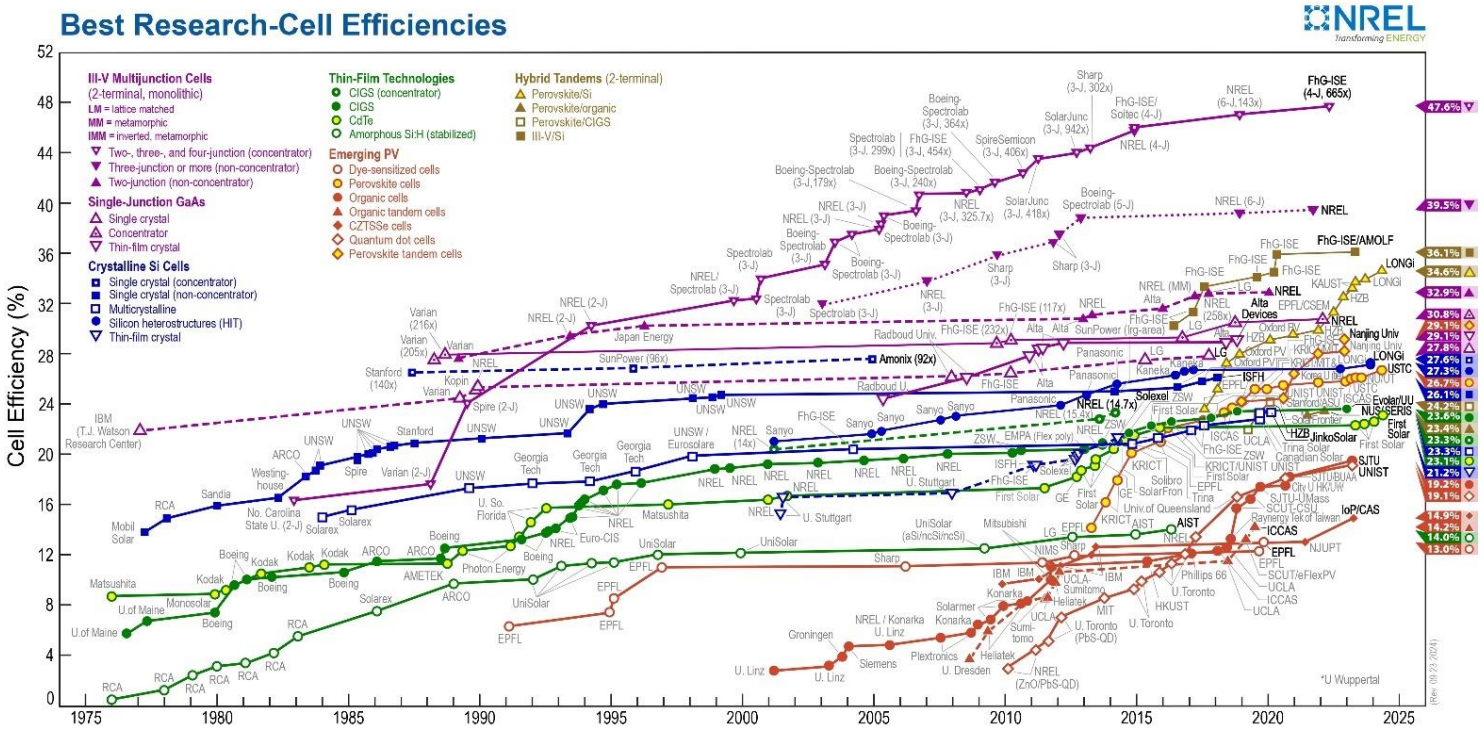

Figure 1.4: *National Renewable Energy Laboratory – 'Best Research-Cell Efficiencies' 2024*[11].

1.3. Antimony Chalcogenide Solar Cells

Antimony chalcogenides (Sb_2E_3, E = S, Se) are a very promising solar absorber material with many attractive properties. They have a high absorption coefficient of over 10^5 cm^{-1} in the visible wavelengths[12-22], meaning they are efficient at harvesting incoming light. They have a tuneable band-gap between 1.1 and 1.8 eV due to the ability to interchange S and Se freely without altering the crystal structure, allowing for the optimisation of the bandgap to raise the potential maximum efficiency to the Shockley-Queisser limit of ~33%[12, 13, 15-19]. Sb_2E_3 also has a direct bandgap, enabling it to have a final optimised thickness of around only 300 nm, compared to the optimum of ~170 µm for silicon[12, 23-27]. They also fulfil many practical and environmental concerns, being very stable in moisture and air, non-toxic and composed of earth-abundant materials[12, 13, 15, 16, 19-22].

Sb_2E_3 has an unusual 1-D crystal structure, with 'ribbons' of Sb_2E_3 which run parallel to one another, shown in *Figure 1.5*. Crystal orientation is of great importance in Sb_2E_3 solar cells, as charge transport along the length of the ribbons is much more effective than it is across them[22, 24, 28, 29]. Ideally, the ribbons would directly connect the electron transport layer (ETL) and hole transport layer (HTL), by standing perpendicular to each of their surfaces. This is commonly referred to as the (hk1) orientation.

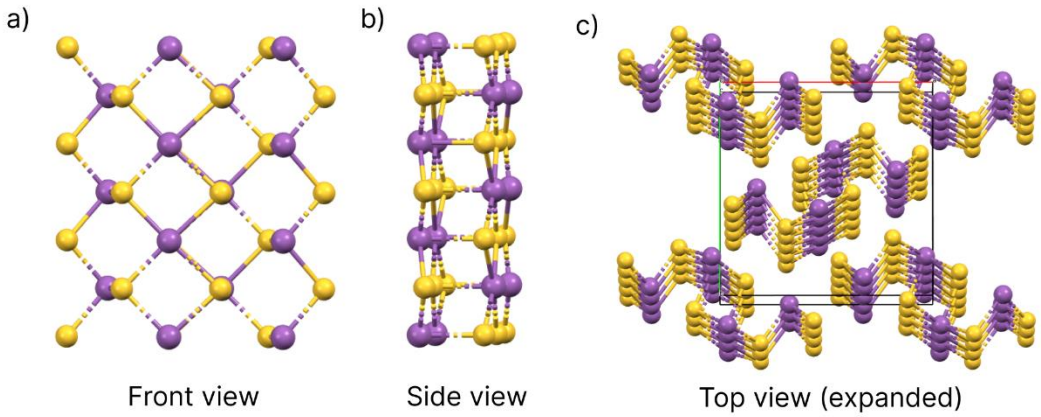

Figure 1.5: *Crystalline structure of antimony chalcogenides with Sb shown in purple and S/Se in yellow. Three view orientations are displayed: a) a single ribbon from the front, and b) a single ribbon from the side and c) a view of the larger crystal structure from the top, with the unit cell superimposed (5 ribbons running parallel, into/out of the plane of the page).*

The main limitation currently facing the commercialisation of antimony chalcogenide solar cells is that of low efficiency compared to other technologies, with record efficiencies lying between 10.5-10.75%[29-31]. These record efficiencies were all achieved through the application of chemical additives. Therefore, fully understanding these additives and the roles they play are of great importance to finding new, more effective additives to further increase the efficiency of Sb_2E_3 solar cells.

1.3.1. Fabrication Techniques

Many techniques have been developed for the fabrication of Sb_2E_3 solar cells, including vapour transport deposition[15, 22], pulsed laser deposition[32], spray pyrolysis[18, 20, 33, 34], spin coating[16, 35], chemical bath deposition[36-40] and hydrothermal (HT) synthesis[12, 13, 23-26, 29-31, 41-43]. Of these techniques, the most popular one, and the one which has attained the highest efficiency

solar cells, is hydrothermal (HT) deposition[29-31]. HT deposition involves the creation of a mixture of Sb and S/Se precursors in water, followed by heating of this mixture in a pressure-sealed autoclave to deposit a film of Sb_2E_3 onto a substrate. Further details of the HT process can be found in *Section 3.1.2*.

While the HT process has been successful in fabricating relatively high efficiency Sb_2E_3 solar cells, it requires the use of opaque steel autoclaves, meaning it is a 'black box' technique. Therefore, the growth of films cannot be observed, and the potential for observing and thus understanding the growth process is limited. It does, however, allow for easy use of additives, so long as they are water-soluble. To utilise an additive in HT synthesis, it is a simple matter of adding it to the HT solution before sealing and heating.

1.3.2. Device Structure

While Sb_2E_3 can utilise either internal doping or external ETL/HTLs to generate an internal electric field, the most effective results have been attained using ETL/HTLs[29-31, 44, 45]. The main ETL used for Sb_2E_3 solar cells is CdS, due to a good match between the CdS and Sb_2E_3 crystal surfaces, allowing effective charge transport across the interface between them[19, 24, 28, 46]. However, CdS is highly toxic, and suffers from 'parasitic absorption' towards Sb_2E_3 (whereby CdS absorbs some of the light which would have otherwise reached and generated charges in Sb_2E_3), so investigation into alternative ETLs with a wider bandgap and fewer safety concerns, such as metal oxides (ZnO, TiO_2, etc), is ongoing[20, 23, 33, 47-49].

For HTL materials, 2,2',7,7'-Tetrakis[N,N-di(4-methoxyphenyl)amino]-9,9'-spirobifluorene (Spiro-OMeTAD) is the HTL most commonly used in lab-based settings to achieve high efficiency. Attempts have been made to replace Spiro-OMeTAD due to concerns regarding thermal stability. Stable alternatives such as CuSCN have been investigated, though so far lower efficiencies have been reached than were obtained with Spiro-OMeTAD[50-53].

Electrode materials can also vary, with silver and gold being very commonly used. Silver is less expensive, but gold has higher conductivity. Higher conductivity helps to reduce the series resistance of the cell, improving the final efficiency.

1.3.3. Additives

Many additives have been used in Sb_2E_3 solar cells. A detailed listing of them is given in *Chapter 2*. The application of additives can be done as a pre-, bulk or post- treatment of the Sb_2E_3 film. Pre-treatments involve the treating of the layer onto which the Sb_2E_3 will be deposited, usually to improve the deposition and/or interfacial contact of the Sb_2E_3. Bulk treatments occur during the deposition of Sb_2E_3, and usually involve the additive working throughout the deposition process, and/or incorporating directly into the final film. Post-treatments occur after the Sb_2E_3 film has been deposited, and usually aim to passivate defects on the surface of the Sb_2E_3 and/or improve the interfacial contact with the next deposited layer.

1.4. Thesis Outline

This thesis aims to nudge the field of additive engineering in Sb_2E_3 solar cells towards a deeper understanding of the mechanisms by which the additives work. To that end, this thesis seeks to improve the efficiency of Sb_2E_3 cells using additives, whilst being able to explain and directly prove why each additive was effective. *Chapter 2* is a perspective article outlining the current state of additive engineering in Sb_2E_3, highlighting excellent examples that demonstrate how a deeper understanding of the underlying mechanisms in additive utilization enables new, bespoke additive design, resulting in significant efficiency gains. It also highlights some examples of studies where this understanding is lacking. One such study uses ethylenediaminetetraacetic acid (EDTA) as an additive. This additive is investigated in depth in this thesis, with the aim of understanding and expanding upon the existing proposed working mechanisms. In *Chapter 4*, EDTA is examined in the context of the working mechanisms proposed in the literature, using nuclear magnetic resonance spectroscopy (NMR) and a solution-based aggregation test. With further clarity regarding the observed behaviours of EDTA, *Chapter 5* then goes on to explore alternative additives that possess structures similar to EDTA, by utilising the solution-based aggregation test as a screening process. Finally, *Chapter 6* combines and solidifies the understanding afforded by these additives into detailed and evidence-based chemical explanations for the working mechanisms and phenomena

observed when applying EDTA and the additional successful additives discovered in *Chapter 5*.

1.5. References

1. Arrhenius, S., Xxxi. On the Influence of Carbonic Acid in the Air Upon the Temperature of the Ground. *The London, Edinburgh, and Dublin Philosophical Magazine and Journal of Science* **1896,** *41* (251), 237-276.

2. Plass, G. N., The Carbon Dioxide Theory of Climatic Change. *Tellus* **1956,** *8* (2), 140-154.

3. NASA, Vital Signs. NASA: https://climate.nasa.gov/vital-signs/, 2024.

4. NASA, Climate Change. NASA: https://science.nasa.gov/climate-change/, 2024.

5. Nations, U., Causes and Effects of Climate Change. United Nations: https://www.un.org/en/climatechange/science/causes-effects-climate-change, 2024.

6. *Statistical Review of World Energy*; Energy Institute: https://www.energyinst.org/statistical-review, 2024.

7. Hannah Ritchie, P. R. a. M. R. Energy Production and Consumption 2020. https://ourworldindata.org/energy-production-consumption.

8. IEA *Electricity 2024*; IEA: https://www.iea.org/reports/electricity-2024, 2024.

9. Shockley, W.; Queisser, H. J., Detailed Balance Limit of Efficiency of P-N Junction Solar Cells. *Journal of Applied Physics* **1961,** *32* (3), 510-519.

10. Green, M. A., Third Generation Photovoltaics: Ultra-High Conversion Efficiency at Low Cost. *Progress in Photovoltaics: Research and Applications* **2001,** *9* (2), 123-135.

11. Best Research-Cell Efficiency Chart. National Renewable Energy Laboratory: https://www.nrel.gov/pv/cell-efficiency.html, 2024.

12. Jiang, C.; Zhou, J.; Tang, R.; Lian, W.; Wang, X.; Lei, X.; Zeng, H.; Zhu, C.; Tang, W.; Chen, T., 9.7%-Efficient $Sb_2(S,Se)_3$ Solar Cells with a Dithieno[3,2-B: 2',3'-D]Pyrrole-Cored Hole Transporting Material. *Energy & Environmental Science* **2021,** *14* (1), 359-364.

13. Tang, R.; Wang, X.; Lian, W.; Huang, J.; Wei, Q.; Huang, M.; Yin, Y.; Jiang, C.; Yang, S.; Xing, G.; Chen, S.; Zhu, C.; Hao, X.; Green, M. A.; Chen, T., Hydrothermal Deposition of Antimony Selenosulfide Thin Films Enables Solar Cells with 10% Efficiency. *Nature Energy* **2020,** *5* (8), 587-595.

14. Wu, C.; Zhang, L.; Ding, H.; Ju, H.; Jin, X.; Wang, X.; Zhu, C.; Chen, T., Direct Solution Deposition of Device Quality $Sb_2S_{3-x}Se_x$ Films for High Efficiency Solar Cells. *Solar Energy Materials and Solar Cells* **2018,** *183*, 52-58.

15. Yin, Y.; Jiang, C.; Ma, Y.; Tang, R.; Wang, X.; Zhang, L.; Li, Z.; Zhu, C.; Chen, T., Sequential Coevaporation and Deposition of Antimony Selenosulfide Thin Film for Efficient Solar Cells. *Advanced Materials* **2021,** *33* (11), 2006689.

16. Wu, C.; Lian, W.; Zhang, L.; Ding, H.; Jiang, C.; Ma, Y.; Han, W.; Li, Y.; Zhu, J.; Chen, T.; Zhu, C., Water Additive Enhanced Solution Processing of Alloy $Sb_2(S_{1-x}Se_x)3$-Based Solar Cells. *Solar RRL* **2020,** *4* (5), 1900582.

17. Nie, R.; Seok, S. I., Efficient Antimony-Based Solar Cells by Enhanced Charge Transfer. *Small Methods* **2020,** *4* (2), 1900698.

18. Fan, S.; Shi, C.; Lv, K.; Wang, Q.; Guo, F.; Chen, W., The Low-Temperature Preparation for Low-Selenium $Sb_2S_xSe_y$ Thin Film Solar Cells with Efficiency of > 5%. *Journal of Nanoparticle Research* **2021,** *23* (2), 42.

19. Wu, C.; Jiang, C.; Wang, X.; Ding, H.; Ju, H.; Zhang, L.; Chen, T.; Zhu, C., Interfacial Engineering by Indium-Doped Cds for High Efficiency Solution Processed $Sb_2(S_{1-x}Se_x)3$ Solar Cells. *ACS Applied Materials & Interfaces* **2019,** *11* (3), 3207-3213.

20. Wang, L.; Li, D.-B.; Li, K.; Chen, C.; Deng, H.-X.; Gao, L.; Zhao, Y.; Jiang, F.; Li, L.; Huang, F.; He, Y.; Song, H.; Niu, G.; Tang, J., Stable 6%-Efficient $SbSe_3$ Solar Cells with a Zno Buffer Layer. *Nature Energy* **2017,** *2* (4), 17046.

21. Nicolás-Marín, M. M.; Ayala-Mato, F.; Vigil-Galán, O.; Courel, M., Simulation Analysis of $Cd_{1-x}Sn_xS/Sb_2(Se_{1-x}S_x)_3$ Solar Cells with N-I-P Structure. *Solar Energy* **2021,** *224*, 245-252.

22. Pan, Y.; Hu, X.; Guo, Y.; Pan, X.; Zhao, F.; Weng, G.; Tao, J.; Zhao, C.; Jiang, J.; Chen, S.; Yang, P.; Chu, J., Vapor Transport Deposition of Highly Efficient $Sb_2(S,Se)_3$ Solar Cells Via Controllable Orientation Growth. *Advanced Functional Materials* **2021,** *31* (28), 2101476.

23. Zhang, L.; Lian, W.; Zhao, X.; Yin, Y.; Chen, T.; Zhu, C., Sb2s3 Seed-Mediated Growth of Low-Defect Sb_2S_3 on a TiO_2 Substrate for Efficient Solar Cells. *ACS Applied Energy Materials* **2020,** *3* (12), 12417-12422.

24. Jin, X.; Fang, Y.; Salim, T.; Feng, M.; Hadke, S.; Leow, S. W.; Sum, T. C.; Wong, L. H., In Situ Growth of [Hk1]-Oriented Sb_2S_3 for Solution-Processed Planar Heterojunction Solar Cell with 6.4% Efficiency. *Advanced Functional Materials* **2020,** *30* (35), 2002887.

25. Huang, Y.; Tang, R.; Wang, G.; Li, G.; Che, B.; Wang, Y.; Lian, W.; Zhu, C.; Chen, T., Chemical Insight into the Hydrothermal Deposition of $Sb_2(S,Se)_3$ Towards Delicate Microstructure Engineering. *Journal of Materials Chemistry A* **2022,** *10* (18), 9892-9901.

26. Zhang, L.; Xiao, P.; Che, B.; Yang, J.; Cai, Z.; Wang, H.; Gao, J.; Liang, W.; Wu, C.; Chen, T., Mechanistic Study of the Transition from Antimony Oxide to Antimony Sulfide in the Hydrothermal Process to Obtain Highly Efficient Solar Cells. *ChemSusChem* **2023,** *16* (7), e202202049.

27. Kowalczewski, P.; Andreani, L. C., Towards the Efficiency Limits of Silicon Solar Cells: How Thin Is Too Thin? *Solar Energy Materials and Solar Cells* **2015,** *143*, 260-268.

28. Zhou, Y.; Wang, L.; Chen, S.; Qin, S.; Liu, X.; Chen, J.; Xue, D.-J.; Luo, M.; Cao, Y.; Cheng, Y.; Sargent, E. H.; Tang, J., Thin-Film Sb_2Se_3 Photovoltaics with Oriented One-Dimensional Ribbons and Benign Grain Boundaries. *Nature Photonics* **2015,** *9* (6), 409-415.

29. Wang, X.; Tang, R.; Jiang, C.; Lian, W.; Ju, H.; Jiang, G.; Li, Z.; Zhu, C.; Chen, T., Manipulating the Electrical Properties of $Sb_2(S,Se)_3$ Film for High-Efficiency Solar Cell. *Advanced Energy Materials* **2020,** *10* (40), 2002341.

30. Zhao, Y.; Wang, S.; Jiang, C.; Li, C.; Xiao, P.; Tang, R.; Gong, J.; Chen, G.; Chen, T.; Li, J.; Xiao, X., Regulating Energy Band Alignment Via Alkaline Metal Fluoride Assisted Solution Post-Treatment Enabling $Sb_2(S,Se)_3$ Solar Cells with 10.7% Efficiency. *Advanced Energy Materials* **2022,** *12* (1), 2103015.

31. Chen, X.; Che, B.; Zhao, Y.; Wang, S.; Li, H.; Gong, J.; Chen, G.; Chen, T.; Xiao, X.; Li, J., Solvent-Assisted Hydrothermal Deposition Approach for Highly-Efficient $Sb_2(S,Se)_3$ Thin-Film Solar Cells. *Advanced Energy Materials* **2023,** *13* (21), 2300391.

32. Chen, C.; Yin, Y.; Lian, W.; Jiang, L.; Tang, R.; Jiang, C.; Wu, C.; Gao, D.; Wang, X.; Fang, F.; Zhu, C.; Chen, T., Pulsed Laser Deposition of Antimony Selenosulfide Thin Film for Efficient Solar Cells. *Applied Physics Letters* **2020,** *116* (13), 133901.

33. Parize, R.; Katerski, A.; Gromyko, I.; Rapenne, L.; Roussel, H.; Kärber, E.; Appert, E.; Krunks, M.; Consonni, V., $ZnO/TiO_2/Sb_2S_3$ Core–Shell Nanowire Heterostructure for Extremely Thin Absorber Solar Cells. *The Journal of Physical Chemistry C* **2017,** *121* (18), 9672-9680.

34. Choi, Y. C.; Lee, D. U.; Noh, J. H.; Kim, E. K.; Seok, S. I., Highly Improved Sb_2S_3 Sensitized-Inorganic–Organic Heterojunction Solar Cells and Quantification of Traps by Deep-Level Transient Spectroscopy. *Advanced Functional Materials* **2014,** *24* (23), 3587-3592.

35. Zheng, Q.; Wang, C.; Ma, G.; Jin, M.; Cheng, S.; Lai, Y.; Yu, J., Annealing Temperature Impact on Sb_2S_3 Solar Cells Prepared by Spin-Coating Method. *Materials Letters* **2019,** *243*, 104-107.

36. Zhang, Y.; Li, S. a.; Tang, R.; Wang, X.; Chen, C.; Lian, W.; Zhu, C.; Chen, T., Phosphotungstic Acid Regulated Chemical Bath Deposition of Sb_2S_3 for High-Efficiency Planar Heterojunction Solar Cell. *Energy Technology* **2018,** *6* (11), 2126-2131.

37. Wang, Z.; Chen, G.; Wen, X.; Lin, L.; Feng, Z.; Liu, K.; Huang, P.; Zheng, Z., Low-Cost $TiO_2/Sb_2(S, Se)_3$ Heterojunction Thin Film Solar Cell Fabricated by Sol-Gel and Chemical Bath Deposition. *Materials Science in Semiconductor Processing* **2017,** *68*, 76-79.

38. Wang, S.; Zhao, Y.; Che, B.; Li, C.; Chen, X.; Tang, R.; Gong, J.; Wang, X.; Chen, G.; Chen, T.; Li, J.; Xiao, X., A Novel Multi-Sulfur Source Collaborative Chemical Bath Deposition Technology Enables 8%-Efficiency Sb_2S_3 Planar Solar Cells. *Advanced Materials* **2022,** *34* (41), 2206242.

39. Chate, P. A.; Sathe, D. J.; Lakde, S. D.; Bhabad, V. D., A Novel Method for the Deposition of Polycrystalline Sb_2S_3 Thin Films. *Journal of Materials Science: Materials in Electronics* **2016,** *27* (12), 12599-12603.

40. Yang, B.; Shi, C.; Huang, Y.; Wang, Y.; Hu, G.; Chen, W.; Guo, F., Chemical Bath Deposition of Sb_2S_3 Thin Films Using the Mixing Solution of $SbCl_3$ and Sodium Citrate as a Novel Sb Source for Assembling Efficient Solar Cells. *Journal of Materials Chemistry C* **2024,** *12* (3), 957-966.

41. Huang, Y.; Tang, R.; Xiao, P.; Che, B.; Wang, Y.; Gao, H.; Wang, G.; Zhu, C.; Chen, T., Efficient in Situ Sulfuration Process in Hydrothermally Deposited Sb_2S_3 Absorber Layers. *ACS Applied Materials & Interfaces* **2022,** *14* (49), 54822-54829.

42. Li, G.; Dong, J.; Xiao, P.; Che, B.; Huang, Y.; Zhang, Y.; Tang, R.; Zhu, C.; Chen, T., Dual Effect of NH_4F Additive in the Hydrothermal Deposition of Antimony Selenosulfide Thin Film for High-Performance Solar Cells. *Science China Materials* **2022,** *65* (12), 3411-3417.

43. Mkawi, E. M., Solvothermal Orthorhombic Sb_2S_3 Nanobars: Effect of Hydrothermal Temperature in Properties for Solar Cell Application. *Results in Physics* **2020,** *19*, 103603.

44. Diliegros Godines, C.; Santos, J.; Mathews, N.; Pal, M., Effect of Ag Doping on Structural, Optical and Electrical Properties of Antimony Sulfide Thin Films. *Journal of Materials Science* **2018,** *53*.

45. Tang, R.; Wang, X.; Jiang, C.; Li, S.; Liu, W.; Ju, H.; Yang, S.; Zhu, C.; Chen, T., N-Type Doping of Sb_2S_3 Light-Harvesting Films Enabling High-Efficiency Planar Heterojunction Solar Cells. *ACS Applied Materials & Interfaces* **2018,** *10* (36), 30314-30321.

46. Zeng, Y.; Huang, J.; Li, J.; Sun, K.; Shah, U. A.; Deng, H.; Zhang, X.; Sha, C.; Qian, C.; Song, H.; Hao, X., Comparative Study of TiO_2 and CdS as the Electron Transport Layer for Sb_2S_3 Solar Cells. *Solar RRL* **2022,** *6* (10), 2200435.

47. Choi, Y. C.; Lee, Y. H.; Im, S. H.; Noh, J. H.; Mandal, T. N.; Yang, W. S.; Seok, S. I., Efficient Inorganic-Organic Heterojunction Solar Cells Employing $Sb_2(S_xSe_{1-x})_3$ Graded-Composition Sensitizers. *Advanced Energy Materials* **2014,** *4* (7), 1301680.

48. Han, J.; Liu, Z.; Zheng, X.; Guo, K.; Zhang, X.; Hong, T.; Wang, B.; Liu, J., Trilaminar ZnO/ZnS/ Sb_2S_3 Nanotube Arrays for Efficient Inorganic–Organic Hybrid Solar Cells. *RSC Advances* **2014,** *4* (45), 23807-23814.

49. Guo, L.; Zhang, B.; Li, S.; Montgomery, A.; Li, L.; Xing, G.; Zhang, Q.; Qian, X.; Yan, F., Interfacial Engineering of Oxygenated Chemical Bath–Deposited Cds Window Layer for Highly Efficient Sb_2Se_3 Thin-Film Solar Cells. *Materials Today Physics* **2019,** *10*, 100125.

50. Itzhaik, Y.; Bendikov, T.; Hines, D.; Kamat, P. V.; Cohen, H.; Hodes, G., Band Diagram and Effects of the Kscn Treatment in TiO_2/ Sb_2S_3/CuSCN Eta Cells. *The Journal of Physical Chemistry C* **2016,** *120* (1), 31-41.

51. Li, K.; Wang, S.; Chen, C.; Kondrotas, R.; Hu, M.; Lu, S.; Wang, C.; Chen, W.; Tang, J., 7.5% N–I–P Sb_2Se_3 Solar Cells with Cuscn as a Hole-Transport Layer. *Journal of Materials Chemistry A* **2019,** *7* (16), 9665-9672.

52. Itzhaik, Y.; Niitsoo, O.; Page, M.; Hodes, G., Sb_2S_3-Sensitized Nanoporous TiO_2 Solar Cells. *The Journal of Physical Chemistry C* **2009,** *113* (11), 4254-4256.

53. Song, W.; Rakocevic, L.; Thiruvallur Eachambadi, R.; Qiu, W.; Bastos, J. P.; Gehlhaar, R.; Kuang, Y.; Hadipour, A.; Aernouts, T.; Poortmans, J., Improving the Morphology Stability of Spiro-Ometad Films for Enhanced Thermal Stability of Perovskite Solar Cells. *ACS Applied Materials & Interfaces* **2021,** *13* (37), 44294-44301.

2. Perspective: "Additive Engineering Mechanisms in Antimony Chalcogenide Solar Cells: A Focus on Deeper Understanding"

The contents of this chapter are planned to be published as a perspective article following the submission of this thesis.

2.1. Introduction

As established in *Chapter 1*, solar power is a powerful technology for reducing greenhouse gas emissions[1, 2]. Crystalline silicon (c-Si) is the most mature and widely adopted solar cell material in the world to date, holding 95% of the market share in 2021[3]. This is due to a high power conversion efficiency, good stability of ~30 years, and a low cost which has rapidly decreased over the past 30 years (the global weighted average levelised costs of electricity for large PV systems has decreased from €0.315/kWh in 2010 to €0.047/kWh in 2022)[4]. However, due to an indirect bandgap, the film thickness has remained above 150 µm, with little to no decrease since 2006[4]. This increases the amount of material required and used for manufacture, and places c-Si in a poor position for lightweight applications such as electric vehicles. The silicon required, despite being earth-abundant, is also very energy intensive to refine into the pure silicon needed for solar cells, which reduces its effectiveness as a low-carbon energy source[5]. Thin film alternatives such as Cu(In,Ga)Se_2 (CIGS), CdTe and GaAs have a direct bandgap so can be made with thicknesses of ~3µm and are already being industrialised. However, they are made from relatively scarce elements such as tellurium and indium, making them less suitable for mass production, and while CdTe itself is not toxic, the presence of cadmium may pose issues for the disposal of cells after their lifetime[5]. Another thin film technology, perovskites, has recently seen massive growth in the field, going from 14% to 26% efficiency in lab-scale in the last decade[6]. However, they suffer from inherent instability and contain toxic lead[7], so again are less suitable for domestic applications. Various other thin film technologies such as organic solar cells are also available, though these also suffer from issues such as low stability, which limit their applications[7].

Antimony chalcogenides (Sb_2E_3, E = S, Se) have good potential to address many, if not all, of the issues mentioned above. They boast inherently high stability[8-12], are formed of earth abundant materials[8, 10, 12-17] through a variety of relatively low-energy deposition processes[8, 10, 11, 13-15, 17-24], and have a strong absorption coefficient of >10^5 cm^{-1} at visible wavelengths[8-17, 25-27]. The bandgap can also be tuned between 1.1 eV (Sb_2Se_3) and 1.8 eV (Sb_2S_3) through S/Se substitution, while retaining their orthorhombic crystal structure[8-14, 25-27]. However, while it is theoretically possible to reach the Shockley-Queisser limit of ~32% using this bandgap tuning[13], the highest efficiency reached to date is only 10.75%[23]. This is primarily due to deficient V_{OC} values that currently are only around half of their theoretical maxima, which are in turn due to the presence of defects in the crystal structure and band misalignment with the transporting layers[25]. Interface engineering and defect passivation are the primary ways to accomplish this, and a review on this topic was performed by Zhang *et al.* in 2021[25]. Practically, the most successful approach to perform these tasks has been through the use of chemical additives such as ethylenediaminetetracetic acid (EDTA), NaF and EtOH, which were used to achieve 10.5%, 10.7% and 10.75%, respectively[23, 26, 28].

However, despite these successes, deeper understanding of the processes involved in forming high quality antimony chalcogenides and importantly, the role that additives play in this formation, is needed if this solar technology is to reach the efficiencies needed to be commercially viable.

2.2. Current Understanding of Additive Engineering Mechanisms

The primary challenge currently facing Sb_2E_3 solar cells is that of a low open circuit voltage (V_{OC}). A review on this topic was published in 2020 by Chao Chen and Jiang Tang[29], and another by Yi Zhang *et al.* in 2021[25]. Chen and Tang highlight that the short circuit current (J_{SC}) and fill factor (FF) in Sb_2E_3 solar cells have reached over 70% of the Shockley-Queisser limit (theoretical thermodynamic limit for single-junction solar cells). Therefore, to bring the overall performance of these cells to 15% and greater, the V_{OC} deficit must be reduced. Both reviews explain how there are two primary causes for this; interfacial recombination and defect-assisted recombination from deep-level trap states. Among many others, their suggestions to remedy these issues include:

- Defect passivation
- Surface treatment of ETL to improve lattice match, or of Sb_2E_3 to decrease Sb_2O_3 formation
- P-type doping

Additionally, the growth of a highly crystalline, hk1-orientated absorber layer is of paramount importance for effective charge transportation and a high-performance solar cell[13, 14, 18, 19, 26, 30-36]. Each of these effects can potentially be achieved through the use of chemical additives, and thus the understanding of chemical additives in Sb_2E_3 solar cells is a topic of great importance.

Additives have been used to great effect in other solar cell technologies, such as in perovskite solar cells, where conjugated bridging molecules are used to bridge grain boundaries, or in CdTe solar cells, where $CdCl_2$ is provides Cl to passivate grain boundaries, and Cd to fill Cd vacancies. In that case, it is often advantageous to establish design rules for additives. These rules can often be put into use relatively easily due to the flexible modification of chemical structures afforded by organic molecules, though it is possible to establish similar rules for inorganic additives[37-40]. If the desired functionality of an additive can be accurately determined, bespoke molecules can be synthesised which are optimised for the task at hand. Another good example of design rules being used to great effect is in organic solar cells, where even the absorbers themselves can be optimised and interchanged to maximise efficiency[41].

Another key consideration with additive engineering is the method by which the additive will be applied. Unlike alternative technologies such as perovskite and organic solar cells, many of the synthesis methods for Sb_2E_3 require a high temperature post-annealing step[8, 13, 21, 26, 28, 42-44], which limits the use of most organic molecules for long-lasting bulk-treatment purposes such as those seen for conjugated organic grain-boundary bridges in perovskite cells[37-39], as organic compounds may decompose at the high temperatures required[45]. Similarly, if an additive is used to aid deposition, considerations must be made for it and/or its decomposition products to potentially be present in the final film, which may introduce unwanted trap states and recombination centres. The various synthesis methods also lend themselves differently to the use of additives, particularly for bulk treatments of the absorber film. Of these methods, hydrothermal (HT) and chemical bath deposition (CBD) have seen the most success[8, 13, 21, 26,

[42, 44]. As long as the additive is water-soluble, it can simply be added to the reaction mixture prior to deposition. So, while other synthesis methods such as vapour transport deposition and spray pyrolysis confer other benefits such as growth on nanostructured substrates and high crystallinity[17, 20], they cannot as easily make use of the wide range of additives available for HT and CBD.

2.3. Additives in Sb_2E_3 Solar Cell Literature and their Mechanisms

Achieving high performance is key to the success of antimony chalcogenides. They have high stability, varied and relatively low energy deposition processes and are made from abundant materials, but fall behind the competitors when it comes to performance. It makes sense then to focus on that aspect when performing research. However, we implore that this be accompanied by a drive to deeply understand the mechanisms which provide this performance, as this will serve to aid future research efforts and ultimately, yield more meaningful progress. This approach may also help to avoid pitfalls whereby the stability and/or benign nature of the material is compromised for the sake of performance.

There are many different avenues through which additives can improve Sb_2E_3 solar cell performance, including defect passivation, improving lattice match, decreasing Sb_2O_3 formation, p-type doping of Sb_2E_3, and improved film crystallinity and orientation. Below, we detail various examples which make use of these effects. We highlight some excellent examples of where in-depth mechanistic investigation have yielded widely applicable and fundamental understanding, while also noting some examples where more in-depth mechanistic investigation would be beneficial to future works. The examples we highlight, and other notable studies, are summarised in Table 1. Most of the 'overall effects' on the cell listed in Table 1 are relatively straightforward to measure using established techniques such as X-ray diffraction (XRD) and scanning electron microscopy (SEM). However, in many cases the details on *how* the additive achieves its effects are not fully explored. The majority of the listed additives work by reducing crystal defects and oxide phases, so by deeply understanding the mechanisms by which these effects happen, it is reasonable to assume that greater efficiency gains than those already seen could be attained.

Table 2.1: *Examples of chemical additives and their overall effects in Sb_2E_3 solar cells*

	Application Method	**Sb_2E_3 System**	**Synthesis Method**	**Efficiency Achieved (%)**	**Standard Efficiency (%)**	**Overall Effect on Cells**	**Ref.**
Ethanol	Bulk	S/Se	HT	10.75	9.12	Limits availability of Sb	[23]
Ethyelenediaminetetraacetic acid (EDTA)	Bulk	S/Se	HT	10.5	9.4	Improved crystallinity	[26]
NH_4F	Bulk	S/Se	HT	10.28	9.16	Dissolution and redeposition of CdS	[44]
Zeolite	Bulk	S/Se	HT	8.87	7.28	Reduced defects and oxide phases	[43]
Thioacetamide (+thiourea)	Bulk	S	CBD	8.0	6.49	Reduced defects and oxide phases	[42]
$N(NH_4)_2S$	Bulk	S	HT	6.92	6.01	Reduced defects and oxide phases	[46]
$[TMA][PF_6]$	Bulk	S	Spin coated	6.83	4.43	Limits availability of Sb	[47]
Tartaric acid	Bulk	S	HT	6.31	5.46	Reduced defects and oxide phases	[48]
4-Chloro-3-nitrobenzenesulfonyl Chloride	Bulk	S	Spin coated	5.84	4.2	Limits availability of Sb	[34]
PCDTBT	Bulk	S	HT	5.11	2.61	Improved crystallinity	[49]
Phosphotungstic Acid	Bulk	S	CBD	4.61	1.91	Suppression of oxides and oxyhalides	[50]
NaF (KF, RbF, CsF)	Post-treatment	S/Se	HT	10.7	9.2	Improved band alignment	[28]
$SbCl_3$	Post-treatment	S	Spin coated	7.1	4.37	Reduced defects and oxide phases	[51]

Thioacetamide	Post-treatment	S	CBD	7.1	5.5	Reduced surface defects and oxide phases	[21]
H_2S	Post-treatment	S/Se	Thermal Evaporation	5.98	3.08	Reduced defects and oxide phases	[24]
KSCN/LiSCN	Post-treatment	S	CBD	3.37; 3.7	N/A	Doping of CuSCN HTL	[52, 53]

To begin, we present an excellent study conducted by the current leaders in Sb_2E_3 cell efficiency, Chen *et al*., for their use of EtOH for a solvent-assisted hydrothermal deposition of $Sb_2(S, Se)_3$ which achieved 10.75%[23]. By observing the thickness and morphology of the films formed using various amounts of EtOH in the hydrothermal mixture, they saw that EtOH has an effect on reaction kinetics. Specifically, it slowed the deposition of $Sb_2(S, Se)_3$, leading to an increase in crystallinity and crystal grain size. They demonstrated that this was the case by showing a notable film thickness decrease with an increasing ratio of EtOH : water in the reaction mixture. They proposed a potential explanation for the phenomena observed; the precursor potassium antimony tartrate (PAT) was less soluble in EtOH, thereby reducing the Sb available for deposition at any one time. Reducing the Sb available slowed down deposition and improved the crystallinity of the film. This not only fit with their observed results, but they also directly observed this solubility effect when dissolving PAT in the relevant solutions. This study provides solvent engineering as a direct and widely applicable method of lowering PAT solubility, leading to favourable film growth.

When EDTA was used by Wang *et al*. in 2020, they achieved a very high efficiency of 10.5%. However, their conclusion of the mechanism was based on a rational assumption that aggregates of the precursor potassium antimony tartrate exist and are broken up by EDTA[26]. While they explain their proposed mechanism well, they only provide the observed surface morphology of the final film as experimental evidence of this effect. Similarly, when PCDTBT was used in the recently published work of Mkawi *et al*., they demonstrated an improvement in cell performance, but only through improved crystallinity and larger crystallite size[49]. While they thoroughly investigated these superficial effects with XRD, Raman, SEM and TEM, even using a variety of PCDTBT concentrations, no effort was made to even explain the role of

PCDTBT, let alone prove the proposed mechanism experimentally. We believe this exemplifies the issues present with the current focus on cell performance over mechanistic study. For researchers seeking to expand upon the above studies, there is minimal practical information available aside from the observation that additives positively impacted the cell's performance by forming a higher quality film.

An excellent illustration of a research endeavour that offers widespread and valuable insights into the underlying mechanisms is the work performed by Huang *et al.* in early 2022, with their chemical investigation into the hydrothermal process[43]. By scrutinizing the chemical properties of the hydrothermal deposition process of $Sb_2(S, Se)_3$, they were able to show that the altering the pH of the precursor solution can improve the film deposition. However, one of the precursors, $Na_2S_2O_3$, is sensitive to pH. Wanting to consider these constraints, while also avoiding adding extra impurities with conventionally applied bases, they introduced a H^+-selective zeolite to the solution and found that it improved the efficiency from 7.28% to 8.87%. This bottom-up approach allowed them to identify and avoid issues with other potential additives before trying them in full devices.

Another study which made good use of already existing widespread knowledge on the underlying mechanisms was conducted by Huang *et al.* in early 2023, exploring a hydrothermal sulfurization strategy[46]. Sulfurization is a well-established method for enhancing antimony sulfide films through the reduction of S vacancies and reduction of oxide phases[24, 42, 43, 46, 48]. In this study, they explain their sulfurization mechanism using $(NH_4)_2S$ by the formation of NH_3 and H_2S during the hydrothermal process through a well-known hydrolysis reaction. These processes are combined to give an effective hot in-situ sulfur source in the form of H_2S during deposition. In the end, they improve the efficiency from 6.01% to 6.92%.

Often studies base their work on insights from other solar technologies, in which case much of the mechanistic explanation may already exist. In this case, it is still key to explain the role of the additive in this new field/system. For example, when Zhao *et al.* attained 10.7% in $Sb_2(S, Se)_3$ cells through the use of NaF in 2021, they based their work on prior successful experiments on CIGS solar cells[54, 55]. However, they importantly still investigated the new system and found that the NaF etches sulfur from the film, thereby decreasing the S/Se gradient and leading to more favourable band alignment in the solar cell. In this case, they

have ample experimental evidence for this gradient and its decrease in the form of energy-dispersive X-ray spectroscopy (EDS), secondary ion mass spectroscopy (SIMS) and a shift in powder X-ray diffraction (P-XRD) peaks[28]. They also measure the sodium and fluorine concentration at various points in the films using SIMS and conclude that sodium doping is likely a factor in the improved performance. They also clearly state in their abstract that "this approach is able to manipulate the S/Se gradient in the films and creates favourable energy alignment which facilitates carrier transport". However, ideally the reasoning behind why sodium in particular has this effect could allow for the discovery and/or design of a reagent which performs this task even more effectively.

Another study which made use of additives established in other solar technologies was the study of phosphotungstic and related heteropoly acids by Chen *et al*. in 2018[50]. Heteropoly acids are known for their use in dye-sensitised solar cells for modification of the TiO_2 photoanode[56]. In their study, Chen *et al*. include mechanistic investigation of the various heteropoly acids, and conclude through comparison of their acidity and oxidative potentials that a high acidity and low oxidative potential are required for an effective additive. However, they only compare these properties within heteropoly acids and not with other acids besides HCl, and they note that while HCl may have a positive impact on performance, it can damage the final Sb_2S_3 film. Additionally, they do not propose or prove a detailed chemical mechanism for the method by which the acidity or oxidative potentials provide the suppression of Sb_2O_3, thereby limiting the broad applicability of the knowledge attained in the study for the design of new additives.

2.4. Conclusions and Outlook

The field of antimony chalcogenides has rapidly advanced in the past decade, and the future of the field looks highly promising, however for this advancement to continue apace, vigilance must be taken to ensure progress is accompanied by understanding of the reasons behind said progress. Improvement of cell performance without a clear, experimentally validated explanation is of little use to the wider research body, and can even mislead future studies if incorrect assumptions are made. To contribute more valuable insights to the broader research community and facilitate advancements in antimony chalcogenide solar cells, our suggestion

is to shift our attention towards understanding the underlying factors driving performance enhancements. By prioritising the exploration of the reasons behind the performance improvements, progress will naturally follow as our comprehension deepens. This deeper understanding will also naturally aid newer researchers in the field with concrete, validated evidence and explanations of underlying principles on which they can base their work, further aiding the drive towards high-efficiency cells. Gaining this understanding is often very challenging, but we hope that by highlighting some examples where excellent investigation has been performed, we can inspire more novel approaches to be developed. We believe a greater focus on mechanisms and processes involved in the formation of good quality antimony chalcogenide solar cells is paramount to continued progress and to encourage new researchers and academics to join this exciting field. With clear and in-depth understanding, the design and development of high-performance, benign, low-cost additives will be made both easier and faster.

2.5. References

1. Inventory of U.S. Greenhouse Gas Emissions and Sinks: 1990-2022 EPA, Ed. 2024.
2. Pehl, M.; Arvesen, A.; Humpenöder, F.; Popp, A.; Hertwich, E. G.; Luderer, G., Understanding Future Emissions from Low-Carbon Power Systems by Integration of Life-Cycle Assessment and Integrated Energy Modelling. *Nature Energy* **2017,** *2* (12), 939-945.
3. *Special Report on Solar PV Global Supply Chains*; IEA: 2022.
4. *Photovoltaics Report*; Fraunhofer Institute for Solar Energy Systems: www.ise.fraunhofer.de, 2024.
5. Dr. Rader Jensen, M. E. I. In *Efficient Utilization of Elements*, The Chemical Sciences and Society Summit, Narita Japan, Sept 16-19 2013; American Chemical Society: Narita Japan, 2013; p 6.
6. Best Research-Cell Efficiency Chart. National Renewable Energy Laboratory: https://www.nrel.gov/pv/cell-efficiency.html, 2024.
7. Martin Heinrich, T. E. K., Frank Dimroth, Uli Würfel, Jan Christoph Goldschmidt, Michael Powalla, Ste-; fan Glunz, D. H. N., A Comparison of Different Solar Cell Technologies

for Integrated Photovoltaics. In *37th European PV Solar Energy Conference and Exhibition*, Fraunhofer Institute for Solar Energy Systems ISE: Lisbon Congress Centre, 2020.

8. Jiang, C.; Zhou, J.; Tang, R.; Lian, W.; Wang, X.; Lei, X.; Zeng, H.; Zhu, C.; Tang, W.; Chen, T., 9.7%-Efficient $Sb_2(S,Se)_3$ Solar Cells with a Dithieno[3,2-B: 2',3'-D]Pyrrole-Cored Hole Transporting Material. *Energy & Environmental Science* **2021,** *14* (1), 359-364.

9. Wu, C.; Zhang, L.; Ding, H.; Ju, H.; Jin, X.; Wang, X.; Zhu, C.; Chen, T., Direct Solution Deposition of Device Quality $Sb_2S_{3-x}Se_x$ Films for High Efficiency Solar Cells. *Solar Energy Materials and Solar Cells* **2018,** *183*, 52-58.

10. Wu, C.; Lian, W.; Zhang, L.; Ding, H.; Jiang, C.; Ma, Y.; Han, W.; Li, Y.; Zhu, J.; Chen, T.; Zhu, C., Water Additive Enhanced Solution Processing of Alloy $Sb_2(S_{1-x}Se_x)_3$-Based Solar Cells. *Solar RRL* **2020,** *4* (5), 1900582.

11. Fan, S.; Shi, C.; Lv, K.; Wang, Q.; Guo, F.; Chen, W., The Low-Temperature Preparation for Low-Selenium $Sb_2S_xSe_y$ Thin Film Solar Cells with Efficiency of > 5%. *Journal of Nanoparticle Research* **2021,** *23* (2), 42.

12. Wu, C.; Jiang, C.; Wang, X.; Ding, H.; Ju, H.; Zhang, L.; Chen, T.; Zhu, C., Interfacial Engineering by Indium-Doped CdS for High Efficiency Solution Processed $Sb_2(S_{1-x}Se_x)_3$ Solar Cells. *ACS Applied Materials & Interfaces* **2019,** *11* (3), 3207-3213.

13. Tang, R.; Wang, X.; Lian, W.; Huang, J.; Wei, Q.; Huang, M.; Yin, Y.; Jiang, C.; Yang, S.; Xing, G.; Chen, S.; Zhu, C.; Hao, X.; Green, M. A.; Chen, T., Hydrothermal Deposition of Antimony Selenosulfide Thin Films Enables Solar Cells with 10% Efficiency. *Nature Energy* **2020,** *5* (8), 587-595.

14. Yin, Y.; Jiang, C.; Ma, Y.; Tang, R.; Wang, X.; Zhang, L.; Li, Z.; Zhu, C.; Chen, T., Sequential Coevaporation and Deposition of Antimony Selenosulfide Thin Film for Efficient Solar Cells. *Advanced Materials* **2021,** *33* (11), 2006689.

15. Wang, L.; Li, D.-B.; Li, K.; Chen, C.; Deng, H.-X.; Gao, L.; Zhao, Y.; Jiang, F.; Li, L.; Huang, F.; He, Y.; Song, H.; Niu, G.; Tang, J., Stable 6%-Efficient Sb_2Se_3 Solar Cells with a ZnO Buffer Layer. *Nature Energy* **2017,** *2* (4), 17046.

16. Nicolás-Marín, M. M.; Ayala-Mato, F.; Vigil-Galán, O.; Courel, M., Simulation Analysis of $Cd_{1-x}Zn_xS/Sb_2(Se_{1-x}S_x)_3$ Solar Cells with N-I-P Structure. *Solar Energy* **2021,** *224*, 245-252.

17. Pan, Y.; Hu, X.; Guo, Y.; Pan, X.; Zhao, F.; Weng, G.; Tao, J.; Zhao, C.; Jiang, J.; Chen, S.; Yang, P.; Chu, J., Vapor Transport Deposition of Highly Efficient $Sb_2(S,Se)_3$ Solar Cells Via Controllable Orientation Growth. *Advanced Functional Materials* **2021,** *31* (28), 2101476.

18. Zhang, L.; Lian, W.; Zhao, X.; Yin, Y.; Chen, T.; Zhu, C., Sb_2S_3 Seed-Mediated Growth of Low-Defect Sb_2S_3 on a TiO_2 Substrate for Efficient Solar Cells. *ACS Applied Energy Materials* **2020,** *3* (12), 12417-12422.

19. Chen, C.; Yin, Y.; Lian, W.; Jiang, L.; Tang, R.; Jiang, C.; Wu, C.; Gao, D.; Wang, X.; Fang, F.; Zhu, C.; Chen, T., Pulsed Laser Deposition of Antimony Selenosulfide Thin Film for Efficient Solar Cells. *Applied Physics Letters* **2020,** *116* (13), 133901.

20. Parize, R.; Katerski, A.; Gromyko, I.; Rapenne, L.; Roussel, H.; Kärber, E.; Appert, E.; Krunks, M.; Consonni, V., ZnO/TiO_2/ Sb_2S_3 Core–Shell Nanowire Heterostructure for Extremely Thin Absorber Solar Cells. *The Journal of Physical Chemistry C* **2017,** *121* (18), 9672-9680.

21. Choi, Y. C.; Lee, D. U.; Noh, J. H.; Kim, E. K.; Seok, S. I., Highly Improved Sb_2S_3 Sensitized-Inorganic–Organic Heterojunction Solar Cells and Quantification of Traps by Deep-Level Transient Spectroscopy. *Advanced Functional Materials* **2014,** *24* (23), 3587-3592.

22. Deng, H.; Zeng, Y.; Ishaq, M.; Yuan, S.; Zhang, H.; Yang, X.; Hou, M.; Farooq, U.; Huang, J.; Sun, K.; Webster, R.; Wu, H.; Chen, Z.; Yi, F.; Song, H.; Hao, X.; Tang, J., Quasiepitaxy Strategy for Efficient Full-Inorganic Sb_2S_3 Solar Cells. *Advanced Functional Materials* **2019,** *29* (31), 1901720.

23. Chen, X.; Che, B.; Zhao, Y.; Wang, S.; Li, H.; Gong, J.; Chen, G.; Chen, T.; Xiao, X.; Li, J., Solvent-Assisted Hydrothermal Deposition Approach for Highly-Efficient $Sb_2(S,Se)_3$ Thin-Film Solar Cells. *Advanced Energy Materials* **2023,** *13* (21), 2300391.

24. Yao, S.; Wang, J.; Cheng, J.; Fu, L.; Xie, F.; Zhang, Y.; Li, L., Improved Performance of Thermally Evaporated Sb_2Se_3 Thin-Film Solar Cells Via Substrate-Cooling-Speed Control and Hydrogen-Sulfide Treatment. *ACS Applied Materials & Interfaces* **2020,** *12* (21), 24112-24124.

25. Dong, J.; Liu, Y.; Wang, Z.; Zhang, Y., Boosting V_{oc} of Antimony Chalcogenide Solar Cells: A Review on Interfaces and Defects. *Nano Select* **2021,** *2* (10), 1818-1848.

26. Wang, X.; Tang, R.; Jiang, C.; Lian, W.; Ju, H.; Jiang, G.; Li, Z.; Zhu, C.; Chen, T., Manipulating the Electrical Properties of $Sb_2(S,Se)_3$ Film for High-Efficiency Solar Cell. *Advanced Energy Materials* **2020,** *10* (40), 2002341.

27. Nie, R.; Seok, S. I., Efficient Antimony-Based Solar Cells by Enhanced Charge Transfer. *Small Methods* **2020,** *4* (2), 1900698.

28. Zhao, Y.; Wang, S.; Jiang, C.; Li, C.; Xiao, P.; Tang, R.; Gong, J.; Chen, G.; Chen, T.; Li, J.; Xiao, X., Regulating Energy Band Alignment Via Alkaline Metal Fluoride Assisted Solution Post-Treatment Enabling $Sb_2(S,Se)_3$ Solar Cells with 10.7% Efficiency. *Advanced Energy Materials* **2022,** *12* (1), 2103015.

29. Chen, C.; Tang, J., Open-Circuit Voltage Loss of Antimony Chalcogenide Solar Cells: Status, Origin, and Possible Solutions. *ACS Energy Letters* **2020,** *5* (7), 2294-2304.

30. Cao, Y.; Liu, C.; Jiang, J.; Zhu, X.; Zhou, J.; Ni, J.; Zhang, J.; Pang, J.; Rummeli, M. H.; Zhou, W.; Liu, H.; Cuniberti, G., Theoretical Insight into High-Efficiency Triple-Junction Tandem Solar Cells Via the Band Engineering of Antimony Chalcogenides. *Solar RRL* **2021,** *5* (4), 2000800.

31. Li, J.; Huang, J.; Li, K.; Zeng, Y.; Zhang, Y.; Sun, K.; Yan, C.; Xue, C.; Chen, C.; Chen, T.; Green, M. A.; Tang, J.; Hao, X., Defect-Resolved Effective Majority Carrier Mobility in Highly Anisotropic Antimony Chalcogenide Thin-Film Solar Cells. *Solar RRL* **2021,** *5* (3), 2000693.

32. Jin, X.; Fang, Y.; Salim, T.; Feng, M.; Hadke, S.; Leow, S. W.; Sum, T. C.; Wong, L. H., In Situ Growth of [Hk1]-Oriented Sb_2S_3 for Solution-Processed Planar Heterojunction Solar Cell with 6.4% Efficiency. *Advanced Functional Materials* **2020,** *30* (35), 2002887.

33. Zhou, Y.; Wang, L.; Chen, S.; Qin, S.; Liu, X.; Chen, J.; Xue, D.-J.; Luo, M.; Cao, Y.; Cheng, Y.; Sargent, E. H.; Tang, J., Thin-Film Sb_2Se_3 Photovoltaics with Oriented One-Dimensional Ribbons and Benign Grain Boundaries. *Nature Photonics* **2015,** *9* (6), 409-415.

34. Zhou, H.; Han, J.; Pu, X.; Li, X., Effective Additive for Enhancing the Performance of Sb2s3 Planar Thin Film Solar Cells. *Journal of Materiomics* **2021,** *7* (5), 1074-1082.

35. Shah, U. A.; Chen, S.; Khalaf, G. M. G.; Jin, Z.; Song, H., Wide Bandgap Sb_2S_3 Solar Cells. *Advanced Functional Materials* **2021,** *31* (27), 2100265.

36. Liang, G.; Chen, M.; Ishaq, M.; Li, X.; Tang, R.; Zheng, Z.; Su, Z.; Fan, P.; Zhang, X.; Chen, S., Crystal Growth Promotion and Defects Healing Enable Minimum Open-Circuit Voltage Deficit in Antimony Selenide Solar Cells. *Adv Sci (Weinh)* **2022,** *9* (9), e2105142.

37. Buyruk, A.; Blätte, D.; Günther, M.; Scheel, M. A.; Hartmann, N. F.; Döblinger, M.; Weis, A.; Hartschuh, A.; Müller-Buschbaum, P.; Bein, T.; Ameri, T., 1,10-Phenanthroline as an Efficient Bifunctional Passivating Agent for $MaPbI_3$ Perovskite Solar Cells. *ACS Applied Materials & Interfaces* **2021,** *13* (28), 32894-32905.

38. Min, J.; Zhang, Z.-G.; Hou, Y.; Ramirez Quiroz, C. O.; Przybilla, T.; Bronnbauer, C.; Guo, F.; Forberich, K.; Azimi, H.; Ameri, T.; Spiecker, E.; Li, Y.; Brabec, C. J., Interface Engineering of Perovskite Hybrid Solar Cells with Solution-Processed Perylene–Diimide Heterojunctions toward High Performance. *Chemistry of Materials* **2015,** *27* (1), 227-234.

39. Kim, K.; Han, J.; Maruyama, S.; Balaban, M.; Jeon, I., Role and Contribution of Polymeric Additives in Perovskite Solar Cells: Crystal Growth Templates and Grain Boundary Passivators. *Solar RRL* **2021,** *5* (5), 2000783.

40. Feng, X.; Lv, X.; Cao, J.; Tang, Y., Continuous Modification of Perovskite Film by a Eu Complex to Fabricate the Thermal and Uv-Light-Stable Solar Cells. *ACS Applied Materials & Interfaces* **2022,** *14* (50), 55538-55547.

41. Dennler, G.; Scharber, M. C.; Ameri, T.; Denk, P.; Forberich, K.; Waldauf, C.; Brabec, C. J., Design Rules for Donors in Bulk-Heterojunction Tandem Solar Cells towards 15 % Energy-Conversion Efficiency. *Advanced Materials* **2008,** *20* (3), 579-583.

42. Wang, S.; Zhao, Y.; Che, B.; Li, C.; Chen, X.; Tang, R.; Gong, J.; Wang, X.; Chen, G.; Chen, T.; Li, J.; Xiao, X., A Novel Multi-Sulfur Source Collaborative Chemical Bath Deposition Technology Enables 8%-Efficiency Sb_2S_3 Planar Solar Cells. *Advanced Materials* **2022,** *34* (41), 2206242.

43. Huang, Y.; Tang, R.; Wang, G.; Li, G.; Che, B.; Wang, Y.; Lian, W.; Zhu, C.; Chen, T., Chemical Insight into the Hydrothermal Deposition of $Sb_2(S,Se)_3$ Towards Delicate Microstructure Engineering. *Journal of Materials Chemistry A* **2022,** *10* (18), 9892-9901.

44. Li, G.; Dong, J.; Xiao, P.; Che, B.; Huang, Y.; Zhang, Y.; Tang, R.; Zhu, C.; Chen, T., Dual Effect of NH_4F Additive in the Hydrothermal Deposition of Antimony Selenosulfide Thin Film for High-Performance Solar Cells. *Science China Materials* **2022,** *65* (12), 3411-3417.

45. Nobre, C.; Şen, A.; Durão, L.; Miranda, I.; Pereira, H.; Gonçalves, M., Low-Temperature Pyrolysis Products of Waste Cork and Lignocellulosic Biomass: Product Characterization. *Biomass Conversion and Biorefinery* **2023,** *13* (3), 2267-2277.

46. Huang, Y.; Gao, H.; Peng, X.; Wang, G.; Xiao, P.; Che, B.; Tang, R.; Zhu, C.; Chen, T., A Robust Hydrothermal Sulfuration Strategy toward Effective Defect Passivation Enabling 6.92% Efficiency Sb_2S_3 Solar Cells. *Solar RRL* **2023,** *7* (6), 2201115.

47. Han, J.; Pu, X.; Zhou, H.; Cao, Q.; Wang, S.; Yang, J.; Zhao, J.; Li, X., Multidentate Anchoring through Additive Engineering for Highly Efficient Sb_2S_3 Planar Thin Film Solar Cells. *Journal of Materials Science & Technology* **2021,** *89*.

48. Huang, Y.; Tang, R.; Xiao, P.; Che, B.; Wang, Y.; Gao, H.; Wang, G.; Zhu, C.; Chen, T., Efficient in Situ Sulfuration Process in Hydrothermally Deposited Sb_2S_3 Absorber Layers. *ACS Applied Materials & Interfaces* **2022,** *14* (49), 54822-54829.

49. Mkawi, E. M.; Al-Hadeethi, Y., Enhanced Antimony Sulfide Sb_2S_3 Nanobars Solar Cell Performance with Doped PCDTBT Polymer. *International Journal of Energy Research* **2023,** *2023*, 2636957.

50. Zhang, Y.; Li, S. a.; Tang, R.; Wang, X.; Chen, C.; Lian, W.; Zhu, C.; Chen, T., Phosphotungstic Acid Regulated Chemical Bath Deposition of Sb_2S_3 for High-Efficiency Planar Heterojunction Solar Cell. *Energy Technology* **2018,** *6* (11), 2126-2131.

51. Han, J.; Wang, S.; Yang, J.; Guo, S.; Cao, Q.; Tang, H.; Pu, X.; Gao, B.; Li, X., Solution-Processed Sb_2S_3 Planar Thin Film Solar Cells with a Conversion Efficiency of 6.9% at an Open Circuit Voltage of 0.7 V Achieved Via Surface Passivation by a $SbCl_3$ Interface Layer. *ACS Applied Materials & Interfaces* **2020,** *12* (4), 4970-4979.

52. Itzhaik, Y.; Niitsoo, O.; Page, M.; Hodes, G., Sb_2S_3-Sensitized Nanoporous TiO_2 Solar Cells. *The Journal of Physical Chemistry C* **2009,** *113* (11), 4254-4256.

53. Nezu, S.; Larramona, G.; Choné, C.; Jacob, A.; Delatouche, B.; Péré, D.; Moisan, C., Light Soaking and Gas Effect on Nanocrystalline TiO_2/ Sb_2S_3/CuSCN Photovoltaic Cells Following Extremely Thin Absorber Concept. *The Journal of Physical Chemistry C* **2010,** *114* (14), 6854-6859.

54. Reinhard, P.; Bissig, B.; Pianezzi, F.; Avancini, E.; Hagendorfer, H.; Keller, D.; Fuchs, P.; Döbeli, M.; Vigo, C.; Crivelli, P.; Nishiwaki, S.; Buecheler, S.; Tiwari, A. N., Features of KF and NaF Postdeposition Treatments of Cu(In,Ga)Se_2 Absorbers for High Efficiency Thin Film Solar Cells. *Chemistry of Materials* **2015,** *27* (16), 5755-5764.

55. Pianezzi, F.; Reinhard, P.; Chirilă, A.; Bissig, B.; Nishiwaki, S.; Buecheler, S.; Tiwari, A. N., Unveiling the Effects of Post-Deposition Treatment with Different Alkaline Elements on the Electronic Properties of CIGS Thin Film Solar Cells. *Physical Chemistry Chemical Physics* **2014,** *16* (19), 8843-8851.

56. Jiang, Y.; Yang, Y.; Qiang, L.; Fan, R.; Li, L.; Ye, T.; Na, Y.; Shi, Y.; Luan, T., A Detailed Study on the Working Mechanism of a Heteropoly Acid Modified TiO_2 Photoanode for Efficient Dye-Sensitized Solar Cells. *Physical Chemistry Chemical Physics* **2015,** *17* (10), 6778-6785.

3. Methodology

3.1. Fabrication Techniques

In this thesis, the device structure used was glass/fluorine-doped tin oxide (FTO)/TiO_2/Sb_2S_3/Spiro-OMeTAD (Spiro)/Au. This was chosen for a balance of safety (TiO_2 instead of CdS) and efficiency (Spiro-OMeTAD instead of CuSCN, and Au instead of Ag). Sb_2S_3 was chosen over Sb_2E_3 to allow for simpler study of underlying chemical mechanisms. The structure of the solar cell used is displayed in *Figure 3.1*.

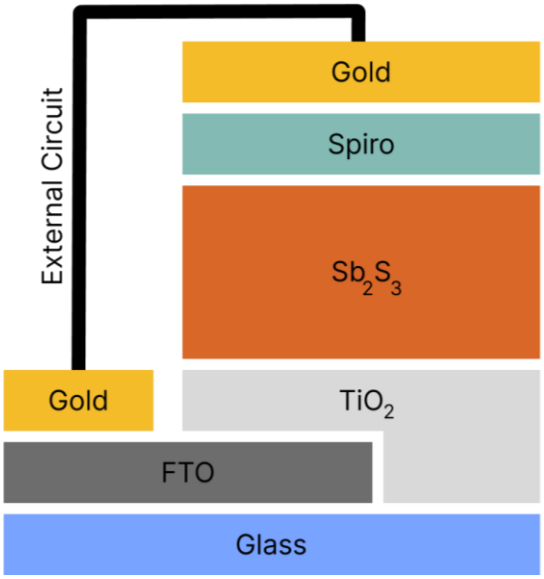

Figure 3.1: *Structure of the solar cells used in this thesis. A base layer of glass coated with fluorine-doped tin oxide (FTO) has a layer of TiO_2 selectively applied, followed by deposition of the bulk Sb_2S_3 layer. The Spiro-OMeTAD (Spiro) layer is added next, followed by the deposition of the gold electrodes. The external circuit connects between the contacts deposited directly on the FTO surface and the contacts on the top of Spiro.*

In order to form this structure, the cell required careful layering of each material to ensure there were no routes for the cell to short-circuit. *Figure 3.2* shows the top view of the solar cell structure used in this thesis, and details in which areas each material is deposited. The chosen layout first involved the etching of FTO under each working electrode (the working electrode is the upper gold contact in *Figure 3.1*) to ensure the connecting pin did not scratch through Sb_2S_3/TiO_2 to the FTO layer and cause a short circuit. Then, when the TiO_2 layer was deposited it was masked, and similarly the Sb_2S_3 and Spiro layers were etched once deposited, so that the counter electrodes lower gold contact in *Figure 3.1*) could directly contact only the

FTO layer. An Sb_2S_3 seed layer was used to provide better Sb_2S_3 film growth on TiO_2, based on the recipe of Zhang *et al*[1].

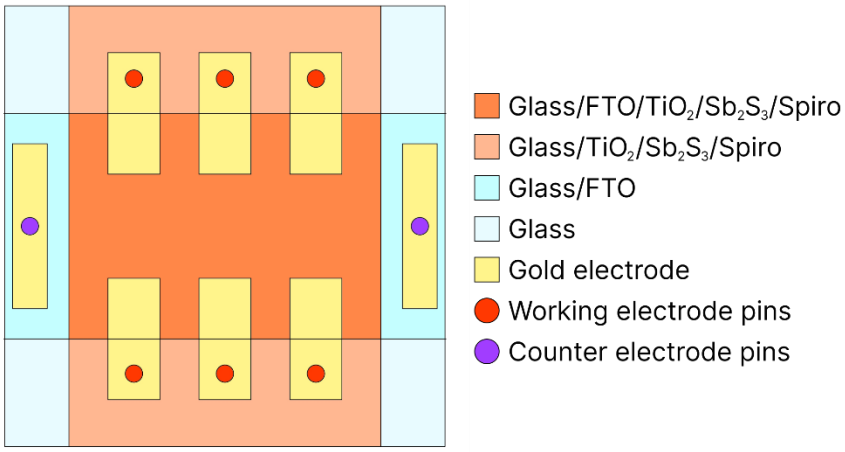

Figure 3.2: *Cell layout, as seen from the top, showing areas where FTO has been etched (lighter shade areas above and below central horizontal strip) and where TiO_2 was masked off (blue areas to the left and right of central vertical strip). Electrode positions and where pins would contact these electrodes are also shown. The cell has 6 active pixels, with two counter electrodes. Each pixel has an active area totalling the overlap of the working electrode with the central region.*

3.1.1. Deposition of TiO_2 and Sb_2S_3 Seed Films

FTO-coated glass (Merck product 735167-1EA; surface resistivity 7 Ω/sq) was etched using Zn metal (Sigma-Aldrich product 209988-1KG; ≥98%) and HCl (Sigma-Aldrich product 258148-2.5L; 37%) under the working electrode contact positions, shown in *Figure 3.2*. The substrate was then cleaned in sonication (Ultrawave model F0001602) in 2% Hellmanex III (Hellma Analytics product 9-307-011-4-507) in ultrapure water (type III deionised water, 18.2 MΩ, UV treated) for 30 minutes, then ultrapure water for 15 minutes, and finally EtOH (Sigma-Aldrich product 32221-2.5L-M; ≥99.8%) for 15 minutes. A TiO_2 precursor solution of 140 µL Ti(IV) isopropoxide (Sigma-Aldrich product 205273-500ML; 97%), 1.984 mL EtOH and 41.6 µL 1.25 M HCl in EtOH (Sigma-Aldrich product 17934-50ML; ~1.25M) was prepared. The clean FTO-glass was then spin coated (Ossila model E441) with 100 µL of this solution at 1650 rpm for 40 seconds, with the counter-electrodes masked off with polyimide tape (positions shown in *Figure 3.2*). The tape was removed and the substrates were placed into a TMS SNOL 8.2/1100

LHM01 muffle furnace overnight (550 °C, 2 °C/min ramp, hold for 50 mins) to yield the finished TiO_2 film.

An Sb_2S_3 seed solution was prepared by fully dissolving 0.1 g thiourea (VWR Chemicals product 28615.231; 99.6% assay) and 0.2 g antimony acetate (Sigma-Aldrich product 483265-100G; 99.99% trace metals basis) in a 252 µL dimethylsulfoxide (Fluorochem product 10080110; ≥99%) solution with ultrapure H_2O (0.8:0.03 v/v) in a N_2-filled MBraun MB20G glovebox. 1680 µL dimethylsulfoxide was then added dropwise. 100 µL of this Sb_2S_3 seed layer solution was spin coated (Laurell model WS-650S-6NPP/LITE) onto the TiO_2 film in the N_2-filled glovebox at 4000 rpm for 40 seconds. This was immediately followed by annealing of the film at 200 °C for 1 minute in the glovebox.

3.1.2. Hydrothermal (HT) Synthesis

Hydrothermal (HT) synthesis involves the mixing of reagents in a solvent, followed by the heating of that mixture in a pressurised chamber, called an autoclave. The general process is shown in *Figure 3.3*.

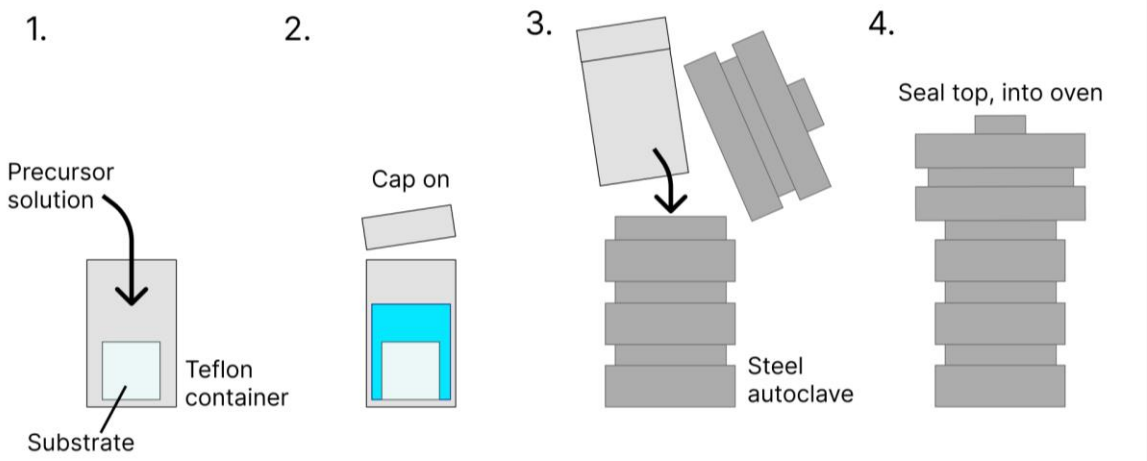

Figure 3.3: *Process of hydrothermal deposition of a material onto a substrate; 1. The precursor solution is loaded into a Teflon container containing the substrate, 2. A cap is applied, 3. The Teflon container is loaded into a steel autoclave, 4. The autoclave is sealed tightly, and loaded into a preheated oven for a set time.*

HT deposition involves the deposition of a film onto a substrate from precursor materials which are in solution. There are many proposed mechanisms for this deposition process, but

nanoparticle-based deposition and ion-based deposition are of particular interest for this thesis[2]. Nanoparticle-based deposition involves the spontaneous formation of nanoparticles (comprised of the material to be deposited) from the precursors in solution, followed by deposition of said nanoparticles onto the film. In this case, the film will end up rough, with uneven atomic distribution and a low crystallinity, since each nanoparticle is formed separately before deposition and will likely not fit well into the existing film surface. Ion-based deposition, on the other hand, involves the controlled release of precursor ions into solution, followed by the deposition of individual ions onto the substrate surface. In this case, the crystal growth is performed on the surface of the substrate rather than in solution, leading to a smoother, more crystalline and uniform film. The deposition of materials in HT synthesis can change between these behaviour modes based on the precursor materials used and the chemical environment they are in.

In order to perform HT synthesis, the seeded films from *Section 3.1.1* were removed from the glovebox and placed into 50 mL autoclaves. HT solutions were made up by dissolving an additive (7.5 $x10^{-5}$ moles) in 15 mL of a potassium antimony tartrate (PAT; Sigma-Aldrich product 244791-100G; ≥99%) solution (19 mM in ultrapure water), except for the standard which did not include an additive. This solution was then mixed with 15 mL of a sodium thiosulfate (STS; Thermo Scientific product 450622500; 99%) solution (220 mM in ultrapure water) and loaded into the autoclave with the film. The autoclaves were then placed into a preheated Binder FD 56 forced convection oven at 100 °C for 2 hours, after which heating was switched off and the autoclaves were left to cool overnight. The films were washed in ultrapure water, the glass side was wiped clean, and the Sb_2S_3 side was dried with nitrogen flow. The films were annealed in the N_2-filled glovebox at 350 °C for 10 minutes to yield the finished film.

3.1.3. Sb_2S_3 Solar Cell Device Assembly

In the N_2-filled glovebox, a Spiro solution was prepared of 1 mL chlorobenzene (Alfa Aesar product B21052.AP; 99%), 28.814 µL tert-butylpyridine (Sigma-Aldrich product 142379-25G; 98%), 9.5 µL Li bis(trifluoromethanesulfonyl)imide (Fluorochem product 010326; 99%) solution (520 mg/mL in MeCN) and 36.6 mg spiro-OMeTAD (Scientific Laboratory Supplies

product 902500-1G; ≥99.9%). 100 µL of this solution was spin coated onto the completed Sb_2S_3/TiO_2 film at 3000 rpm for 30 seconds. The film was then removed from the glovebox and heated at 100 °C for 10 minutes in air. The spiro on the edges of the cell (blue areas shown in *Figure 3.2*) were etched by dipping into acetonitrile (Fisher Scientific product 10660131; ≥99.9%), then the Sb_2S_3 was etched by dipping into a 5 M KOH (prepared from Fisher Scientific product 10366240; ≥86%) solution. The excess KOH solution was carefully wiped away once complete to avoid further etching of the central area. The etched cells were loaded into a thermal evaporator and the gold electrodes were deposited from pellets (Kurt J Lesker Company product EVMAUXX50G; 99.999%) evaporated at a pressure of approximately $5x10^{-6}$ mbar, at a rate of 0.5 Å/s, with a final thickness of 80 nm.

3.2. Aggregation Screening Test

The additive ($1.25 x10^{-5}$ moles) was dissolved in 2.5 mL of a PAT solution (38 mM in ultrapure water). If the additive did not fully dissolve, it was swirled vigorously for a few minutes. 2.5 mL of STS (440 mM in ultrapure water) was then added and the solution was swirled further to yield a homogenous solution. This solution was left in a vial to react and settle over the course of a week.

The additives used included nitrilotriacetic acid (Sigma-Aldrich product N9877-100G; ≥99%), ethylenediaminetetraacetic acid (Apex Bio product B7197; 98%), pentetic acid (Fluorochem product F319523; ≥98%), triethylenetetramine-N,N,N',N'',N''',N'''-hexaacetic acid (Thermo Scientific product 044737.04; 98%), 3,4,9,10-perylenetetracarboxylic dianhydride (Merck product 8209700100; 98%), creatinine (Acros Organics product 228940250; ≥99%), triethanolamine (Merck product 1083790250; 97%), 4,5-dimethyl-2-nitroaniline (Acros Organics product 116480250; 97%), 4-nitrophenol (Acros Organics product 157050050; 99%), pentafluoronitrobenzene (Sigma-Aldrich product 262218-5G; 98%), 1,1',1'',1'''-(ethane-1,2-diylbis(azanetriyl))tetrakis(propan-2ol) (Fluorochem product F222350; 95%), 4,4'-dithiobutyric acid (Sigma-Aldrich product C15605-10G; 95%), citric acid (Sigma-Aldrich product C7129-100G; ≥98%), diethylenetriaminepentakis(methylphosphonic acid) solution (Sigma-Aldrich product 36818-100ML-F; ~50% technical in HCl), ethylenediamine (Fluka product 02400; ≥99%), diglycolic acid (Sigma-Aldrich product 143073-100G; 98%), sebacic

acid (Sigma-Aldrich product 283258-5G; 99%), 12-aminododecanoic acid (Sigma-Aldrich product 159247; 95%), l-(+)-tartaric acid (Sigma-Aldrich product 251380-100G; ≥99.5%), N,N,N',N'-pentamethyldiethyldiethylenetriamine (Acros Organics product 416950250; ≥98%), nitrilotris(methylenephosphonic) acid (Sigma-Aldrich product 144797-100G; 50% in H_2O), acetic acid (Fisher Scientific product 10744361; ≥99.7%), hydrochloric acid (Sigma-Aldrich product 258148-2.5L; 37%) and phosphoric acid (Fisher Scientific product 10122010; ≥85%).

The aggregate was collected by decanting the water when settled, then refilling with fresh ultrapure water, sonicating and shaking to ensure unreacted PAT and STS would be removed. This process was repeated once more once the powder had again settled, and the final liquid was decanted once it had settled. The resulting wet powder was allowed to dry overnight to yield the final product.

3.3. Materials Characterisation

3.3.1. Powder X-Ray Diffraction (P-XRD)

Powder X-ray diffraction (P-XRD) is used both as a fingerprinting technique to identify crystalline compounds, and to find information on the degree of crystallinity and orientation of crystalline substances. Due to the similar size of X-ray wavelengths and atomic spacing (both on the 10^{-10} m, or Å scale), X-rays will diffract when passing through spaces between atoms. If the spaces between the atoms are regular and uniform in size (such as in a crystal lattice), then the resulting diffracted waves can constructively interfere and create a strong signal, as seen in *Figure 3.4*.

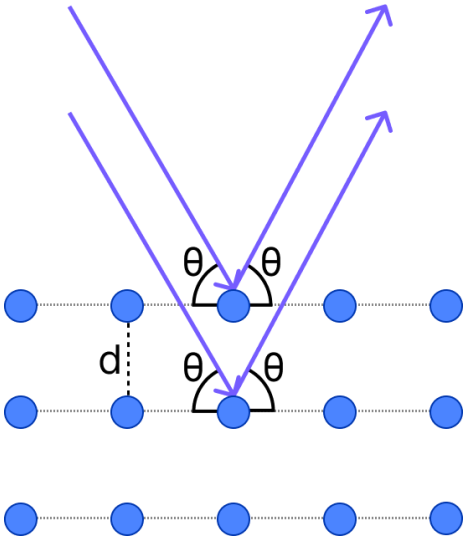

Figure 3.4: *Crystalline planes causing regular diffraction of X-rays, leading to constructive interference and a measurable signal; d, the lattice spacing, can be calculated using ϑ, the diffraction angle and the wavelength of light used.*

The angle at which the wave diffracts can be used to determine the distance between atomic planes using Bragg's law, shown in *Equation 3.1*. θ is the diffraction angle, λ is the wavelength of the X-ray and d is the spacing between the planes. For any values of λ and d, multiple values of θ may satisfy the conditions. The diffraction order (n_d) is an integer which accommodates this[3].

$$n_d\lambda = 2d \sin\theta \qquad \text{(Equation 3.1)}$$

By varying the angle at which the X-ray source and detector sit in relation to the sample (each at the same angle θ, opposite one another, as shown in *Figure 3.5*), a spectrum corresponding to each of the crystalline planes in a sample can be measured.

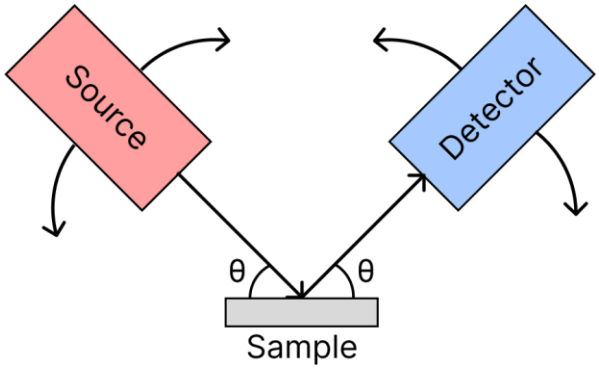

Figure 3.5: *Configuration of X-ray source and detector in a P-XRD setup; The source and detector are held opposite one another, each at an angle ϑ from one another, which is changed linearly during the experiment.*

If a crystalline plane is present and at the correct angle to constructively interfere, a signal will be seen, otherwise, if there is no plane present or it is not at the correct angle to constructively interfere, no signal will be detected. The intensity of the signal is proportional to the number of crystalline units with the corresponding lattice spacing. When measuring a film in P-XRD specifically, since the material is usually not a single crystal, the strength of the signal also corresponds to the relative orientation of the crystals in the film, which allows for the determination of crystalline orientation in deposited film[3].

An example P-XRD spectrum is shown in *Figure 3.6*. The angles of the incoming and outgoing X-rays are combined into a value of 2θ, measured in degrees (°). Each 2θ value corresponds to a specific spacing between the atoms as defined by *Equation 3.1*.

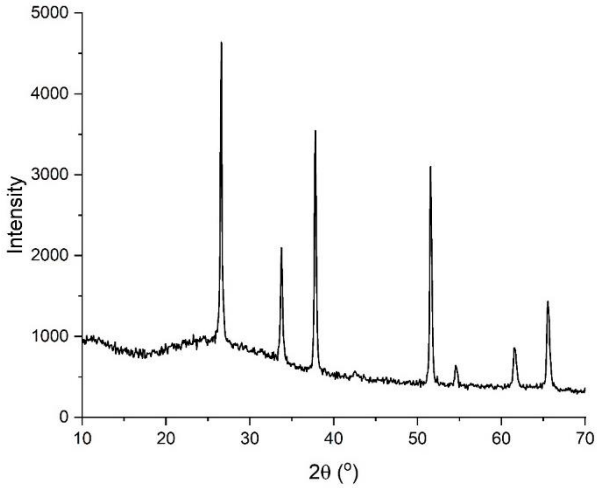

Figure 3.6: *Example of a P-XRD spectrum. Peak are shown at specific 2ϑ values corresponding to atomic spacings in the crystalline lattice; The intensity of the peak corresponds to the relative abundance of the relevant lattice spacing in the sample, in its measured orientation.*

Each plane has a set of miller indices (hkl) which define how it intersects the unit cell of the crystal. For example, the (001) plane only intersects the vertical direction vector of the unit cell once, giving a flat horizontal plane. (hk0) describes the set of planes which do not intersect the vertical direction vector, while (hk1) describes those that do intersect the vertical direction vector[3].

A value of texture coefficient (TC_{hkl}) can be calculated to yield information on the relative abundance of specific hkl signals in a sample in comparison to a standard. The formula for TC_{hkl} is shown in *Equation 3.2*, where I_{hkl} is the measured intensity of a peak corresponding to miller indices hkl, and I^0_{hkl} is the intensity of the same peak for a standard sample of the material (usually from a single crystal analysis).

$$TC_{hkl} = I_{hkl}/I^0_{hkl} \qquad (Equation\ 3.2)$$

In this thesis, the growth of Sb_2S_3 as (hk1) is preferred, as it indicates that the Sb_2S_3 ribbons are orientated perpendicularly to the substrate, yielding favourable charge transport. P-XRD data was collected on a Bruker D2 Phaser benchtop powder X-ray diffractometer with Cu Kα radiation (λ = 1.54184 Å). TC_{hkl} calculations were standardised to an ICSD standard for Sb_2S_3 (collection code 30779).

3.3.2. Atomic Force Microscopy (AFM)

Atomic force microscopy (AFM) is a technique used to measure the surface morphology of films. The deflection of a cantilever is precisely measured by a laser as the cantilever moves across the surface of the film, giving relative height data for each measurement point. A diagram of this is shown in *Figure 3.7.* The cantilever can operate in contact or tapping modes, either dragging the cantilever tip across the surface of the film, or tapping at a fixed amplitude, which is then disturbed by contact with the surface. Since contact mode may damage samples and as the tip runs along the surface, tapping is used for most samples. The contact mode also increases the likelihood of the tip picking up debris, which will alter the oscillation frequency of the tip and affect measurements[3].

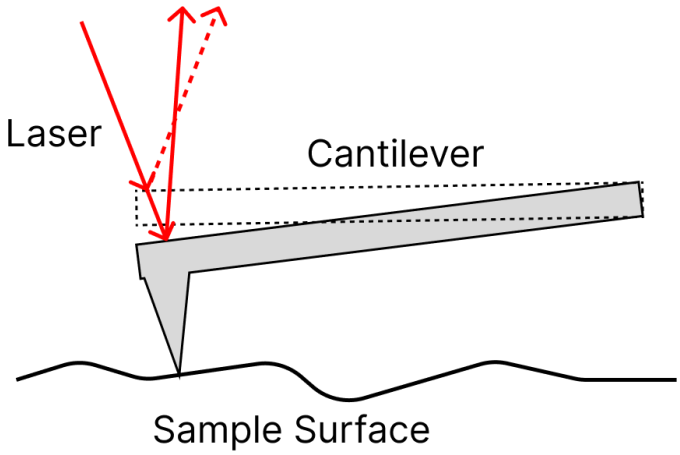

Figure 3.7: *Diagram of atomic force microscopy (AFM) cantilever as it passes over the surface of a film; The deflection of the cantilever, and subsequently the height of the film at that point, are measured by the deflection of a laser off of the cantilever.*

AFM data was measured in a 30 µm x 30 µm area with 256 x 256 samples at a rate of 0.5 samples per second on a Bruker Nanoscope V atomic force microscope.

3.3.3. Scanning Electron Microscopy (SEM) and SEM Energy-Dispersive X-Ray Spectroscopy (EDS)

Scanning electron microscopy is a technique used to image surfaces at a very high resolution (in the low nm range). It involves the scanning of a focussed electron beam over the surface of a sample. The electrons are accelerated towards the surface by a voltage, known as the 'accelerating voltage' and upon impact, they release other electrons and radiation from the surface through various mechanisms, illustrated in *Figure 3.8*. Secondary electrons are the most commonly used signal for SEM imaging, and are formed when the electron beam ionises the elements within the sample, and they emit another 'secondary' electron. These electrons can only escape from within the first few nanometres of the sample, so it is well suited for imaging surface morphology. Backscattered electrons can also be used for imaging, however due to their higher energy they are detected from deeper in the sample, since they are not as easily reabsorbed as secondary electrons. This results in the lateral resolution of backscattered electrons being around 1 µm, compared to secondary electrons, which are much more focussed at 10 nm[3, 4].

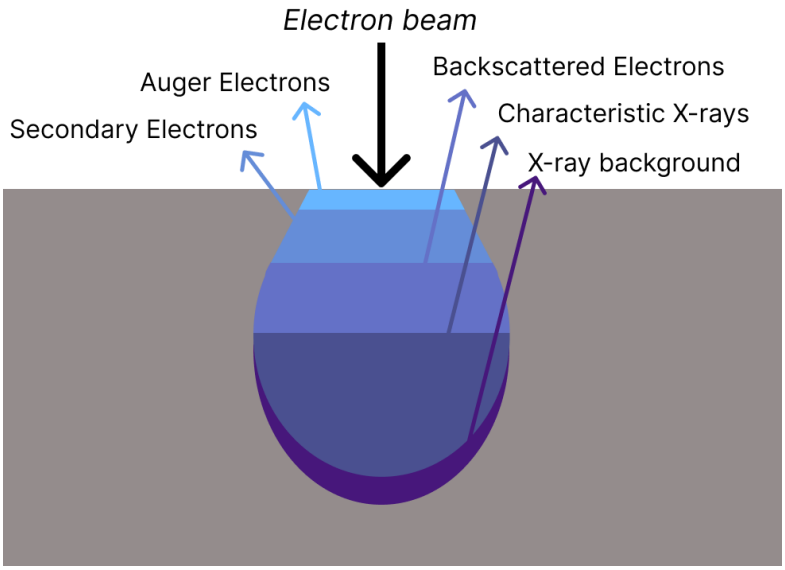

Figure 3.8: *The various emissions of a surface after an impacted SEM beam in the 'teardrop' shaped interaction volume.*

The electron beam also yields compositional information. Auger electrons are caused by the electron beam displacing an inner shell electron of an impacted atom, followed by the falling of an outer shell electron from that same atom to fill the gap. The characteristic energy of this drop is given to yet another electron, which is emitted from the atom as an Auger electron. While they can be formed deep in the material, Auger electrons only have escape depths of a few nanometres, so are used for surface analysis of elemental composition. If this characteristic energy is not given to an Auger electron, it is instead emitted as an X-ray. This X-ray is characteristic of the element which was hit, allowing for accurate determination of elemental composition. This technique is known as energy-dispersive X-ray spectroscopy (EDS). Due to the penetrative nature of X-rays, the entire volume of electron collisions can be measured for X-ray emissions, including where electrons have slowed due to multiple collisions. Where electrons have slowed, a background of X-ray emissions is detected, which is usually subtracted from the signal before analysis due to the varied energies of the emitted radiation. Due to the shape of the interaction volume of the electron beam, EDS often penetrates through thinner films, and this must be accounted for when performing analysis[5].

SEM samples were prepared with a 4 nm conductive Pd coating and measured at a working distance (distance between electron beam emitter and sample) of 7 mm at an accelerating voltage of 10 kV using a Carl Zeiss SIGMA HD VP Field Emission SEM. EDS data was collected and processed using Oxford Instruments Aztec ED X-ray analysis software.

3.3.4. Raman Spectroscopy

Raman spectroscopy is used to attain chemical bonding information. When light of a set wavelength is shone onto a sample, vibrational modes in the molecules scatter the light at a characteristic frequency which can be measured. This is measured as a wavenumber ($\tilde{\nu}$; cm^{-1}) which is defined as shown in *Equation 3.3*.

$$\tilde{\nu} = \omega/2\pi c \qquad (Equation\ 3.3)$$

Where $\omega = (k_f/\mu)^{-1/2}$ and $c = 2.998 \times 10^8$ m/s. k_f is the force constant of the bond, which increases with increasing bond strength. μ is the effective mass, defined in *Equation 3.4* for two atomic masses m_1 and m_2.

$$\mu = (m_1 m_2)/(m_1 + m_2) \qquad (Equation\ 3.4)$$

If $m_1 >> m_2$, then μ is low and approximates m_2, meaning the vibrational motion of the bond is almost entirely performed by m_2. So, the wavenumber will be higher for bonds with a higher strength (or force constant, k_f) and when the effective mass is low (i.e. $m_1 >> m_2$). Therefore, a weak bond between similarly sized atoms (e.g. a metal-metal bond) will be at a low $\tilde{\nu}$, while a strong bond between differently sized atoms (e.g. O-H) will be at a high $\tilde{\nu}$.

Often, however, Raman spectroscopy is simply used as a fingerprinting technique. A known spectrum is compared to a measured one, and if they match, it is good evidence that the substances are the same[3, 5].

Raman spectra were measured with light of wavelength 785 nm using a Thermoscientific DXR3 at a power of 0.2 mW. Each measurement was taken for 20s with 3 repeats.

3.3.5. Nuclear Magnetic Resonance Spectroscopy (NMR)

Nuclear magnetic resonance spectroscopy (NMR) is a technique used to determine details of molecular structures. In order to yield a signal, the molecule must have one or multiple nuclei which have a nuclear spin quantum number $I > 0$, known as 'NMR active'. The most common NMR active nucleus is ^1H, which has $I = ½$. From this number, the number of components of angular momentum $m_I\hbar$, can be determined, where $m_I = I\text{-}1, \ldots, I$. For ^1H, these would be $m_I = ½$ and $m_I = -½$[3].

Absorption of the applied electromagnetic radiation can occur when the resonance condition, shown in *Equation 3.5*, is fulfilled. In this equation, $h = 6.626 \times 10^{-34}$ Js, ν = frequency of applied electromagnetic field, γ_N = the nuclear magnetogyric ratio (empirically determined value specific to internal structure of a nucleus), $\hbar = h/2\pi$ and B_0 = external magnetic field in T.

$$h\nu = \gamma_N \hbar B_0 \qquad \text{(Equation 3.5)}$$

By applying a magnetic field, the components m_I are separated in energy, as shown in *Figure 3.9*. When this separation matches the value $\gamma_N\hbar B_0$, resonance occurs and the absorption of radiation can be measured as a peak.

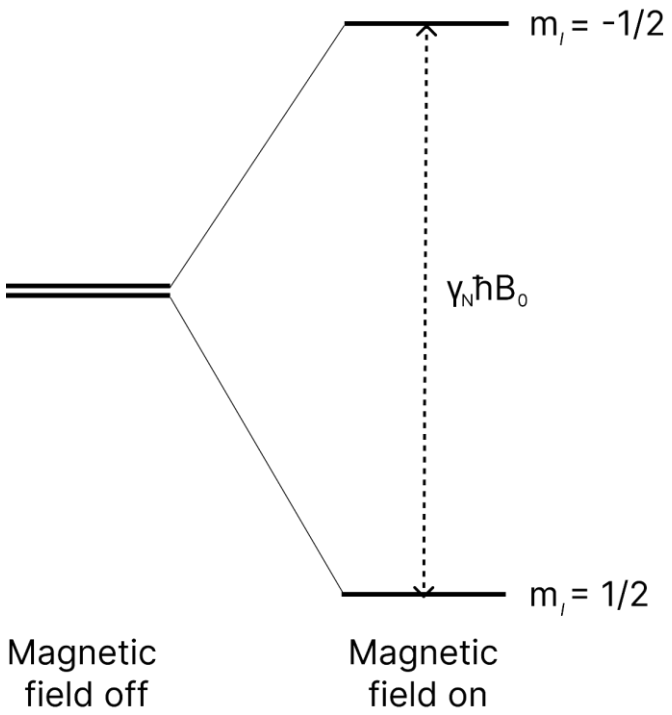

Figure 3.9: *Separation of angular momentum components in an I = ½ nucleus under the application of an external magnetic field B_0; If the separation of the m_I energies are equal to $\gamma_N \hbar B_0$, resonance occurs.*

The resonant frequency of a specific nucleus in a molecule is measured as a chemical shift, shown in *Equation 3.6*, where ν_0 is the resonant frequency of the standard, and the chemical shift, δ, is measured in ppm. The chemical shift of a nucleus changes based on its surrounding electron density. Electrons, due to their motion, create a magnetic field which opposes B_0. Therefore, higher electron density 'shields' the nucleus from B_0, and moves the chemical shift to a lower value. Conversely, lower electron density 'deshields' the nucleus and moves the chemical shift to a higher value.

$$\delta = (\nu - \nu_0)/\nu_0 \times 10^6 \qquad \text{(Equation 3.6)}$$

In addition, nuclei in close proximity can couple together and cause the formation of fine structure in a spectrum. For a standard ^{1}H spectrum, any number of equivalent H atoms (N) spaced 2 or 3 bonds apart from a H atom in a different chemical environment will result in the second H atom signal splitting into N+1 signal lines. For splitting by an equivalent group of

atoms, the spacing between these lines, known as the coupling constant (J), will be the same. The peak intensities also follow Pascal's triangle due to the way that the signals overlap (1:1, 1:2:1, 1:3:3:1, etc). These patterns are known as singlets, doublets, triplets, etc. for patterns of 1, 2, 3, etc. peaks.

This splitting effect may also occur when equivalent atoms experience changes in their environment, however in this case the spacing between the lines and the intensities of the peaks depend on the electronic structure of those various environments and the relative probabilities of being in any one state, rather than based on Pascal's triangle and a set J value.

Solutions were prepared in deuterium oxide (D_2O; Sigma-Aldrich product 151882-100G; 99.9% atom % D). NMR spectra were collected on a Bruker Avance Spectrometer δ_H(500MHz; D_2O; Me_4Si).

3.3.6. X-Ray Fluorescence (XRF)

X-ray fluorescence (XRF) is a technique used to determine the elemental composition of a sample. It works in much the same way as EDS, described in *Section 3.3.3*, whereby the ionisation of a core electron from an atom can cause an electron from an outer orbital to drop down and emit an X-ray which is characteristic of that transition, and that element. The ionisation of electrons in XRF is achieved by exposure to short-wavelength X-rays of a particular wavelength. Different atoms require different X-ray powers to yield good signals, so measurements may be done at multiple power levels to get a good range. However, lighter elements such as C, N and O still do not give good signal strength because despite them absorbing the X-rays effectively, their emitted X-rays are too low energy and simply get reabsorbed before they can be detected effectively. Thus, while XRF is a useful and powerful technique, it cannot be used effectively for organic molecule analysis unless specifically built with controls in place to increase the sensitivity to allow it to do so[5].

XRF measurements were performed using a Bruker S2 PUMA energy-dispersive XRF using X-ray tubes in three conditions; 50 kV at 1 mA with 250 µm Cu filter, 40 kV at 1.25 mA with 500 µm Al filter, and 20 kV at 2 mA with no filter.

3.3.7. Thermogravimetric Analysis (TGA)

Thermogravimetric analysis (TGA) is used to examine the thermal degradation and/or reaction of a compound. A sample is placed onto a precise balance and heated at a steady rate. The resulting loss of mass due to thermal degradation, and/or gain of mass due to reaction with compounds in the air, are recorded by the balance as a function of time and temperature[5].

In this thesis, the sample was heated from 25 to 800 °C at a rate of 10 °C per minute using a Netzsch STA 449C.

3.3.8. pH Testing

pH is a logarithmic scale which describes the acidity, or concentration of hydrogen ions, $[H^+]$, in an aqueous solution. A pH of 7 is neutral, the point at which $[H^+] = [OH^-]$ (at ambient temperature). The value of pH is equal to the $-\log_{10}[H^+]$, so conversely, $[H^+] = 10^{-pH}$ [5].

In this thesis, pH testing was measured with a Hanna Instruments HI98103 pH tester, calibrated against a Hanna Instruments HI70007P 7.01 pH buffer solution. To take a measurement, the probe was cleaned with ultrapure water, partially dried by dabbing onto paper, then inserted into the solution to be tested. It was gently swirled until a stable reading could be taken.

3.4. Solar Cell Characterisation

Solar cells are characterised primarily using four performance metrics; short circuit current density (J_{SC}; mA cm^{-2}), open-circuit voltage (V_{OC}; V), fill factor (FF) and power-conversion efficiency (PCE, also known as 'efficiency'; %). The J_{SC}, V_{OC} and FF are all found from the J-V plot of the solar cell measured under simulated sunlight. J-V plots are explained in more detail in *Section 3.4.1*. PCE is the ratio of the power input to the cell by incoming light to the power output by the cell as electricity, and can be calculated from the J_{SC}, V_{OC} and FF using *Equation 3.7*.

$$PCE = P_{out}/P_{in} = (V_{OC}J_{SC}FF)/P_{in} \quad (\textit{Equation 3.7})$$

Where P_{out} is the output power of the solar cell (equivalent to the product of V_{OC}, J_{SC} and FF; mW cm^{-2}) and P_{in} is the power input (from the light source; mW cm^{-2}).

The simulated sunlight is usually calibrated to a standard of 100 mW cm^{-2} under a solar spectrum of AM1.5G. The term AM1.5G denotes the amount of air mass (AM), or atmosphere, that the sunlight would pass through on its way to the ground, with AM1 being a direct path perpendicular to the surface, and AM1.5 being 1.5x that amount of air. The G (for 'global') means that it considers additional factors such as the tilt of the ground relative to the angle of the sun (as the light would be spread over a larger area). The AM1.5G spectrum is shown in *Figure 3.10*[6, 7].

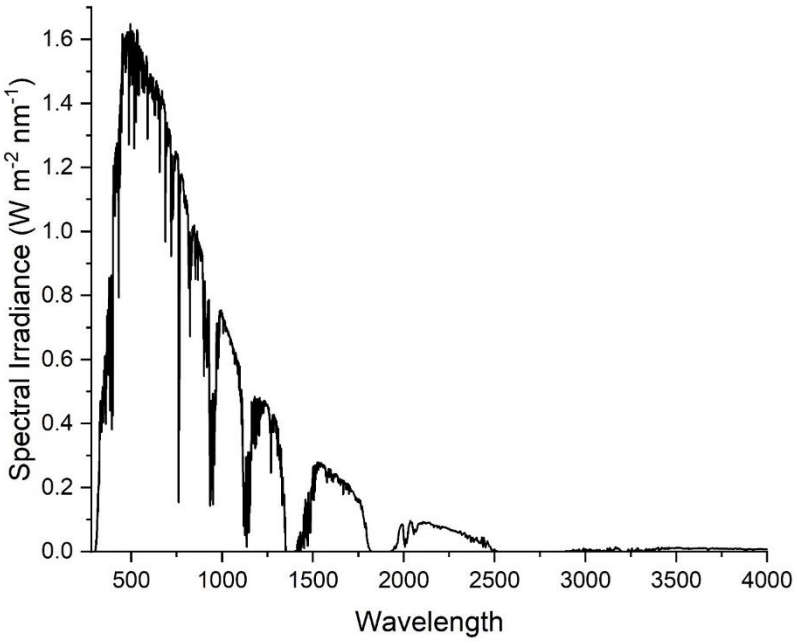

Figure 3.10: *AM1.5G standard solar spectrum in the range of 280-4000 nm.*

3.4.1. Current Density vs Voltage (J-V) Curves

To measure the performance of a solar cell, J-V curves are measured under both illumination (simulated sunlight of AM1.5G at 100 mW cm^{-2}) and in the dark. An external voltage sweep is

applied and the output voltage and current of the cell are measured. An example of a curve measured under illumination is shown below in *Figure 3.11*.

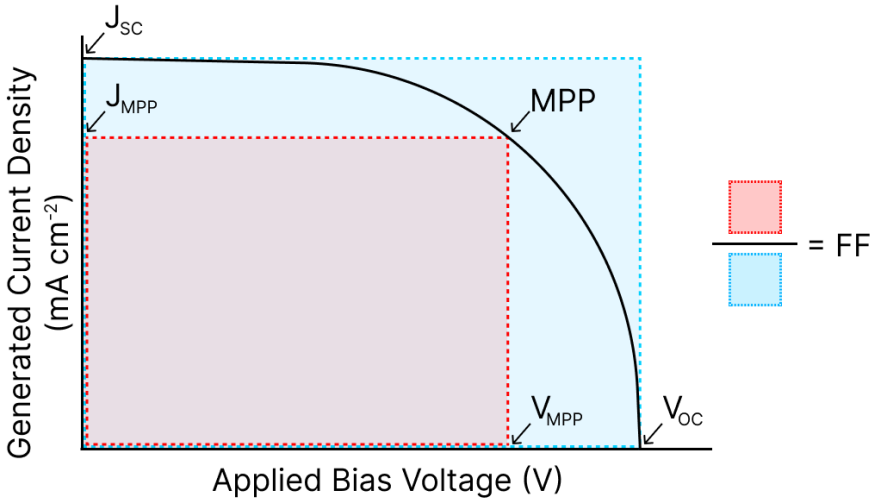

Figure 3.11: *Example of a current-density vs voltage (J-V) curve; Short circuit current density (J_{SC}), open circuit voltage (V_{OC}), and maximum power point (MPP) are annotated. Fill factor (FF) may be calculated by dividing the area of the red rectangle by the area of the blue rectangle ($J_{MPP}V_{MPP}/J_{SC}V_{OC}$).*

There are three main points of interest on a J-V curve; 1) short circuit, where applied bias is 0 and maximum current is attained (J_{SC}), 2) open circuit, where the applied bias equals and opposes the generated voltage of the cell (V_{OC}), and 3) the maximum power point (MPP), which shows where the cell generates the maximum power density (product of voltage and current density). FF can be calculated with these values using *Equation 3.8*, which is equivalent to the ratio of the areas marked in red and blue in *Figure 3.11*.

$$FF = V_{MPP}J_{MPP}/V_{OC}J_{SC} \qquad (Equation\ 3.8)$$

Where V_{MPP} and J_{MPP} are the voltage and current at the MPP, respectively. The fill factor is a good measure of how well the cell conducts charge carriers and how well it resists recombination. The visualisation in *Figure 3.12* shows how an increase in series resistance (R_S), or a decrease in shunt (recombination) resistance (R_{sh}) will lead to a decreased FF. As seen

in *Equation 3.7*, the PCE is a product of each of the three J_{SC}, V_{OC} and FF, so if one term is decreased, the overall efficiency of the cell can drop considerably.

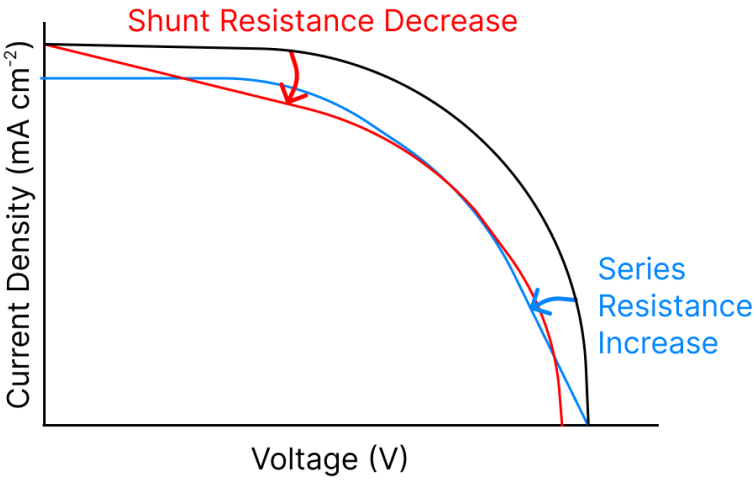

Figure 3.12: *Effects of shunt resistance and series resistance on the shape of a J-V curve; An increase in series resistance and/or a decrease in shunt resistance result in reduced FF.*

In addition to measuring J-V curves under illumination, they are also measured in darkness to evaluate the diodic behaviour of the solar cell. The measured dark curve appears very similar in shape to the light curve, but shifted downwards so that the output current under short circuit is 0. As a bias is applied, eventually a current is forced through the cell and can be seen in the J-V curve. The current density of an ideal cell in the dark is given by *Equation 3.8*.

$$J = J_0 \, e^{(qV/nkT)} - 1 \qquad \text{(Equation 3.8)}$$

Where J = net current density, J_0 is the dark saturation current density, q is the electron charge constant (1.602 $x10^{-19}$ C), V is the applied bias voltage, n is the ideality factor (a measure of how well the cell acts like a diode), k is Boltzmann's constant (1.38 $x10^{-23}$ J/K) and T is the temperature in K.

The value of J_0 helps determine the potential at which current will start to flow more freely. It is an indication of recombination mechanisms in the device, and a larger saturation current will indicate a larger level of recombination.

For values of V > ~0.1V, the exponential term in *Equation 3.8* dominates and the equation can be approximated as *Equation 3.9*.

$$J = J_0 e^{(qV/nkT)} \qquad \text{(Equation 3.9)}$$

By approximating as such, the natural logarithm of both sides can be taken to yield *Equation 3.10*.

$$\ln(J) = \ln(J_0) + qV/nkT \qquad \text{(Equation 3.10)}$$

Finally, *Equation 3.10* can be plotted as a semi-log graph (ln(J) vs V) in order to attain additional information, including the ideality factor (from the reciprocal of the slope), a readable value of J_0 and information on the internal resistances of the cell. An example of such a graph is shown in *Figure 3.13*.

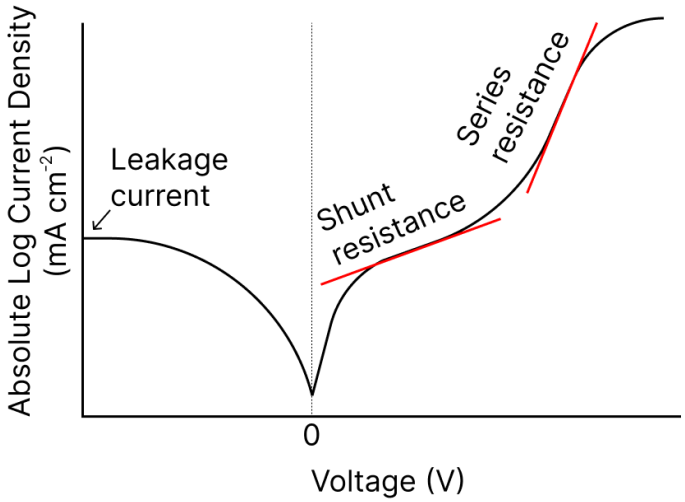

Figure 3.13: *Example of a dark J-V curve; Leakage current and areas of the curve which are affected by series and shunt resistance are annotated.*

A real cell will also have series and shunt resistances, which can be modelled by adding resistance terms to *Equation 3.9* to yield *Equation 3.11*[8].

$$J = J_0 e^{(q(V - JR_s)/nkT)} + (V - JR_s)/R_{sh} \quad \text{(Equation 3.11)}$$

In the semi-log plot, these terms yield the effects shown in *Figure 3.14*, whereby a large R_s will lower the slope in the region of higher applied bias voltage, while a large R_{sh} will increase the slope in the region of lower applied bias voltage. As such, the values of R_s and R_{sh} can be approximated by these regions in the semi-log dark J-V curves.

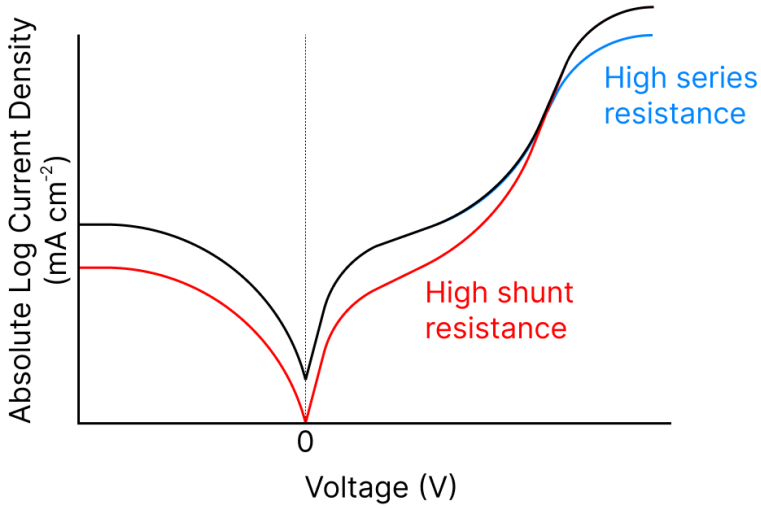

Figure 3.14: *Effects of shunt and series resistance on the shape of a dark J-V curve.*

J-V measurement was carried out using an AM1.5G Sciencetech SLB300A solar simulator with 601-300 power supply and a Keithley 2450 sourcemeter to apply bias voltage. The scans were done from -0.5 V to 1.5 V at 0.125 V/s with a step size of 0.035 V. The active area of the device was 0.04785 cm^2, made using an aluminium mask.

3.4.2. External Quantum Efficiency

External quantum efficiency (EQE) describes the ability of a device to convert incoming photons to charge carriers which have left the device. EQE is measured per-wavelength of light and standardised against a silicon reference. First, the power of the lamp is calibrated by dividing the measured current of the Si detector at each wavelength by the responsivity of the silicon reference (provided by the manufacturer when calibrated, in A W^{-1} nm^{-1}). The detector

and subsequent samples must be placed at the same distance and location relative to the lamp after this has been done. The measured sample current at each wavelength (λ) is then divided by the power attained during calibration, yielding the responsivity of the sample. The responsivity at a given wavelength (R_λ) can be converted to EQE using *Equation 3.12*, where h = 6.626 x10^{-34} Js, c = 2.998 x10^{17} nm s^{-1} and q = 1.602 x10^{-19} C[9, 10].

$$EQE = hcR_\lambda/q\lambda \approx 1240R_\lambda/\lambda \quad \text{(Equation 3.12)}$$

This can be plotted against the wavelength to attain an EQE versus wavelength curve, which gives information about how efficiently the solar cell converts absorbed photons to current at each wavelength.

To attain the value of J_{SC} from EQE, the photon flux (ϕ) for the AM1.5G solar spectrum is calculated from the spectral irradiance (H) using *Equation 3.13*[7, 11].

$$\phi = (\lambda H/hc) \quad \text{(Equation 3.13)}$$

From this and the EQE, the J_{SC} can be calculated using *Equation 3.14* and checked against the value attained from the J-V curves.

$$J_{SC} = \int q\, \phi_\lambda\, EQE_\lambda\, d\lambda \quad \text{(Equation 3.14)}$$

This is an important measurement for the honest reporting of solar cell results, as solar simulator setups can vary wildly from lab to lab due to ambient conditions, lamp distances, mask setups, etc. By standardising against EQE, the effects of these differences on over- or under-reporting cell performances can be minimised.

EQE measurements were taken using a dual-source quartz halogen and xenon lamp setup (Bentham ILD_75E powered by 2x Bentham 610 power sources with Bentham 418 optical chopper controller and 2-slot chopper blade) which was monochromated (Bentham TMc300 Monochromator), passed through a mask (square 1.5 mm) and focussed onto the sample. A reference silicon diode (Bentham DH-Si) with a known responsivity at the same fixed distance was used to calculate the EQE of the device. Data was collected using a Stanford Research Systems Model SR830 DSP lock-in amplifier connected to the cell.

3.5. References

1. Zhang, L.; Lian, W.; Zhao, X.; Yin, Y.; Chen, T.; Zhu, C., Sb_2S_3 Seed-Mediated Growth of Low-Defect Sb_2S_3 on a TiO_2 Substrate for Efficient Solar Cells. *ACS Applied Energy Materials* **2020,** *3* (12), 12417-12422.

2. Wang, X.; Tang, R.; Jiang, C.; Lian, W.; Ju, H.; Jiang, G.; Li, Z.; Zhu, C.; Chen, T., Manipulating the Electrical Properties of $Sb_2(S,Se)_3$ Film for High-Efficiency Solar Cell. *Advanced Energy Materials* **2020,** *10* (40), 2002341.

3. P. Atkins, J. d. P., *Atkins' Physical Chemistry*. 10th ed.; Oxford University Press: 2014.

4. Zhou, W.; Apkarian, R.; Wang, Z.; Joy, D., Fundamentals of Scanning Electron Microscopy (Sem). 2006; pp 1-40.

5. M. Weller, T. O., J. Rourke, F. Armstrong, *Inorganic Chemistry*. 6th ed.; Oxford University Press: 2014.

6. M. O'Kane, F. W. The AM1.5 Spectrum. https://www.ossila.com/pages/standard-solar-spectrum (accessed 15/11/2024).

7. Laboratory, N. R. E., Reference Air Mass 1.5 Spectra.

8. C. Honsberg, S. B. Impact of Both Series and Shunt Resistance. https://www.pveducation.org/pvcdrom/solar-cell-operation/impact-of-both-series-and-shunt-resistance (accessed 15/11/2024).

9. Kumar, K.; Kaur, D., A Review on Recent Advancements in the Growth of MoS_2 Based Flexible Photodetectors. *Solar Energy Materials and Solar Cells* **2024,** *268*, 112736.

10. A. Rogalski, K. A., J. Rutowski, *Narrow-Gap Semiconductor Photodiodes*. SPIE Press: 2000.

11. C. Honsberg, S. B. Spectral Irradiance. https://www.pveducation.org/pvcdrom/properties-of-sunlight/spectral-irradiance (accessed 15/11/2024).

4. Mechanisms of EDTA as an Additive in Sb_2S_3 Solar Cells

4.1. Introduction

Ethylenediaminetetraacetic acid (EDTA) is a commonly used additive in a wide variety of applications including pharmaceuticals, food and toxic waste remediation[1-4]. Its main feature is the ability to effectively and selectively chelate positively charged metal ions. Chelation is the process of a molecule binding to another atom/molecule (usually an ion) through multiple binding sites[3]. This increases the strength by which the chelating molecule is bound to the atom/molecule as, in order to separate them, multiple bonds must be broken in sequence. The chemical structure of EDTA and a schematic example of how it chelates to a metal ion are shown in *Figure 4.1*.

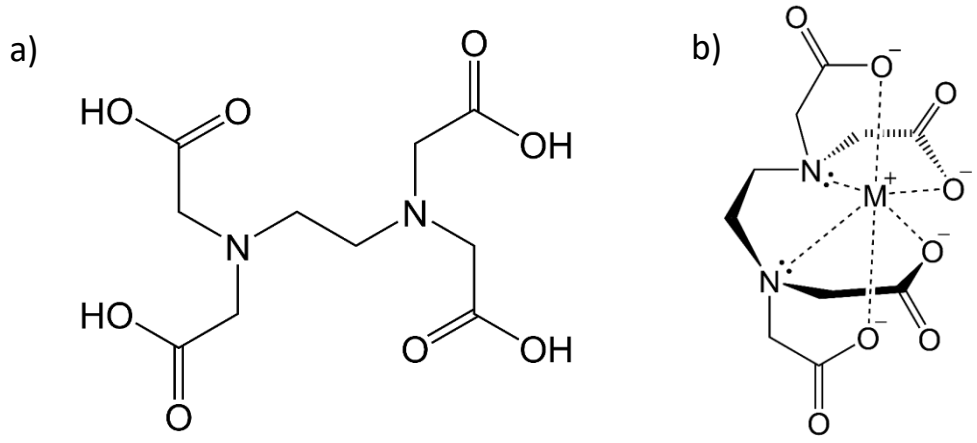

Figure 4.1: *a) Structure of ethylenediaminetetraacetic acid (EDTA), and b) schematic of how EDTA can very strongly chelate to a positively charged metal ion (M^+)*

EDTA also finds frequent use as a complexing agent in film deposition, including for Sb_2E_3. The first use of EDTA for depositing Sb_2E_3 was in 1991, where Sb-complexed EDTA was used as an antimony source to do an alkaline bath deposition of Sb_2S_3[5]. Later, in 2010, it was used to shift the hydrothermally deposited Sb_2S_3 from forming irregular particles to forming single-crystal nanotubes[6]. The most recent development, and most relevant for this thesis, came in 2020 when EDTA was used directly as an additive in Sb_2E_3 solar cells and achieved the record efficiency for that time of 10.5%[7].

However, as discussed in *Chapter 2*, despite EDTA's high performance, the underlying mechanistic understanding of how EDTA performed this role was not directly evidenced. Based on observations of increased film thickness and the reduction of dispersed $Sb_2(S, Se)_3$

particulates after hydrothermal deposition, the proposed working mechanism of EDTA was that it enabled highly dispersed potassium antimony tartrate (PAT) during the hydrothermal deposition process, and that it shifted the deposition process from preformed particle-based to ion-based via EDTA coordinating to Sb[7]. More dispersed PAT would increase availability of precursor materials, promoting the faster film growth which was observed. Shifting from particle-based to ion-based means that instead of large, preformed $Sb_2(S, Se)_3$ particles depositing on the film (thereby creating a disordered and rough crystal), individual S, Se and Sb ions deposit one-by-one, allowing it to form an ordered crystal with a smooth surface. In order to prove whether these were indeed the mechanisms by which it operated, this work explores two avenues:

1) The use of nuclear magnetic resonance spectroscopy (NMR; *Section 3.3.5*) to determine the nature of EDTA binding in the presence of hydrothermal precursors (*Section 4.3.1*)
2) The investigation of the formation of aggregates in precursor solution in ambient conditions with and without EDTA (*Section 4.3.2*)

Before this, however, the efficacy of EDTA in the chosen system of Sb_2S_3/TiO_2 needed to be established. Even though EDTA was shown to improve Sb_2S_3 film quality and improve the efficiency of $Sb_2(S, Se)_3$ cells, it had not yet been proven that it improves the efficiency of Sb_2S_3 cells, nor was it yet proven to improve performance when using a TiO_2 substrate.

4.2. Confirmation of the Effectiveness of EDTA as an Additive in Sb_2S_3/TiO_2 Solar Cells

To confirm the effectiveness of EDTA as an additive in my chosen system, standard (additive-free) and EDTA-containing films were deposited and fabricated into corresponding solar cells. The TiO_2 and Sb_2S_3 films were prepared as detailed in *Section 3.1.1* and *Section 3.1.2*, and cells were prepared as detailed in *Section 3.1.3*. The quality of the prepared films was analysed using powder X-ray diffraction (P-XRD; *Section 3.3.1*), atomic force microscopy (AFM; *Section 3.3.2*), scanning electron microscopy (SEM; *Section 3.3.3*), SEM energy-dispersive X-ray spectroscopy (EDS; *Section 3.3.3*) and Raman spectroscopy (*Section 3.3.4*). The results of these

experiments are presented and discussed in *Section 4.2.1* below. The performance of the fabricated solar cells was measured using current density-voltage (JV; *Section 3.4.1*) curves and external quantum efficiency (EQE; *Section 3.4.2*), the results of which are presented and discussed in *Section 4.2.2*.

4.2.1. Film Quality

From initial inspection, the standard (additive-free) Sb_2S_3 film appeared rough and pale compared to the EDTA Sb_2S_3 film, which was shiny and reflective. This suggested that the surface of the Sb_2S_3 film was smoother after the use of EDTA. An image of the films is shown below in *Figure 4.2*.

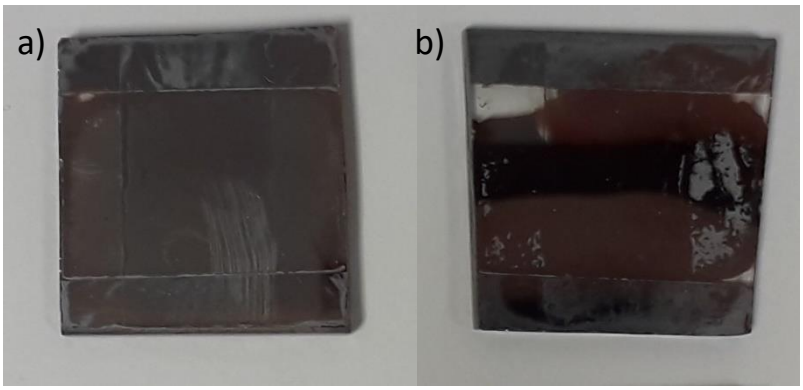

Figure 4.2: *Example films of Sb_2S_3 prepared with a) no additive (standard) and b) EDTA.*

To investigate the effect of EDTA on the crystallinity of the formed Sb_2S_3 film, P-XRD was used. In literature, EDTA both improved the overall crystallinity of the film and improved the texture coefficient (details in *Section 3.3.1*) of the (221) and (211) diffraction peaks[7]. Similar results were seen for the cells in this work (shown in *Figure 4.3)*, with increases in intensity for the (211) peak at 29.3° and (221) peak at 32.4° upon the use of EDTA. The $TC_{(211)}$ increased from 0.37 for the standard to 0.43 for EDTA, and the $TC_{(221)}$ similarly increased from 0.30 to 0.37. Unexpectedly, the standard appeared to contain a large amount of Sb_2O_3 (shown by the large peak at ~28°), which may have explained the pale appearance of the film. It is worth noting that the (221) peak of Sb_2S_3 is close to a peak of Sb_2O_3 at 32°, and that the peak seen in the standard film at this value corresponds to Sb_2O_3, not to the (221) peak of Sb_2S_3. Interestingly, upon using EDTA, Sb_2O_3 was entirely removed, with no Sb_2O_3 peaks present in the EDTA-prepared film. Sb_2O_3 is an electrical insulator, and so can act as a recombination centre. It is a

known side-product in Sb_2E_3 solar cells, and the suppression of Sb_2O_3 by EDTA is a benefit not previously reported[7-11]. An apparent increase in film roughness upon annealing led to the hypothesis that somehow this Sb_2O_3 was forming during the annealing process, and that the presence of EDTA prevented its formation. However, it was unclear where the oxygen required for its formation was coming from, as annealing was always performed under an inert nitrogen atmosphere.

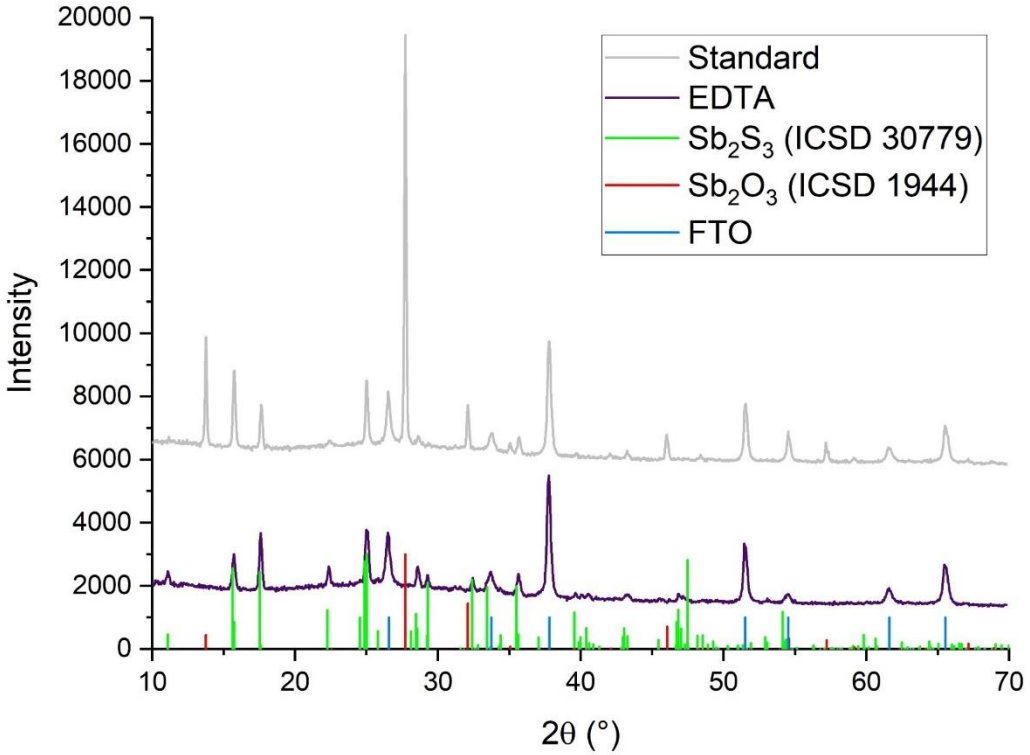

Figure 4.3: *P-XRD of standard and EDTA Sb_2S_3 films; Inorganic Crystal Structure Database (ICSD) standards for Sb_2S_3 (collection code 30779)[12, 13] and Sb_2O_3 (collection code 1944)[12, 14] and internal fluorine-doped tin oxide (FTO) standard are overlaid as stick diagrams.*

To investigate the surface of the films, AFM scans of both film surfaces were taken, shown in *Figure 4.4*.

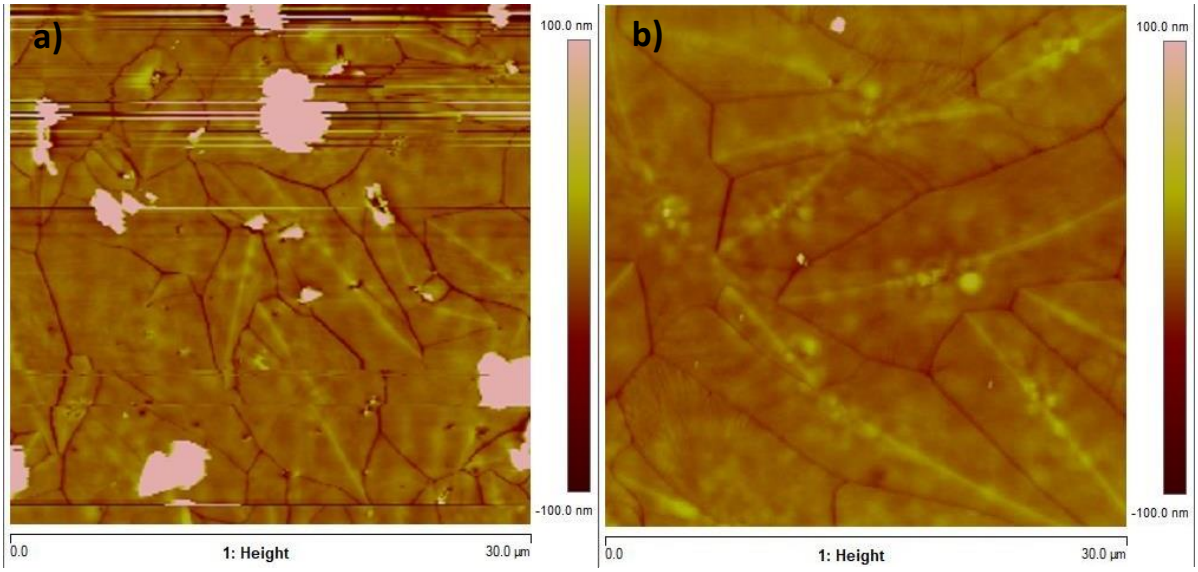

Figure 4.4: *AFM scans of a) the standard Sb_2S_3 film surface and b) the EDTA Sb_2S_3 film surface; Both were measured with an area of 30x30 µm and height range of -100 to 100 nm. The standard film has multiple large formations on the surface, which caused some horizontal streaks due to rapid height variation.*

The EDTA film was smooth, with distinct crystal domains. The standard film was unfortunately very rough, which can be seen by the bright spots, indicating a formation over 100 nm high. It was clear to see that the grain size was greatly increased by EDTA, with large distinct domains of ~10-30 µm, compared to the standard, which had ~5-15 µm These formations were all over the film, and several µm in size. Given the P-XRD results showing a large Sb_2O_3 content in the standard film, it was likely that these were crystals of Sb_2O_3.

The nature of the surface formations of the standard film was further investigated using SEM imaging, shown in *Figure 4.5*. So far only the annealed, crystalline Sb_2S_3 films were investigated, but to determine whether the hypothesis about Sb_2O_3 forming during annealing was correct, some unannealed, amorphous Sb_2S_3 film samples were also measured to see if Sb_2O_3 was present.

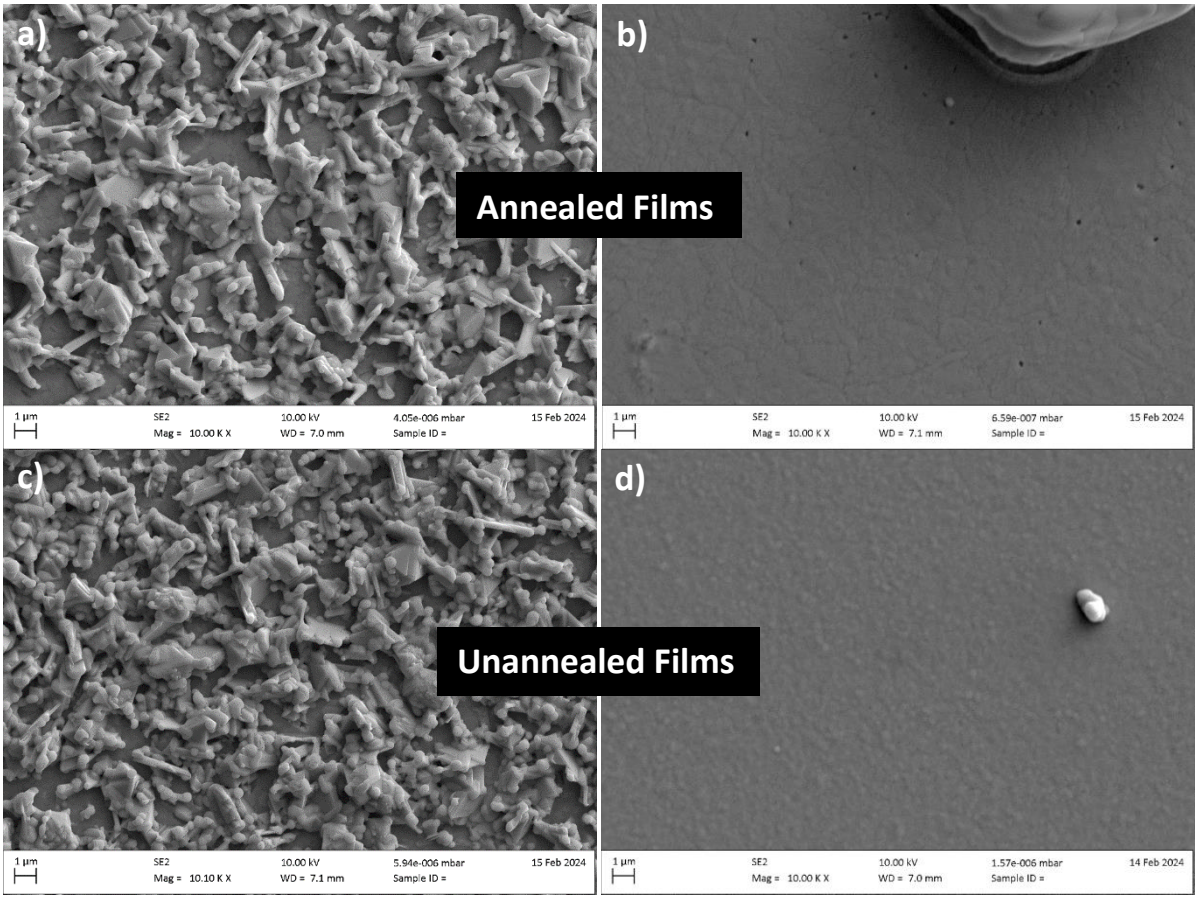

Figure 4.5: *SEM scans of the annealed a) standard and b) EDTA Sb_2S_3 film surfaces and unannealed c) standard and d) EDTA Sb_2S_3 film surfaces*

Large, uneven formations were seen on the surfaces of the annealed and unannealed standard films, in similar quantities. If these formations were indeed Sb_2O_3, then it would mean that the majority of the Sb_2O_3 forms during the initial deposition of the film, rather than during the annealing process. This would make sense given the prior concern regarding the source of the oxygen for forming Sb_2O_3 given that annealing was done under inert N_2. Interestingly, there were also some formations on the EDTA film, and it was unclear if these too could be trace amounts of Sb_2O_3.

The EDTA film had distinct pinholes which only appeared after annealing. This was consistent with the observations of Huang *et al.* when they found that during annealing, the Sb_2S_3 film will lose excess sulfur, and pinholes form as a way for this sulfur to escape[15]. Unfortunately, these pinholes negatively impact cell performance by providing pathways between the electrodes, causing that area of the cell to short-circuit. The surface of the standard film is

hidden by the uneven formations, so no details on the role of EDTA in the promotion/suppression of these pinholes can be determined from these results.

Two techniques were employed to probe the nature of the surface formations on both of the annealed films; EDS (*Table 4.1* and *Table 4.2)* and Raman spectroscopy mapping (*Figure 4.6)*. EDS showed that the formations on the surface of the standard film were indeed Sb_2O_3. They had high amounts of Sb and O, with very little S. Meanwhile, the surface below the formations was largely Sb and S (and some Ti and O from the TiO_2 of the underlying substrate). EDS also showed that the surface formations on the EDTA film were not Sb_2O_3, but instead Sb_2S_3, as there was very little O present but plenty of S.

Table 4.1: *EDS results for main film and surface formations of standard and EDTA films; Values are displayed in relative weight percentage (wt%). Measurements for both the film surface and surface formations were averaged over at least three measurements on at least three separate parts of the film.*

Sample	**Sb (wt%)**	**S (wt%)**	**O (wt%)**	**Ti (wt%)**	**Sn (wt%)**	**C (wt%)**	**N (wt%)**
Standard main film	39	11	11	3.4	32	3.1	0.53
EDTA main film	48	16	6.0	2.7	23	3.1	0.93
Standard surface formations	81	1.1	14	0.00	0.00	3.2	0.36
EDTA surface formations	68	24	1.3	0.13	0.53	4.5	1.3

It is clear to see from *Table 4.1* that the surface formations on the standard film were largely Sb_2O_3, while on the EDTA film, the formations were instead formed of Sb_2S_3. However, the values shown in *Table 4.1* for the films should not be taken at face value. For example, despite the standard main film and surface formation having similar O values, some of the O in the main film was incorporated into the underlying TiO_2 and FTO substrate layers, which were being reached by the scanning envelope of the EDS beam through the Sb_2S_3 layer (more details

on this effect in *Section 3.3.3*). To accommodate for the Ti and Sn content of the main films, the weight percentage can be adjusted to relative atomic abundances, as shown in *Table 4.2*. The values have all been multiplied by 2 to allow for easy comparison of Sb:S and Sb:O ratios for Sb_2S_3 and Sb_2O_3.

Table 4.2: *EDS results for main film and surface formations of standard and EDTA films; Values are displayed in relative atomic abundance, relative to the amount of Sb present. The values have all been multiplied by 2 to show how closely each sample follows the Sb_2S_3 atomic ratio. Measurements for both the film surface and surface formations were averaged over at least three measurements on at least three separate parts of the film. Oxygen abundances adjusted by removing the oxygen incorporated into TiO_2 and SnO_2 are shown in brackets.*

Sample	**Sb**	**S**	**O**	**Ti**	**Sn**	**C**	**N**
Standard main film	2.0	2.1	4.5 (0.22)	0.44	1.7	1.6	0.24
EDTA main film	2.0	2.5	1.9 (-0.59)	0.28	0.96	1.3	0.33
Standard surface formations	2.0	0.10	2.7 (2.7)	0.00	0.00	0.80	0.08
EDTA surface formations	2.0	2.6	0.28 (0.2)	0.01	0.02	1.3	0.34

By assuming that the TiO_2 and FTO layers were stoichiometric and each had 2 O per Ti/Sn, the oxygen content incorporated elsewhere could be estimated. The bracketed O values in *Table 4.2* show these calculated values. However, by assuming this exact stoichiometry, the films themselves gave quite low values, and for the case of EDTA, a negative value. As such, they may instead have a lower relative abundance of O, thus meaning that it is not exactly two O atoms per Ti/Sn. Therefore, the fact the standard film O value was positive suggests that (assuming the TiO_2/FTO films are consistent between the samples) the standard film contains a larger amount of O than the EDTA film, even accounting for the underlying FTO and TiO_2 layers. This, along with the lower ratio of S:Sb observed for the standard film versus the EDTA

film, suggests that there is some amount of Sb_2O_3 present in the film and not just on the surface.

The ratio of Sb:O in the standard surface formations was approximately 2:3, with very little S present, strongly suggesting that the standard surface formations were primarily Sb_2O_3. Meanwhile, the EDTA surface formations had very little O present, with instead a nearly 2:3 ratio of Sb to S. This confirmed that these were not the same formations as the standard surface and were instead a similar composition to the main EDTA film.

Some C and N content were observed in each sample. These were attributed to environmental factors such as dust, and some potential leftover residue from the precursors and EDTA. Some of the O content may have also been attributed to this source as PAT, STS and EDTA all contained some O.

Raman mapping (*Figure 4.6*) further confirmed that the surface formations were Sb_2O_3; the areas which showed the 190 cm^{-1} signal (corresponding to Sb_2O_3) overlapped with the areas where the formations were observed in the optical microscope image.

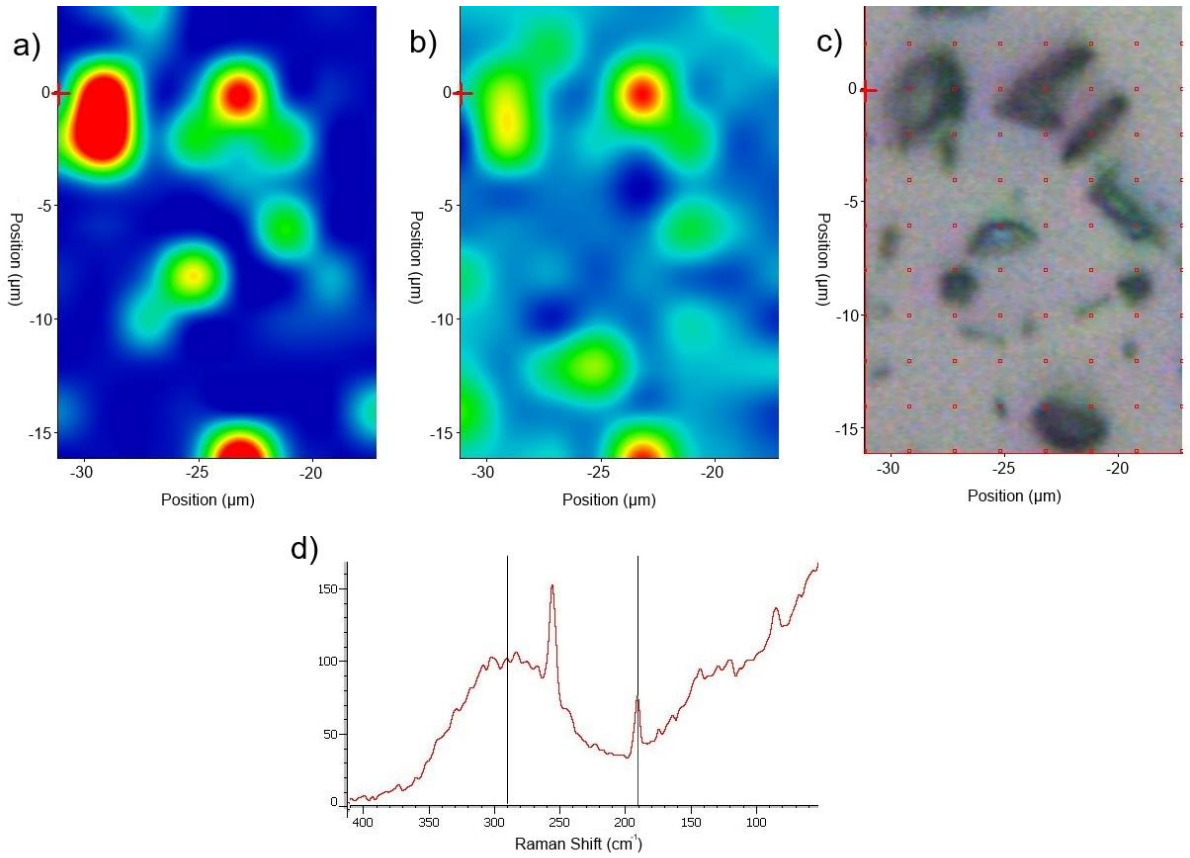

Figure 4.6: *Raman spectroscopy map of a standard film; a) Raman signal of 190 cm^{-1}, corresponding to Sb_2O_3,[16] b) Raman signal of 290 cm^{-1}, corresponding to Sb_2S_3,[17] c) an optical image of the same region and d) the combined Raman signals of Sb_2S_3 and Sb_2O_3, with lines denoting the positions of the signals at 190 and 290 cm^{-1}.*

Overall, the film quality drastically improved upon the addition of EDTA, with the enhancement of hk1 diffraction peaks, film smoothness and grain size, and additionally, the complete suppression of the Sb_2O_3 formations which were seen in the standard film. The next step was to test whether these film quality improvements translated directly into increased solar cell efficiency.

4.2.2. Solar Performance

The films from *Section 4.2.1* were fabricated into full solar cells using the methods described in *Section 3.1.3*. The current density-voltage (JV; *Section 3.4.1*) curves of the champion standard and EDTA cells under light and dark are shown in *Figure 4.7*. The light curve shows that EDTA increased across all of the performance metrics, with V_{OC} increasing from 0.62 V to

0.66V, J_{SC} increasing from 10.1 mA cm^{-2} to 12.1 mA cm^{-2} and FF increasing from 0.46 to 0.52, leading to an overall increase in the power conversion efficiency (PCE) from 2.88% to 4.14%. In the dark curve, the leakage current for EDTA was approximately two orders of magnitude lower, showing that the EDTA cell operated more effectively as a diode. The EDTA sample was also shifted down by a similar amount around 0 V, suggesting that shunt resistance (R_{sh}) was greatly increased for the EDTA sample. This explained the increased FF and V_{OC} of the EDTA cell. Additionally, the value of current density at high voltage was increased for EDTA meaning the series resistance (R_s) is decreased, which in turn explained both the J_{SC} improvements and further explaining the FF increase. Overall, the EDTA cell improved solar performance considerably through both the reduction of R_s and increase of R_{sh}, likely due to the removal of Sb_2O_3, improved crystallinity and crystal orientation.

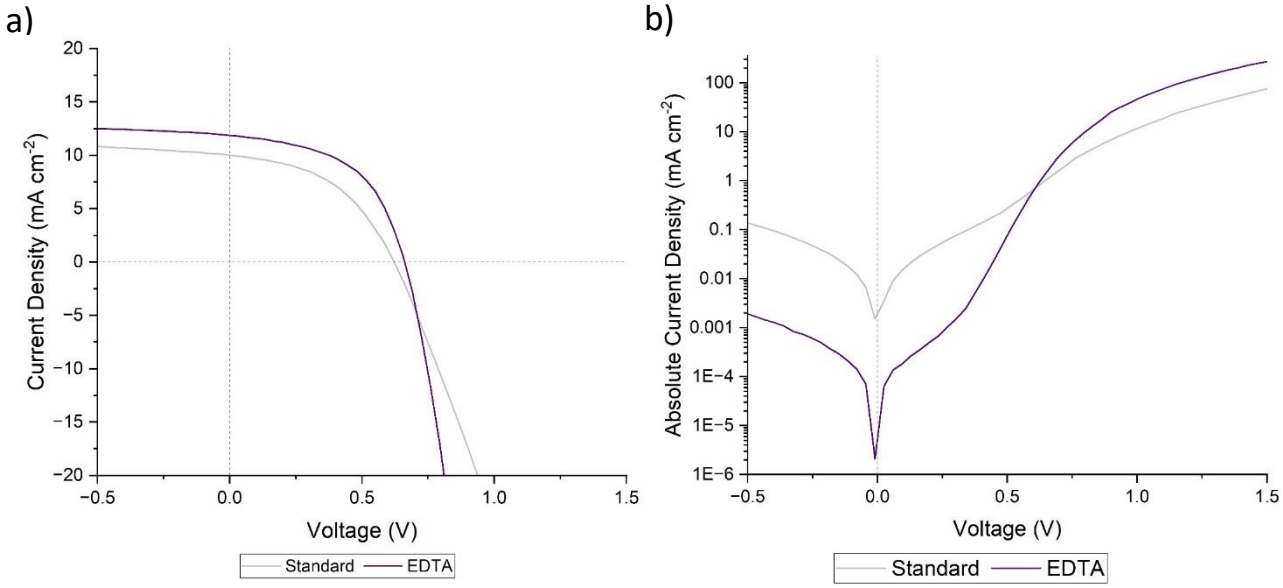

Figure 4.7: *JV curves in a) light (AM1.5G, 100 mW cm^{-2}) and b) dark of champion solar cells using no additive (standard) and EDTA.*

The cell statistics are shown in *Figure 4.8*. As seen in the JV curves, EDTA saw an overall improvement in every category, leading to a consistent average improvement in PCE. The average (±standard deviation) values for each metric increased even more significantly than the champion values, and the standard deviations decreased, showing increased consistency in performance when using EDTA over no additive. The V_{OC} increased from 0.52 ±0.2 V to 0.62 ±0.02 V, the J_{SC} increased from 8.94 ±1.5 mA cm^{-2} to 10.9 ±1.2 mA cm^{-2}, the FF increased from 0.39 ±0.08 to 0.48 ±0.03, leading to an overall increase in average PCE of 1.95 ±0.9% to 3.23 ±0.6%.

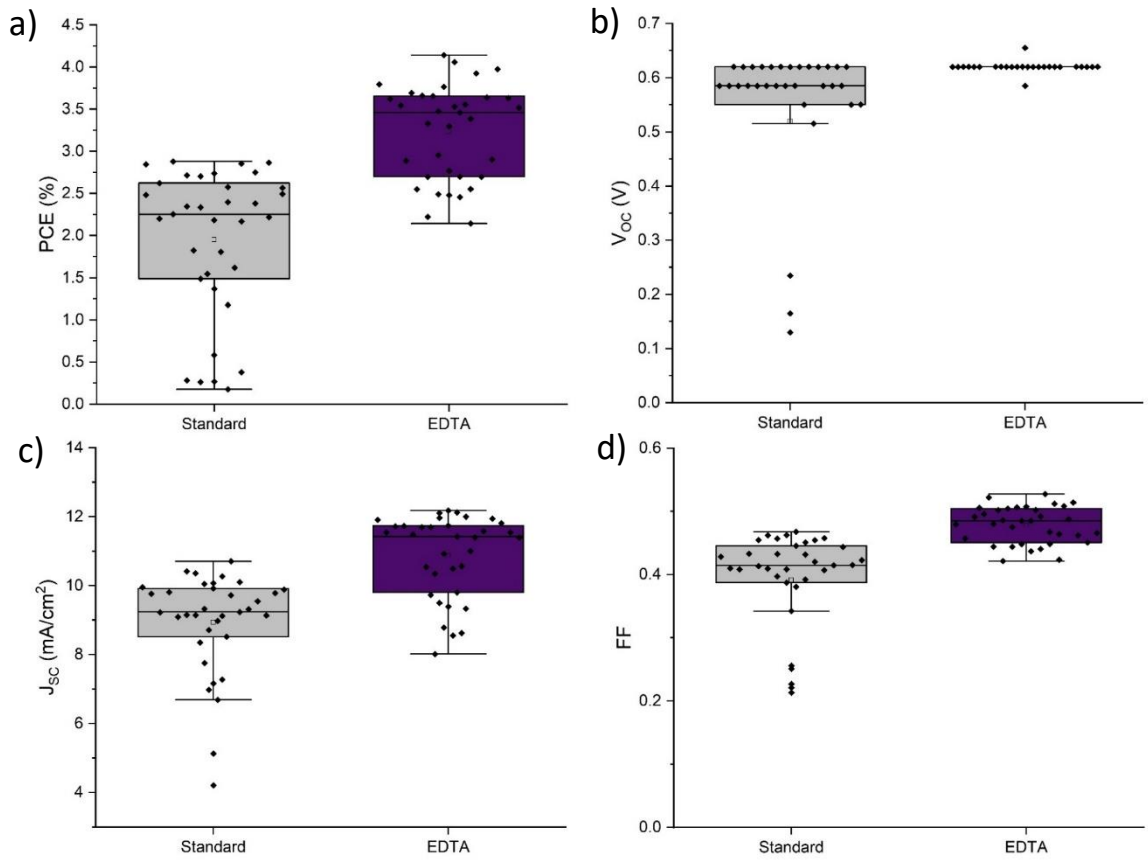

Figure 4.8: *Solar cell performance statistics a) PCE, b) V_{OC}, c) J_{SC} and d) FF for standard and EDTA solar cells; Overall, 6 cells were fabricated, with each cell containing 6 pixels, giving a total of 36 data points for each standard and EDTA. The cells were fabricated over the course of 3 experimental runs. One pixel of each type was fully shunted, yielding no solar performance, so were excluded from the data.*

To further evaluate the effects of EDTA on solar performance, external quantum efficiency measurements (EQE; *Section 3.4.2*) were performed on the champion cells, shown in *Figure 4.9*. EQE describes the proportion of the photons which are absorbed which are utilised in generating an external electric current. Thus, recombination within the cell reduces the EQE by 'wasting' some of the absorbed energy. The EQE was increased for almost all effective wavelengths when using EDTA, thereby indicating an overall decrease in recombination in the cell when using EDTA. The EQE can also be integrated to yield a trace of J_{SC} per wavelength (process described in *Section 3.4.2*), allowing a way of confirming the value of J_{SC} acquired from the JV curve. In this case, the JV values of 10.1 mA cm^{-2} for the standard and 12.2 mA cm^{-2} for EDTA were confirmed with the respective values of 10.1 and 12.2 mA cm^{-2} in EQE.

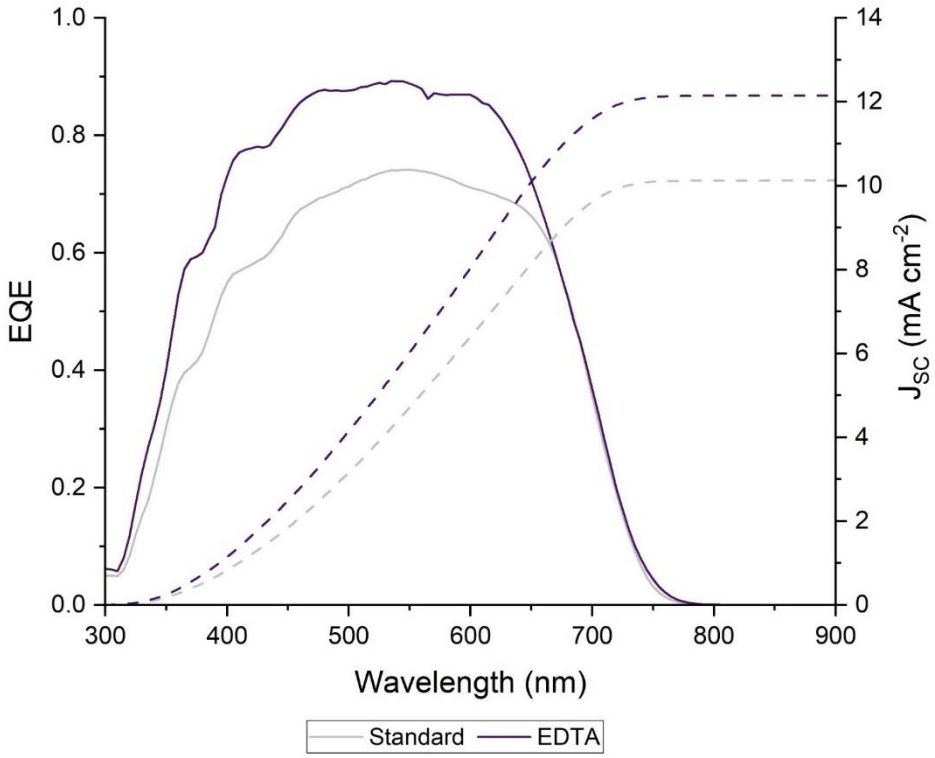

Figure 4.9: *External quantum efficiency (EQE), left axis, and corresponding J_{SC} trace, right axis, of champion standard and EDTA solar cells.*

Overall, the performance of EDTA in Sb_2S_3/TiO_2 cells rivalled and even exceeded the benefits seen in the original study[7]. This was primarily due to a large increase in R_{sh} and a decrease in R_s when utilising EDTA. The additional benefits seen over the original study were likely from the Sb_2O_3 suppression effect of EDTA. Now that the effectiveness of EDTA in this system had been proven, investigation of its working mechanisms could be undertaken.

4.3. Investigation of EDTA Mechanisms

To test the claims made for the function of EDTA, two tests were planned; NMR spectroscopy (*Section 3.3.5*) would be used to investigate the nature of EDTA binding to Sb in solution with potassium antimony tartrate (PAT), and a solution-based aggregation test (*Section 3.2*) would then be used to test the claim that EDTA reduces aggregation of Sb_2E_3 in the hydrothermal solution.

4.3.1. NMR Spectroscopy

Various solutions were prepared for NMR spectroscopy (*Section 3.3.5*). Each solution was prepared in D_2O to ensure an equivalent solvent environment to that used for hydrothermal solutions. Solutions were prepared at half the concentration of that used in the regular hydrothermal solutions. Initially, a solution containing potassium antimony tartrate (PAT) and sodium thiosulfate (STS) was prepared. The resulting ^1H NMR spectrum can be seen in *Figure 4.10*.

Only one signal was expected; a singlet for the 'backbone' hydrogens of PAT. STS does not contain hydrogens, so was not expected to yield any signal. A strong singlet was seen at 4.74 ppm, which logically corresponded to the expected PAT signal. The low intensity signals seen at 4.87, 4.71 and 4.59 and 4.37 ppm were of unknown origin, though were very weak compared to the PAT signal. Of these, the largest integral peak at 4.37 ppm was broad, indicating a hydrogen exchange process[18]. This corresponded to some unknown interaction between STS and PAT, discussed below.

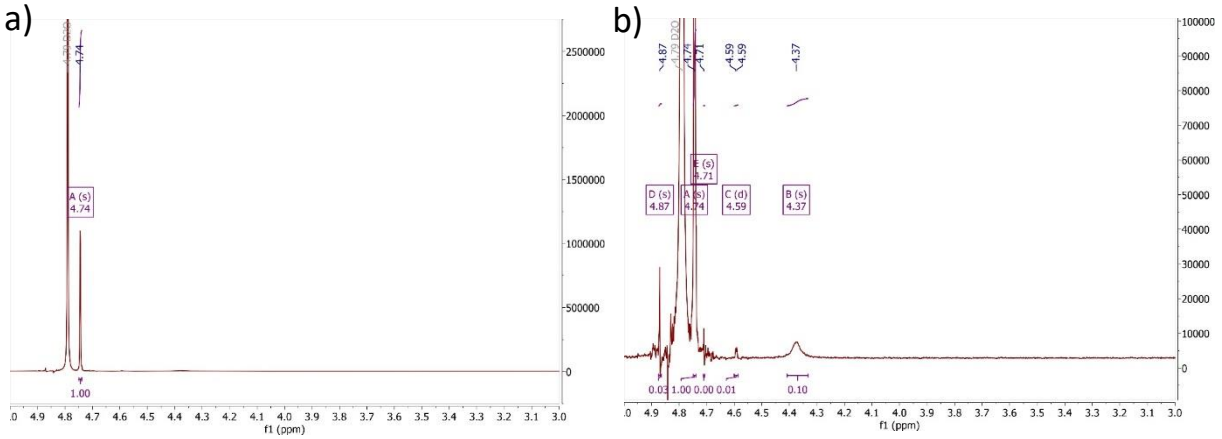

Figure 4.10: *The a) overall and b) zoomed in ^1H NMR spectrum of a solution of both PAT and STS in D_2O at half the concentrations used in hydrothermal synthesis.*

To look at the effects of EDTA, four NMR solutions were prepared in D_2O; EDTA on its own, EDTA in a PAT solution, EDTA in an STS solution, and EDTA in a solution of both PAT and STS. The resulting ^1H NMR spectra are shown in *Figure 4.11*. EDTA on its own had two distinct signals at 3.94 ppm and 3.62 ppm. The signal at 3.94 ppm had an integral ~2x that of the integral of the 3.62 ppm peak, meaning there were two times the number of hydrogens for that signal. This led to the assignments of the 3.94 ppm peak as the 'arm' -CH_2 groups of EDTA (shown as blue in *Figure 4.11.a*), and the 3.62 ppm peak as the 'core' -CH_2 groups (shown as

red in *Figure 4.11.a*). This agreed with the literature values of EDTA (after accounting for the effect of pH shifting the ppm values)[3].

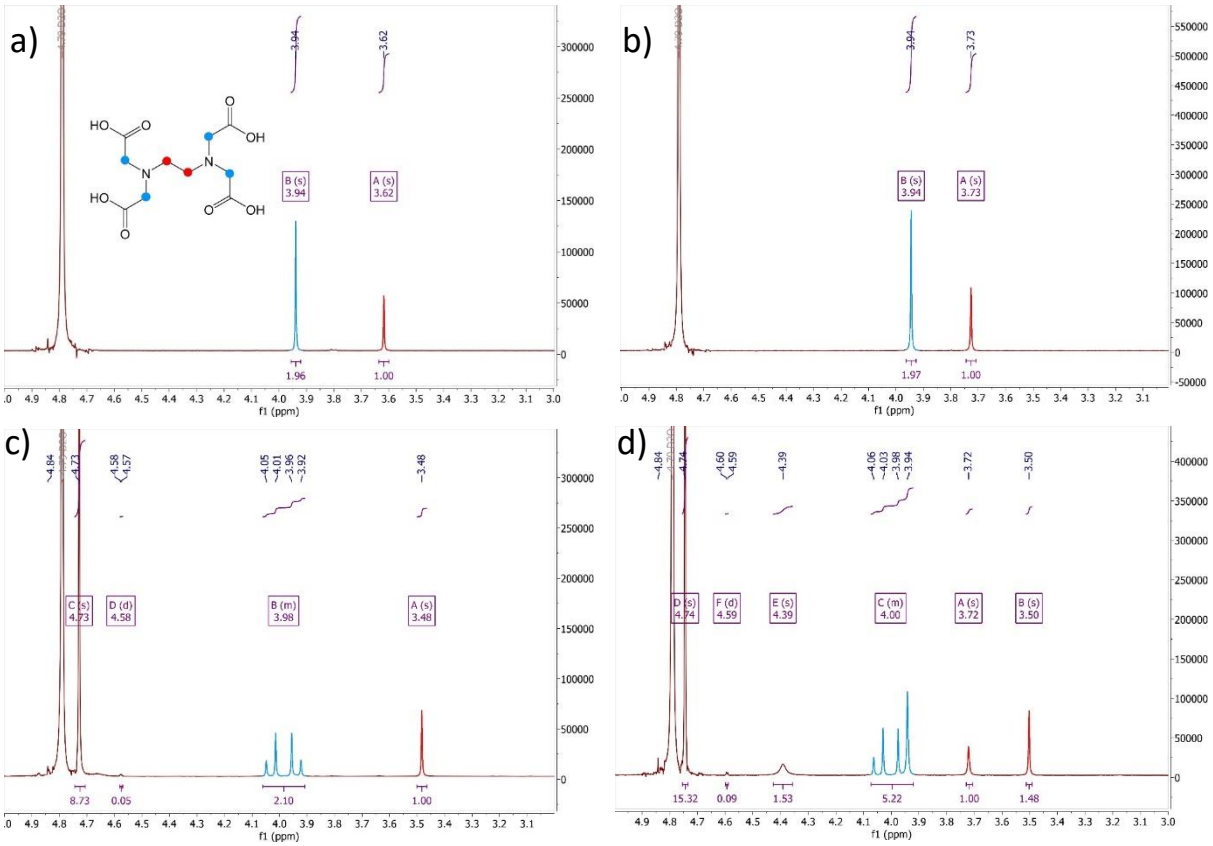

Figure 4.11: *^{1}H NMR spectra of a) EDTA, b) EDTA and STS, c) EDTA and PAT, and d) EDTA, PAT and STS solutions in D_2O, at half the concentrations used in hydrothermal synthesis; A diagram of EDTA and the relevant hydrogen groups are shown in spectrum a), with the corresponding peaks coloured in each spectrum.*

Upon addition of STS, one of the EDTA signals shifted slightly. The core -CH_2 signal at 3.62 ppm moved downfield to 3.73 ppm, which may have indicated some interaction between EDTA and STS, or it may have simply been due to the pH change in the NMR solution[19].

Once PAT was introduced, a similar but opposite shift was seen in the core -CH_2 signal at 3.62 ppm moving to 3.48 ppm, which could again have been explained by the effect of pH, as STS is basic, while PAT is acidic. More interestingly, the arm -CH_2 signal at 3.94 ppm split into what appeared to be quartet signal. However, the ratios between the peaks were not 1:3:3:1 as would be expected from a quartet, but were instead closer to 1:2.15:2.15:1. This was what is known as an A:B quartet, which is characteristic of EDTA chelation[3]. Each -CH_2-COOH arm ends up in a slightly different chemical environment, leading to a splitting of the -CH_2 singlet

into four separate signals. The environments corresponding to the two central peaks are slightly more common states for the arms to be in than the environments corresponding to the outer peaks, leading to a quartet-like appearance. The PAT peak at 4.73 ppm was also observed, as was the very weak doublet at 4.58 ppm, seen in the mixture of PAT and STS. Therefore, the weak doublet was likely from PAT, or a decomposition product of PAT. However, the broad peak at 4.37 ppm was not present, indicating that this peak was instead due to an interaction between STS and PAT.

For the mixture of STS, PAT and EDTA, a very similar spectrum to the EDTA and PAT spectrum with slightly different shifts was expected, since in the PAT and EDTA sample, only the A-B quartet was observed (and not an additional peak which would correspond to unbound EDTA), indicating that all of the present EDTA binds to PAT. However, the spectra instead were overlapped, with the core 3.62 ppm peak becoming two signals at 3.72 ppm (corresponding to the STS interaction) and 3.50 (corresponding to PAT interaction). Similarly, the peak observed at 3.94 ppm in the EDTA + STS solution overlapped the A-B quartet of the EDTA + PAT solution. The broad peak at 4.39 ppm, observed in the mixture of PAT and STS at 4.37 ppm also reappeared, further suggesting that this was due to an interaction between STS and PAT.

To summarise, PAT and STS interacted in some way to cause a hydrogen exchange. What this exchange entails is currently unknown, though it indicated that the two precursors were interacting even in ambient conditions. EDTA also interacted with STS in some way, STS shifting EDTA's core -CH_2 signal, and EDTA also interacted with PAT by binding to it (or its decomposition products), indicated by the formation of an A-B quartet out of the arm -CH_2 signal. When all three were mixed, a mixture of all of the above effects was seen, indicating that the binding of EDTA to PAT was inhibited by the presence of STS, which in turn says that STS must have been interacting with EDTA in a way more substantial than simply altering the pH of the solution.

4.3.2. Solution-Based Aggregation Test

One of the proposed mechanisms by which EDTA worked was by reducing aggregates of Sb_2E_3 in solution by coordinating to Sb[7]. To test this theory, solutions of 1) PAT and STS in water and 2) PAT, STS and EDTA in water were mixed in the same concentrations as were used for

hydrothermal synthesis. The solutions were then left in ambient conditions over the course of a few days and observed during that time. Experimental details may be found in *Section 3.2*. The results of the test for solutions 1 and 2 are shown in *Figure 4.12*. According to the proposed literature mechanisms, the solution with PAT and STS was expected to form an aggregate of Sb_2S_3, while the EDTA solution would remain clear. In fact, the opposite occurred. Over the course of a day, the standard solution had remained clear, while the EDTA solution had precipitated a red powder. This powder was presumed to be Sb_2S_3, however this needed to be confirmed in order to fully understand the mechanisms at work.

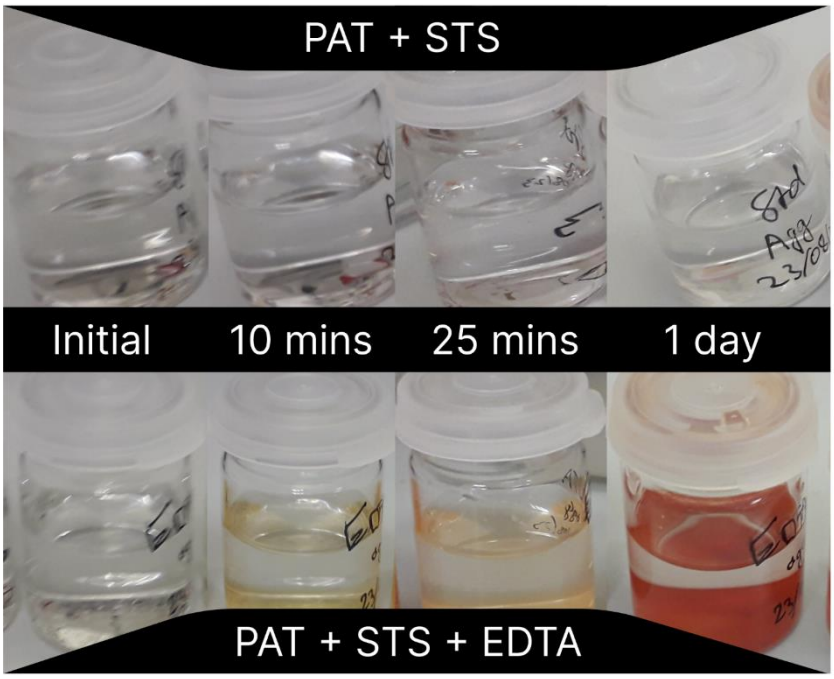

Figure 4.12: *Solution-based aggregation test for solutions 1) PAT and STS in water, and 2) PAT, STS and EDTA in water after mixing, and then after 10 minutes, 25 minutes, and one day; Vials were left sealed in ambient conditions.*

In order to identify the resultant powder (RP), powder X-ray diffraction (P-XRD; *Section 3.3.1*) was used. The P-XRD results of the RP are shown in *Figure 4.13.a*. The diffraction pattern was quite unusual, with very few peaks. The few peaks that were present corresponded to specific crystalline orientations of STS pentahydrate, the largest being the (040) direction[12, 20]. This suggested that the way the powder had been prepared (dried out from drops of the solution) had allowed unreacted precursors to also be crystallised out as residue. To remedy this, the powder was washed three times in deionised (DI) water, and the P-XRD spectrum was

remeasured (shown in *Figure 4.13.b*). This time, no clear peaks were seen, despite the powder looking visibly identical. Thus, the RP was an amorphous substance.

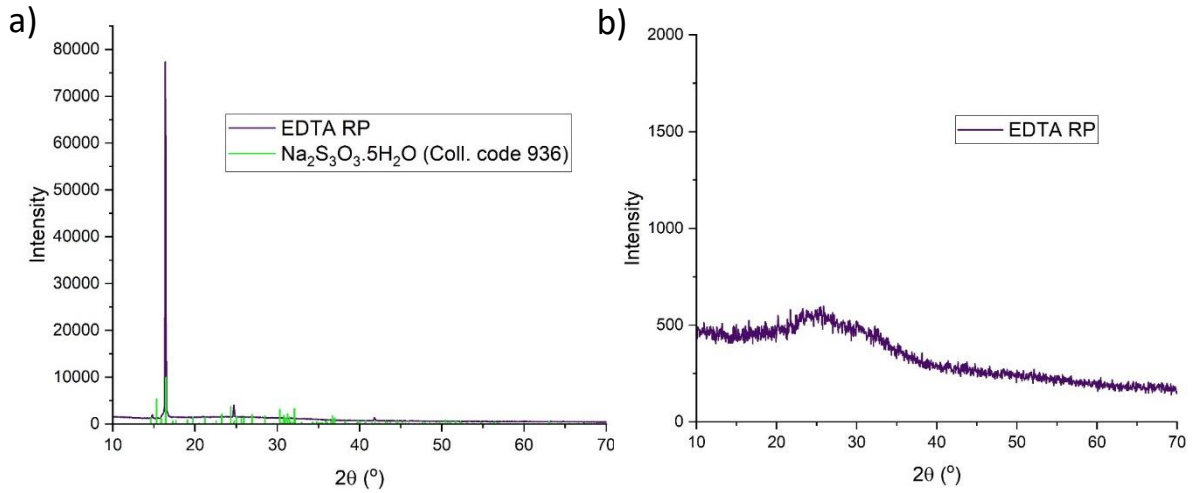

Figure 4.13: *P-XRD of a) unwashed RP of EDTA aggregation test, with STS pentahydrate (ICSD collection code 936) overlaid[12, 20] and b) RP of EDTA aggregation test after washing in DI water three times.*

To attain some further understanding of what the powder consisted of, X-ray fluorescence (XRF; *Section 3.3.6*) was used. Unfortunately, it was a very new and untested setup at the time, so the precise ratios of elements could not be fully trusted as it was not fully calibrated. However, it allowed for the confirmation that both sulfur and antimony were the primary elements present (the ratio measured was 11.6 : 1, corresponding with weight % 75.3, 24.7). The technique could not detect organic elements (C, N, O) due to reasons outlined in *Section 3.3.6*, so their presence could not be ruled out.

By combining this finding with the P-XRD results, it seemed very likely that the formed powder was Sb_2S_3. Further investigation into the nature of the powder and the reasons behind its formation are discussed in *Chapter 6*. For the time being, it was reasonable to assume that if EDTA was an effective additive, this red RP formation in the aggregation test may have corresponded to its effectiveness as an additive in this system. To that end, other additives were screened using this test and observing the results, which are in *Chapter 5*.

4.4. Conclusions

EDTA was determined to be an effective additive in Sb_2S_3/TiO_2 solar cells, as it had been previously in $Sb_2(S, Se)_3$/CdS cells. It provided similar film crystallinity and orientation benefits, while also providing a hitherto unseen effect of Sb_2O_3 suppression. NMR spectroscopy showed that EDTA interacted with both of the precursors PAT and STS in some way, with distinct signs of EDTA complexing in the presence of PAT. These findings suggest that the originally proposed mechanism of Sb complexation may be correct, but it is not the whole understanding of what EDTA is doing in the hydrothermal solution. Furthermore, in the solution aggregation test, EDTA was observed to actually increase the aggregation of what appeared to be amorphous Sb_2S_3, rather than suppress it, as originally proposed. These findings form the basis of the additive screening process explored in *Chapter 5*, and the deeper mechanistic understanding of the role of EDTA and similar additives detailed in *Chapter 6*.

4.5. References

1. Yang, D.; Yang, R.; Wang, K.; Wu, C.; Zhu, X.; Feng, J.; Ren, X.; Fang, G.; Priya, S.; Liu, S., High Efficiency Planar-Type Perovskite Solar Cells with Negligible Hysteresis Using Edta-Complexed SnO_2. *Nature Communications* **2018,** *9* (1), 3239.

2. Resgalla, C.; Poleza, F.; Souza, R. C.; Máximo, M. V.; Radetski, C. M., Evaluation of Effectiveness of EDTA and Sodium Thiosulfate in Removing Metal Toxicity toward Sea Urchin Embryo-Larval Applying the Tie. *Chemosphere* **2012,** *89* (1), 102-107.

3. Hafer, E.; Holzgrabe, U.; Kraus, K.; Adams, K.; Hook, J. M.; Diehl, B., Qualitative and Quantitative 1H NMR Spectroscopy for Determination of Divalent Metal Cation Concentration in Model Salt Solutions, Food Supplements, and Pharmaceutical Products by Using EDTA as Chelating Agent. *Magnetic Resonance in Chemistry* **2020,** *58* (7), 653-665.

4. Mathuthu, E.; Janse van Rensburg, A.; Du Plessis, D.; Mason, S., EDTA as a Chelating Agent in Quantitative (1)H-NMR of Biologically Important Ions. *Biochem Cell Biol* **2021,** *99* (4), 465-475.

5. Lokhande, C. D., Chemical Deposition of Metal Chalcogenide Thin Films. *Materials Chemistry and Physics* **1991,** *27* (1), 1-43.

6. Chen, G.-Y.; Zhang, W.-X.; Xu, A.-W., Synthesis and Characterization of Single-Crystal Sb_2S_3 Nanotubes Via an Edta-Assisted Hydrothermal Route. *Materials Chemistry and Physics* **2010,** *123* (1), 236-240.

7. Wang, X.; Tang, R.; Jiang, C.; Lian, W.; Ju, H.; Jiang, G.; Li, Z.; Zhu, C.; Chen, T., Manipulating the Electrical Properties of $Sb_2(S,Se)_3$ Film for High-Efficiency Solar Cell. *Advanced Energy Materials* **2020,** *10* (40), 2002341.

8. Zhang, Y.; Li, S. a.; Tang, R.; Wang, X.; Chen, C.; Lian, W.; Zhu, C.; Chen, T., Phosphotungstic Acid Regulated Chemical Bath Deposition of Sb_2S_3 for High-Efficiency Planar Heterojunction Solar Cell. *Energy Technology* **2018,** *6* (11), 2126-2131.

9. Wang, S.; Zhao, Y.; Che, B.; Li, C.; Chen, X.; Tang, R.; Gong, J.; Wang, X.; Chen, G.; Chen, T.; Li, J.; Xiao, X., A Novel Multi-Sulfur Source Collaborative Chemical Bath Deposition Technology Enables 8%-Efficiency Sb_2S_3 Planar Solar Cells. *Advanced Materials* **2022,** *34* (41), 2206242.

10. Zhang, L.; Xiao, P.; Che, B.; Yang, J.; Cai, Z.; Wang, H.; Gao, J.; Liang, W.; Wu, C.; Chen, T., Mechanistic Study of the Transition from Antimony Oxide to Antimony Sulfide in the Hydrothermal Process to Obtain Highly Efficient Solar Cells. *ChemSusChem* **2023,** *16* (7), e202202049.

11. Choi, Y. C.; Lee, D. U.; Noh, J. H.; Kim, E. K.; Seok, S. I., Highly Improved Sb_2S_3 Sensitized-Inorganic–Organic Heterojunction Solar Cells and Quantification of Traps by Deep-Level Transient Spectroscopy. *Advanced Functional Materials* **2014,** *24* (23), 3587-3592.

12. Nist Inorganic Crystal Structure Database. NIST Standard Reference Database Number 3, National Institute of Standards and Technology, Gaithersburg MD, 20899.

13. Šćavničar, S., The Crystal Structure of Stibnite. A Redetermination of Atomic Positions. **1960,** *114* (1-6), 85-97.

14. Svensson, C., Refinement of the Crystal Structure of Cubic Antimony Trioxide, Sb_2O_3. *Acta Crystallographica Section B* **1975,** *31* (8), 2016-2018.

15. Huang, Y.; Tang, R.; Xiao, P.; Che, B.; Wang, Y.; Gao, H.; Wang, G.; Zhu, C.; Chen, T., Efficient in Situ Sulfuration Process in Hydrothermally Deposited Sb_2S_3 Absorber Layers. *ACS Applied Materials & Interfaces* **2022,** *14* (49), 54822-54829.

16. Sui, Z.; Hu, S.; Chen, H.; Gao, C.; Su, H.; Rahman, A.; Dai, R.; Wang, Z.; Zheng, X.; Zhang, Z., Laser Effects on Phase Transition for Cubic Sb_2O_3 Microcrystals under High Pressure. *Journal of Materials Chemistry C* **2017,** *5* (22), 5451-5457.

17. Diliegros Godines, C.; Santos, J.; Mathews, N.; Pal, M., Effect of Ag Doping on Structural, Optical and Electrical Properties of Antimony Sulfide Thin Films. *Journal of Materials Science* **2018,** *53*.

18. Charisiadis, P.; Kontogianni, V. G.; Tsiafoulis, C. G.; Tzakos, A. G.; Siskos, M.; Gerothanassis, I. P., 1H-NMR as a Structural and Analytical Tool of Intra- and Intermolecular Hydrogen Bonds of Phenol-Containing Natural Products and Model Compounds. *Molecules* **2014,** *19* (9), 13643-13682.

19. Kukic, P.; O'Meara, F.; Hewage, C.; Erik Nielsen, J., Coupled Effect of Salt and pH on Proteins Probed with Nmr Spectroscopy. *Chemical Physics Letters* **2013,** *579*, 114-121.

20. *Acta Crystallographica, Section B: Structural Crystallography and Crystal Chemistry*. 1977; Vol. 33.

5. Investigation of Alternative Additives for Sb_2E_3 Solar Cells

5.1. Introduction

Following on from the study of ethylenediaminetetraacetic acid (EDTA) as an additive in Sb_2S_3/TiO_2 solar cells covered in *Chapter 4*, this chapter explores alternative additives with the aims of a) the determination of functional aspects of EDTA, allowing for design rules to be established, b) the finding of additives which rival and/or exceed the performance of EDTA and c) the correlation of design rules with the findings of *Chapter 4*, to find and prove the underlying mechanisms by which EDTA and similar molecules improve efficiency in Sb_2E_3 solar cells.

Many molecules exist which could potentially be used as additives. Therefore, the solution-based aggregation test from *Chapter 4* was used as a screening process to determine some preliminary information about the additives before a selection were used to fabricate full solar cells. The list of the additives tested, their structure and their similarities to EDTA are shown in *Table 5.1*.

Table 5.1: *Names, similarities to EDTA and chemical structures for all additives tested in solution-based aggregation test.*

Additive Name	Short Name	Similarities to EDTA	Chemical Structure
Nitrilotriacetic acid	NTA	Similar structure to EDTA, without -CH_2-CH_2- bridge, and with an extra arm	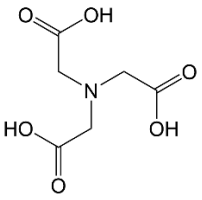
Ethylenediaminetetraacetic acid	EDTA	N/A	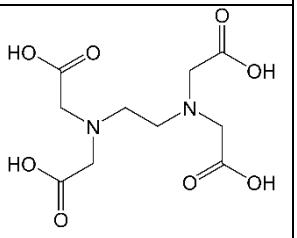
Pentetic acid	PA	Similar to EDTA, with central bridge expanded to add another N and arm	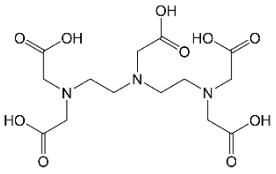
Triethylenetetramine-N,N,N',N'',N''',N'''-hexaacetic acid	TETAH	Similar to PA (above) with central bridge expanded once again to add another N and arm	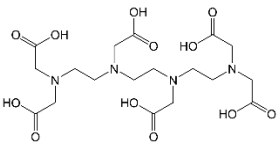
3,4,9,10-Perylenetetracarboxylic dianhydride	34910-P	C=O and C-O groups in close proximity	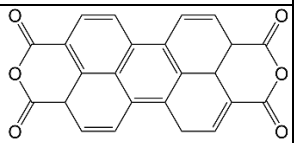
Creatinine	Creat	O and N available for coordination	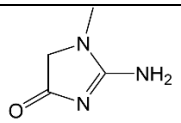
Triethanolamine	TEA	Central N group with ‘arms’ ending in OH instead of COOH	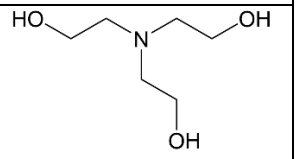
4,5-dimethyl-2-nitroaniline	45-d-2-n	O and N available for coordination	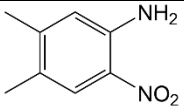

4-nitrophenol	4-n	O and N available for coordination	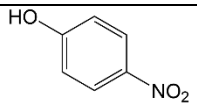
Pentafluoronitrobenzene	PFNB	O and N available for coordination	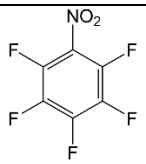
1,1',1'',1'''-(ethane-1,2-diylbis(azanetriyl))tetrakis(propan-2ol)	1111E	Similar structure to EDTA, but with $(CH_2)COOH$ arm groups replaced with $CH(CH_3)OH$	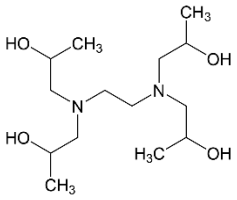
4,4'-dithiobutyric acid	44D	COOH groups with potential to chelate	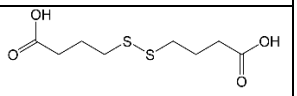
Citric acid	CA	COOH groups in proximity	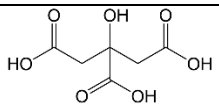
Diethylenetriaminepentakis(methylphosphonic acid) solution	DETAP	Similar structure to PA (above), with extra N group added to middle of chain, and COOH groups replaced with PO_3H_2	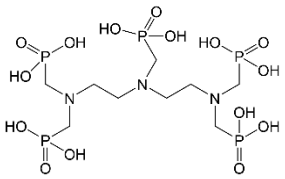
Ethylenediamine	ED	Backbone of EDTA without arms	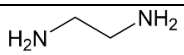
Diglycolic acid	DGA	COOH groups with potential to chelate	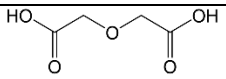
Sebacic acid	SBA	COOH groups with potential to chelate	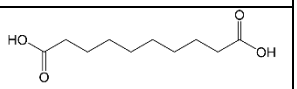
12-Aminododecanoic acid	12-ADA	COOH group and NH_2 group with potential to chelate	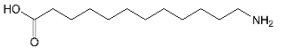
L-(+)-Tartaric acid	LTA	COOH groups with potential to chelate	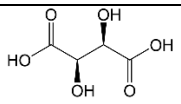

N,N,N',N',N'-Pentamethyldiethyldiethylenetriamine	PMDTA	N groups with potential to chelate	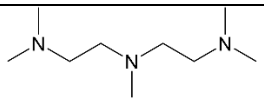
Nitrilotris(methylenephosphonic) acid	NTMP	Equivalent of NTA (above) with COOH replaced with PO_3H_2	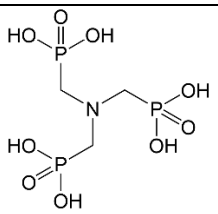

5.2. Screening and Testing of Additives

The aggregation test from *Chapter 4* (experimental details in *Section 3.2*) was utilised as a screening process. This was done by repeating the test but replacing EDTA with an equimolar amount of the additive to be tested. Observation over the course of a day showed whether the additive formed a similar aggregate to what was seen for EDTA, and whether or not other side reactions were occurring. The results of this test are given in *Section 5.2.1*. Additionally, some information about reaction speed could be attained by observing the initial change from clear and colourless to coloured, if such a change occurred.

The powder and liquids left after the solution had reacted were separated, as detailed in *Section 3.2*, and the powders recovered will henceforth be referred to as the resultant powder (RP). The RPs were measured using powder X-ray diffraction (P-XRD; *Section 3.3.1*), and a selection was further examined using scanning electron microscopy (SEM; *Section 3.3.3*) and SEM energy-dispersive X-ray spectroscopy (EDS; *Section 3.3.3*).

After an initial screening, Sb_2S_3 films and solar cells were prepared according to the methods described in *Section 3.1* with a selection of promising and/or interesting additives. The films were measured with P-XRD, with a small selection being measured using atomic force microscopy (AFM; *Section 3.3.2*), SEM and SEM-EDS. The results are given in *Section 5.2.2*.

Finally, the solar performance of the fabricated films was measured using current density-voltage (J-V; *Section 3.4.1*) curves and external quantum efficiency (EQE; *Section 3.4.2*) measurements. These results are given in *Section 5.2.3*.

5.2.1. Aggregation Screening Test

Each additive was added to a solution of potassium antimony tartrate (PAT) and sodium thiosulfate (STS) in water, in the same concentrations as used in hydrothermal synthesis. These solutions were left for a day in ambient conditions. Images of the vials at the start and after 1 day are shown in *Figure 5.1*.

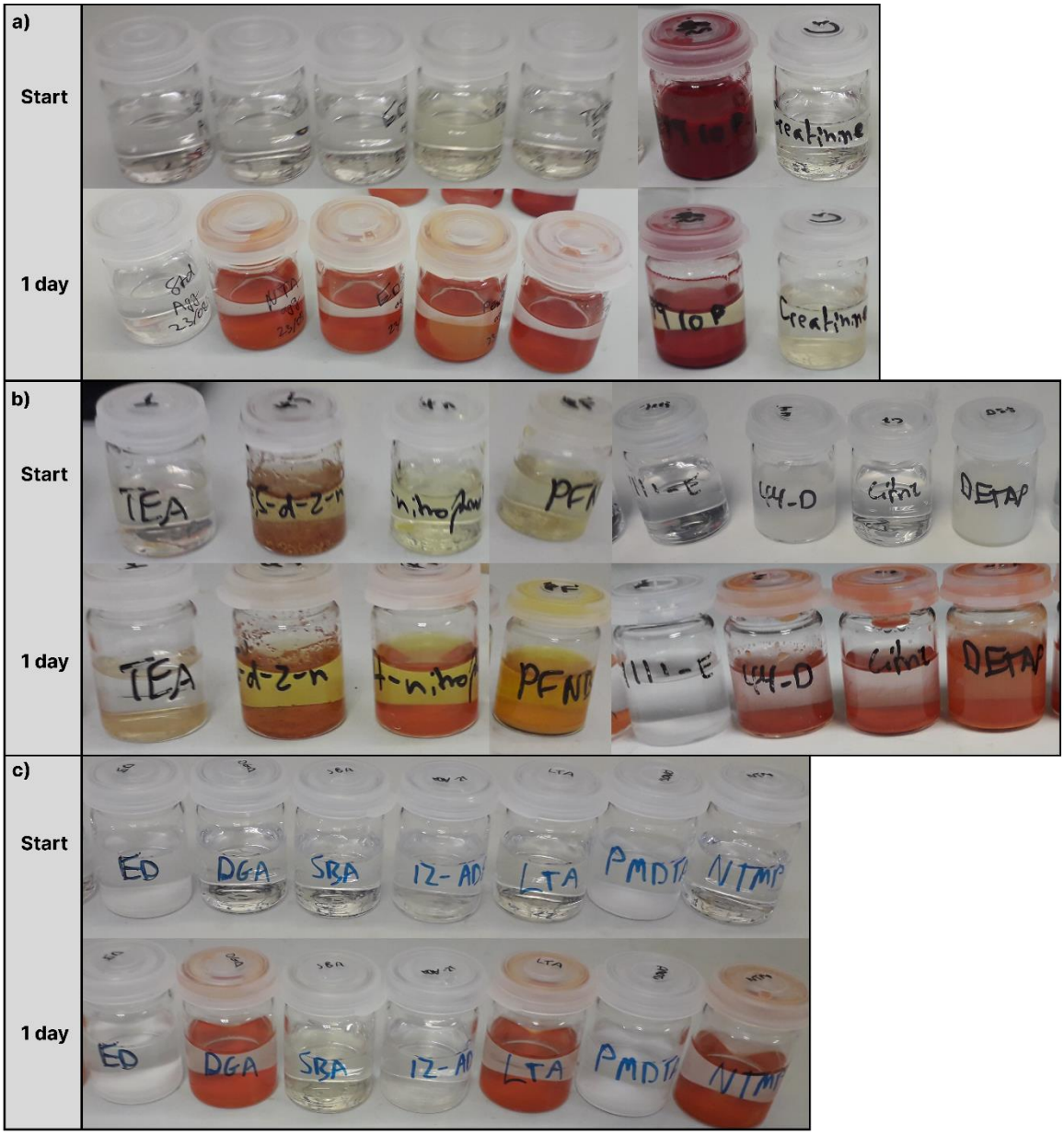

Figure 5.1: *Photographs of aggregation screening test vials for each additive, immediately after mixing and after 1 day in ambient conditions; additives (from left to right): a) no additive (standard), NTA, EDTA, PA, TETAH, 34910-P, Creat; b) TEA, 45-d-2-n, 4-n, PFNB, 1111E, 44-D, CA, DETAP; c) ED, DGA, SBA, 12-ADA, LTA, PMDTA, NTMP.*

A variety of results were seen for the various additives, with many forming red precipitates similarly to EDTA, some forming white precipitates, and others forming precipitates of different colours. The additives which formed red powders are NTA, EDTA, PA, TETAH, 44-D, CA, DETAP, DGA, LTA, NTMP and 4-n. SBA also formed a similar red powder after another three days.

A few additives showed signs of little to no reaction, with 45-d-2-n initially forming a pale-yellow solution with little change over a day. 34910-P was a red powder, but it was red to begin with, with no obvious colour change over the course of a day. PMDTA started as a white powder and had no change after a day.

PFNB had a drastic change from clear, pale yellow to a deep yellow colour. This indicated a distinct reaction, but likely the formation of elemental sulfur rather than Sb_2S_3.

The samples which did not change (34910-P, 45-d-2-n, PMDTA) and sample which had an obvious side reaction (PFNB) were not included for testing in full cells, as they showed no effect, or an unknown effect on the solution. A selection of red and white RP forming additives were chosen to make solar cells from. TEA, 1111E and ED were chosen for white RP forming additives, due to their similarity to EDTA structurally. NTA, PA and TETAH were chosen for red RP additives, due to being in the 'EDTA family' of structures. DGA, LTA and NTMP were also chosen as additional red RP additives with a range of similar structural moieties to EDTA. DETAP would have been chosen due to its similarity to the EDTA structure, however it was in a solution with HCl, which may have damaged the film.

Before fabricating films and cells, the RPs of these additives were isolated according to the method in *Section 3.2* and measured in P-XRD. The P-XRD results of the red and white RPs are shown in *Figure 5.2*.

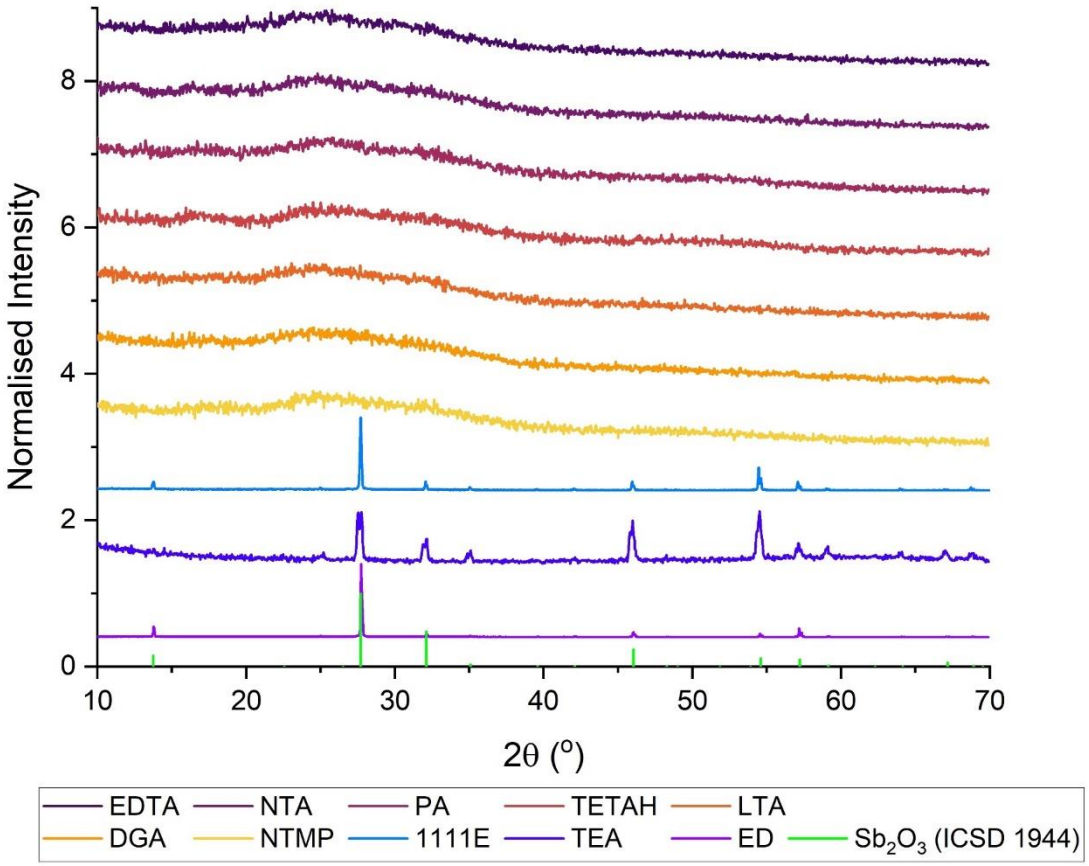

Figure 5.2: *P-XRD of a) red RPs of additives EDTA, NTA, PA, TETAH, LTA, DGA, NTMP and b) white RPs of additives 1111E, TEA, ED showing ICSD standard for Sb_2O_3 (collection code 1944[1])*

The red RP patterns presented no distinct peaks (as with the EDTA RP in *Chapter 4*), indicating an amorphous nature. This suggested that the powders were likely the same as the EDTA RP, which was thought to be amorphous Sb_2S_3. Therefore, the mechanism by which this RP was forming was likely common between all of the additives which formed it. The white RP patterns matched the literature pattern for cubic Sb_2O_3, meaning that these additives were promoting the formation of Sb_2O_3, contrasting the Sb_2O_3 suppression mechanism seen for EDTA in *Chapter 4*[1]. The three additives all forming the same RP suggested another common mechanism for its formation. These common mechanisms are explored in more depth in *Chapter 6*.

5.2.2. Film Quality of Chosen Additives

Sb_2S_3 films were fabricated according to the method described in *Section 3.1.2* using the chosen additives from *Table 5.1* (EDTA, NTA, PA, TETAH, LTA, DGA, NTMP for red RP forming,

and 1111E, TEA and ED for white RP forming). The crystallinity and Sb_2O_3 content of the films was investigated using P-XRD and compared to the standard (no additive). The results are shown in *Figure 5.3*.

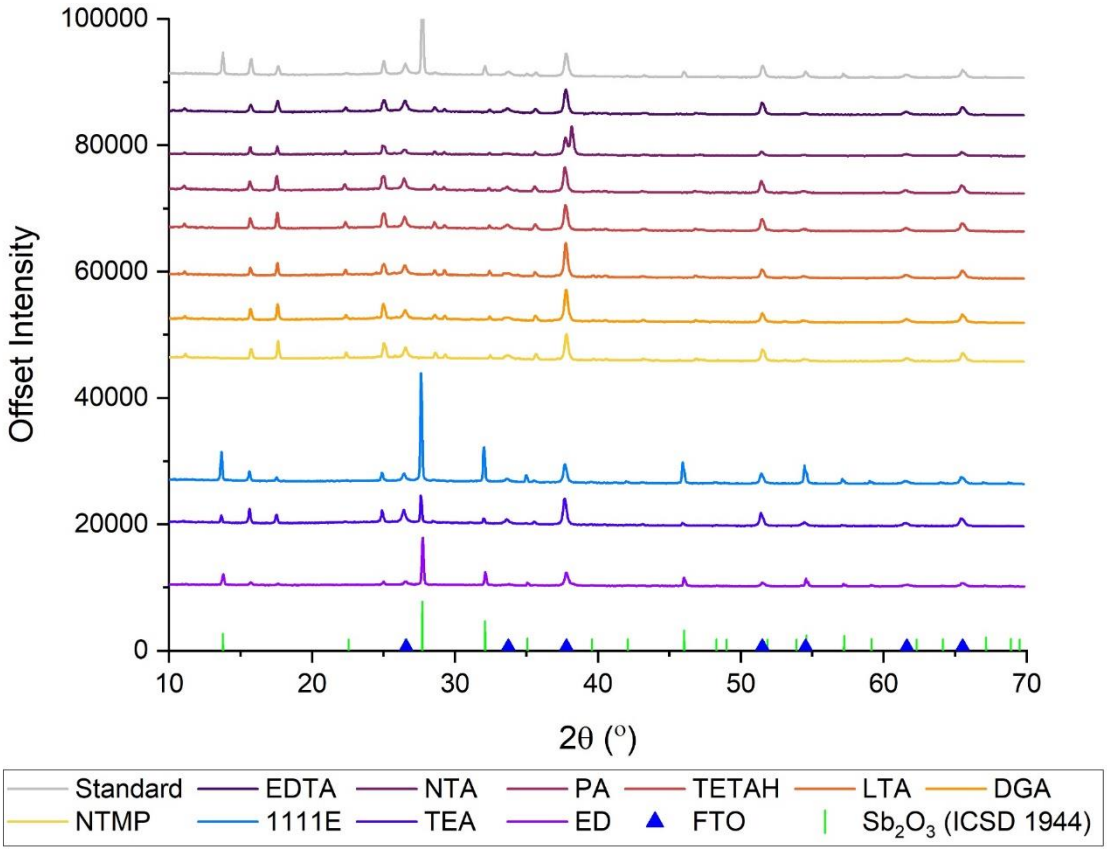

Figure 5.3: *P-XRD patterns of Sb_2S_3 films fabricated using no additive (standard) and the additives EDTA, NTA, PA, TETAH, LTA, DGA, NTMP, 1111E, TEA and ED. Intensities have been normalised for comparison.*

The films fabricated with the white RP additives 1111E, TEA and ED each had Sb_2O_3 also incorporated into the film. This was logical, seeing as they were observed to form Sb_2O_3 (the white RP) in solution during the screening process. It rationally follows that this Sb_2O_3 would then incorporate during the film deposition. In contrast, all of the red RP forming additives had no signs of Sb_2O_3 in the film, indicating that the common mechanism which caused the red RP formation also had an effect of suppressing Sb_2O_3.

The standard (no additive) film gave a hk1/hk0 texture coefficient ratio ($TC_{hk1/hk0}$; *Section 3.3.1*) of 0.837. A higher value of $TC_{hk1/hk0}$ means that the film was overall orientated in more of the desired hk1 (perpendicular to substrate) direction, while a lower value means it was

orientated in more of the undesired hk0 (parallel to substrate) direction in the film. All of the red RP forming additives increased the intensity of the (221) and (211) peaks similarly to EDTA. PA and TETAH yielded an overall value of $TC_{hk1/hk0}$ which was lower than the value of EDTA at 0.983, with values of 0.890 and 0.876, respectively. NTA was only slightly worse than EDTA in orientation, with a $TC_{hk1/hk0}$ of 0.965, and NTMP was slightly worse again at 0.945. DGA and LTA, on the other hand, had higher $TC_{hk1/hk0}$, with 1.01 and 1.10, respectively. Overall, it appeared that DGA and LTA yielded the most favourable directionality for solar cells, though all of the red RP additives improved the (221) and (211) reflections over the standard.

Atomic force microscopy (AFM; *Section 3.3.2*) was used to look at the surface of a selection of red RP additive films, to determine their effects on grain size and film roughness. PA, TETAH, LTA and NTMP were scanned, and the results are shown in *Figure 5.4* alongside the previous standard and EDTA film results.

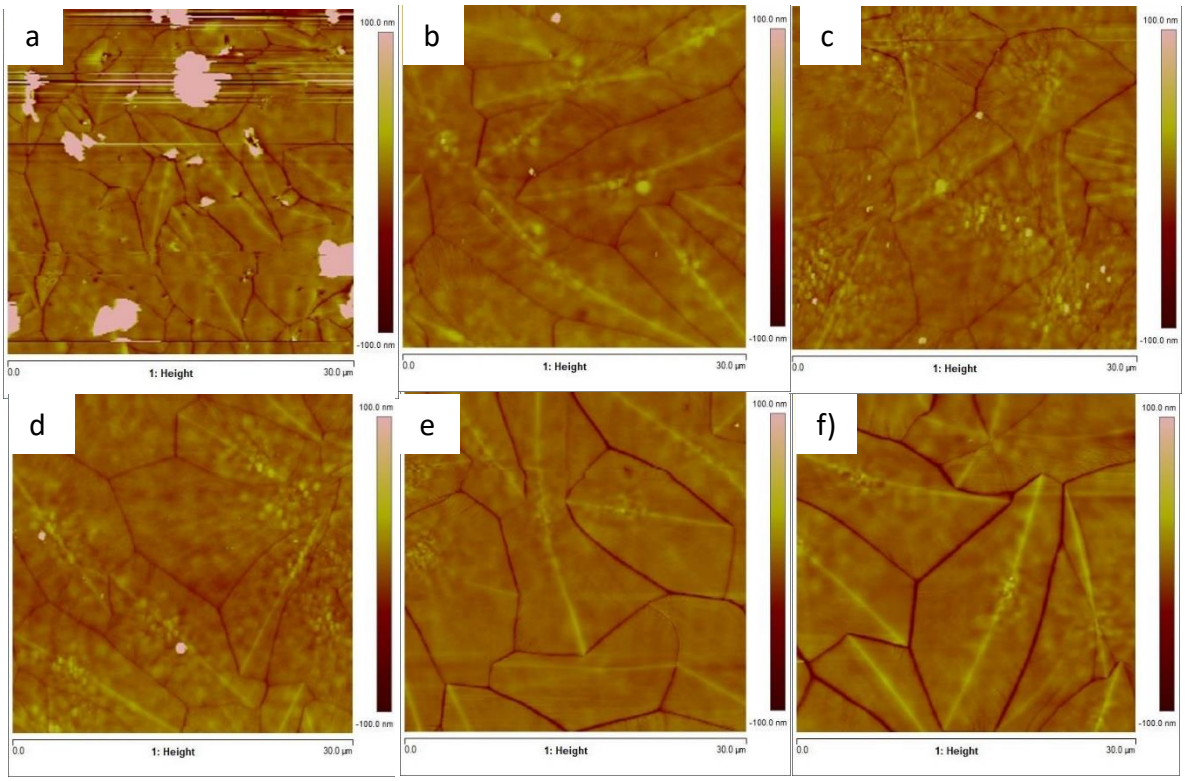

***Figure 5.4**: AFM scans of the surface of Sb_2S_3 films fabricated using a) no additive (standard) and additives b) EDTA, c) PA, d) TETAH, e) DGA and f) NTMP; The area measured for each was 30x30 µm, with a depth range of -100 to 100 nm displayed.*

The film roughness (R_q) across the entirety of each image shown was 136 nm for the standard, 8.33 nm for EDTA, 7.57 nm for PA, 9.09 nm for TETAH, 6.48 nm for DGA, and 8.74 nm for NTMP.

Therefore, each of these red RP forming additives had a similar roughness, which was much lower than the standard film. However, by isolating a 5x5 µm area of the standard film without the large Sb_2O_3 formations, an R_q value of ~6 nm was attained, indicating that the Sb_2S_3 film underlying the Sb_2O_3 was actually quite smooth, and of similar magnitude to the red RP films.

Grain size and shape, on the other hand, changed significantly between the samples. PA and TETAH appeared to have more minor surface roughness, while DGA and NTMP had much larger 'valleys' and 'crests' between and on top of the crystal grains, respectively. EDTA fell between these two sets, with visible but less defined crests and valleys. PA and TETAH, therefore, are expected to have a lower degree of recombination, as the grains were more compact and the grain boundaries were less distinctly defined, providing less of a barrier for charges passing between grains. However, as mentioned earlier, the value of $TC_{hk1/hk0}$ was lower for PA and TETAH, meaning the crystals were orientated more parallel to the substrate. The $TC_{hk1/hk0}$ values correlated quite well with these observed differences in appearance, as it appeared the more orientated in the hk1 direction the film was, the deeper the grain boundaries were. So, while the orientation bode well for the potential performance of the more hk1-orientated DGA and LTA, the reduction of recombination at grain boundaries by a compact film would also have an impact, and a balance of these effects would likely produce the best result.

Overall, the red RP additives greatly improved the film quality, primarily through the removal of Sb_2O_3 which was an effect common to all of them. In contrast, the white RP additives incorporated the Sb_2O_3 powder which they formed in solution into the films, which will likely negatively affect solar performance. Competing effects of orientation of the crystals in the hk1 direction and the compactness of crystalline grains was seen, indicating that perhaps growth in the hk1 direction using these additives may impact the compactness of the crystal grains.

5.2.3. Solar Performance of Chosen Additives

The performance of the chosen additives EDTA, NTA, PA, TETAH, LTA, DGA, NTMP, 1111E, TEA and ED in solar cells was assessed using current density-voltage (J-V) and external quantum efficiency (EQE) measurements. The J-V curves under light and dark conditions are shown in *Figure 5.5*.

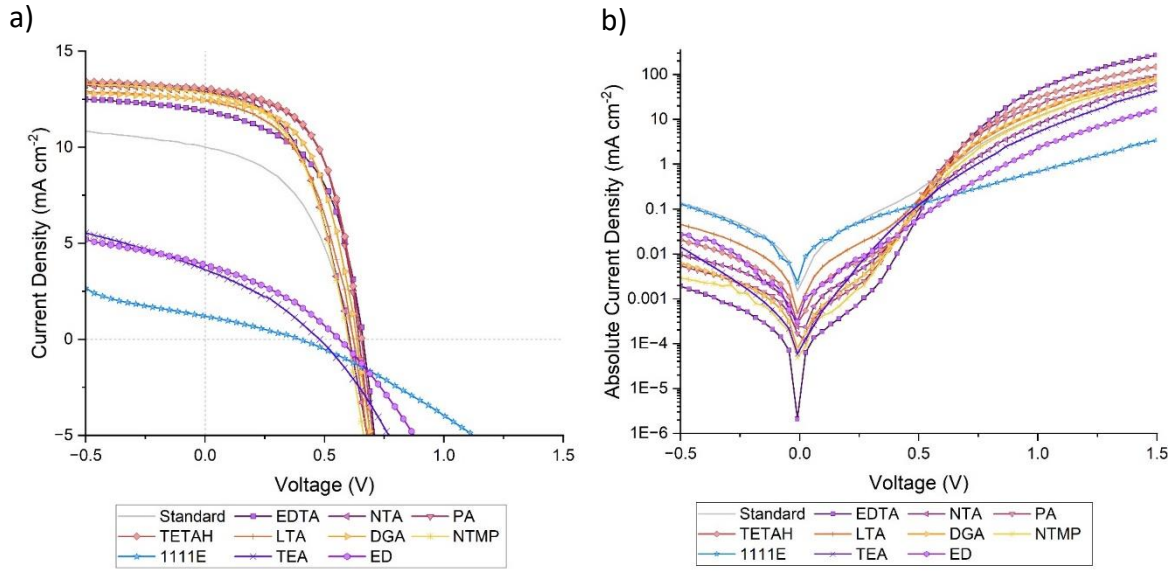

Figure 5.5: *J-V curves of champion Sb_2S_3 solar cells made with no additive (standard) and with additives EDTA, NTA, PA, TETAH, LTA, DGA, NTMP, 1111E, TEA and ED; under a) light conditions (AM1.5G, 100 mW cm^{-2}) and b) dark conditions.*

The red RP forming additives (shown in red-yellow colours) performed significantly better than the white RP forming additives (shown in blue-purple colours), and all out-performed the standard. The light curve primarily showed an increase in J_{SC} and FF for the red RP additives over the standard, and significant decreases in all of J_{SC}, V_{OC} and FF for the white RP additives compared to the standard. The dark curve did not have as well-defined differences between the samples, with only a few distinguishing features. The standard and 1111E curves had a very high leakage current, which helps to explain why their V_{OC} and FF was lower than the red RP additive cells. Additionally, the white RP additives had the lowest current density values at 1.5 V, indicating that the series resistance (R_S) was increased, explaining the lowered J_{SC} and FF.

However, for a more balanced overview, the whole set of cells should be considered. In *Figure 5.6*, the cell statistics for each additive are shown. Additionally, the champion values, and the average (±standard deviation) for each set of cells are shown in *Table 5.2*.

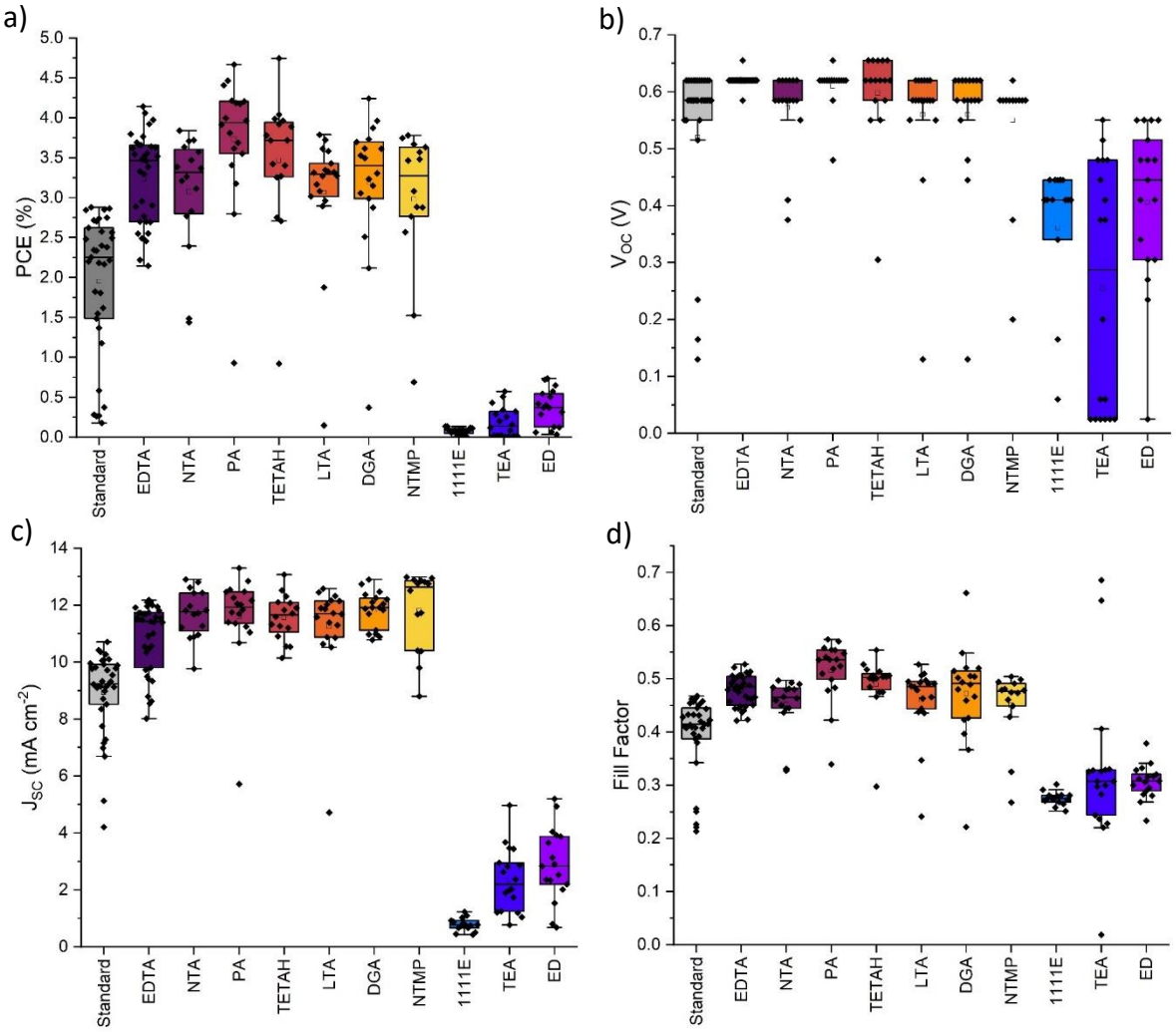

Figure 5.6: *Sb_2S_3 solar cell performance statistics a) PCE, b) V_{OC}, c) J_{SC} and d) FF for cells fabricated using no additive (standard) and additives EDTA, NTA, PA, TETAH, LTA, DGA, NTMP, 1111E, TEA and ED; For standard and EDTA, 6 cells were fabricated for each, with a cell containing 6 pixels, giving a total of 36 data points. For the additional additives, 3 cells were fabricated for each, with a cell containing 6 pixels, for a total of 18 data points. All of the cells were fabricated over the course of 10 experimental runs. Shunted pixels did not yield photovoltaic performance and so were excluded. In total, one pixel of the standard, EDTA and ED, two pixels of the NTA and TETAH, three of the 1111E and four of the NTMP pixels were fully shunted and thus excluded from the results.*

Table 5.2: *Champion and average performance metrics PCE, V_{OC}, J_{SC} and FF with standard deviations for Sb_2S_3 solar cells fabricated using no additive (standard) and additives EDTA, NTA, PA, TETAH, LTA, DGA, NTMP, 1111E, TEA and ED*

Additive	**PCE (%) champion, (average ±s.d.)**	**V_{OC} (V) champion, (average ±s.d.)**	**J_{SC} (mA cm^{-2}) champion, (average ±s.d.)**	**FF champion, (average ±s.d.)**
Standard	2.88 (1.95 ±0.9)	0.62 (0.52 ±0.2)	10.1 (8.94 ±2)	0.46 (0.39 ±0.08)
EDTA	4.14 (3.23 ±0.6)	0.66 (0.62 ±0.02)	12.1 (10.9 ±1)	0.52 (0.48 ±0.03)
NTA	3.84 (3.08 ±0.7)	0.62 (0.57 ±0.07)	12.9 (11.7 ±0.9)	0.48 (0.45 ±0.05)
PA	4.67 (3.73 ±0.8)	0.66 (0.61 ±0.04)	13.3 (11.6 ±2)	0.54 (0.52 ±0.06)
TETAH	4.75 (3.47 ±0.8)	0.66 (0.60 ±0.08)	13.1 (11.6 ±0.8)	0.55 (0.49 ±0.05)
LTA	3.79 (3.06 ±0.8)	0.62 (0.56 ±0.1)	12.5 (11.3 ±2)	0.49 (0.46 ±0.07)
DGA	4.24 (3.19 ±0.9)	0.62 (0.56 ±0.1)	12.5 (11.8 ±0.6)	0.55 (0.47 ±0.09)
NTMP	3.78 (2.98 ±0.9)	0.59 (0.55 ±0.1)	12.8 (11.8 ±1)	0.50 (0.45 ±0.07)
1111E	0.14 (0.08 ±0.04)	0.41 (0.25 ±0.2)	1.23 (2.35 ±1)	0.27 (0.28 ±0.1)
TEA	0.57 (0.19 ±0.2)	0.48 (0.36 ±0.1)	3.67 (0.78 ±0.2)	0.33 (0.32 ±0.01)
ED	0.74 (0.37 ±0.2)	0.55 (0.41 ±0.1)	3.92 (2.88 ±1)	0.34 (0.31 ±0.03)

Similar to the observations made for the champion cell curves, the improvements in performance on average for the red RP additives primarily came from an increase in J_{SC} and

FF. In fact, the J_{SC} was higher for every red RP additive than for EDTA itself. PA and TETAH end up having an average PCE higher than that of EDTA, with EDTA at 3.23 ±0.6%, PA at 3.73 ±0.8% and TETAH at 3.47 ±0.8%. The champion values are also higher for PA and TETAH than for EDTA, with DGA joining PA and TETAH above EDTA in this case. EDTA had a champion PCE of 4.14%, while PA had 4.67%, TETAH had 4.75% and DGA had 4.24%. All of the red RP additives had some ability to chelate to Sb, but PA and TETAH particularly had the highest capability, with 5 and 6 carboxylic groups, respectively. This may be some indication that this ability of an additive to chelate to Sb translates to higher performance in Sb_2S_3 solar cells.

To confirm the J-V results and see the effect of the additives on their respective Sb_2S_3 cells' ability to absorb different wavelengths of light, EQE measurements were taken. The results of these measurements are shown in *Figure 5.7*. The J_{SC} traces all agreed well with the values of J_{SC} from the J-V curves. The effects of each additive can be very clearly seen in the EQE, with the EQE of each of the red RP additives being significantly more than the standard at almost all wavelengths, and the EQE of the white RP additives being less than half of the standard at most wavelengths.

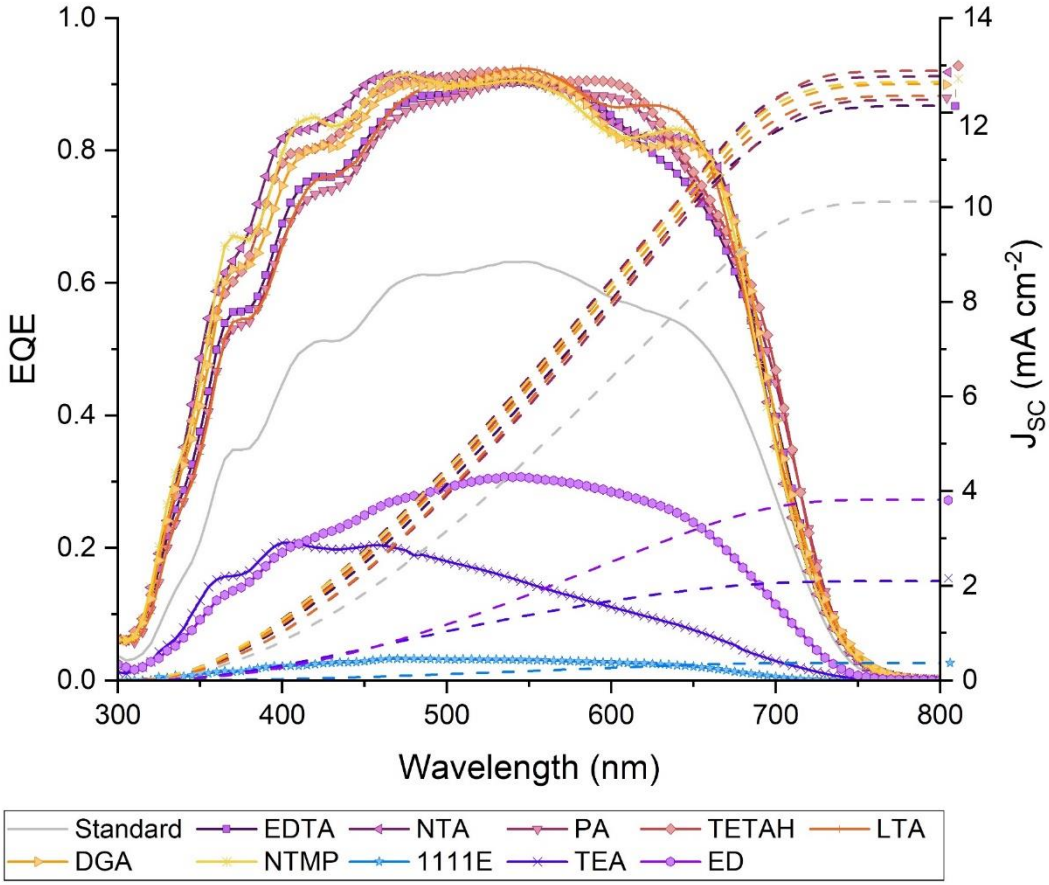

Figure 5.7: *EQE measurements for champion Sb_2S_3 solar cells made using no additive (standard) and additives EDTA, NTA, PA, TETAH, LTA, DGA, NTMP, 1111E, TEA and ED; The EQE is shown on the left axis, while the J_{SC} trace is shown on the right axis.*

As seen in *Figure 5.4*, the surface of the Sb_2S_3 layer changed to be more compact with smaller grain boundaries upon the addition of PA and TETAH, which could explain the improvement in performance from a film-quality perspective, due to a reduction in grain boundary recombination in the cell. The $TC_{hk1/hk0}$ ratio also decreased from EDTA to PA to TETAH, which would explain the slight decrease in performance from PA to TETAH. TETAH was less orientated in the favoured direction, thus the charges could not escape the cell as easily and a slight decrease in J_{SC} and V_{OC} was seen. This argument also makes sense for the observed behaviours of DGA and NTMP, with the large grains of DGA and NTMP being quite well orientated in the hk1 direction, but not very compact, leading to similar performance to the other red RP additives. Therefore, it appears that a balance between crystalline orientation and grain compactness was struck with PA, leading to a performant Sb_2S_3 solar cell.

5.3. Conclusions

Additives with various structures similar to EDTA were tested in a solution-based aggregation test and in Sb_2S_3 films and solar cells. Additives with multiple carboxylic and phosphonic acid groups formed a red resultant powder (RP), while those without (even with similar backbone structures to EDTA) formed a white RP. Additives with other groups not found on EDTA, such as -NO_2, saw additional unwanted side-reactions. The red RP was found to be amorphous using P-XRD, indicating that it was amorphous Sb_2S_3. The white RP was shown to be Sb_2O_3 using P-XRD. Films fabricated using the white RP additives all showed the incorporation of Sb_2O_3, leading to the respective solar cells all achieving average PCE values of less than 1%. This suggested that the Sb_2O_3 formed in solution had incorporated into the film during the deposition process and was causing a large amount of recombination. In contrast, the red RP films all had no signs of Sb_2O_3 being present, suggesting that the red RP formation coincided with a complete suppression of Sb_2O_3 formation. Cells made using these films yielded efficiencies above the standard, and close to, if not above, EDTA. These increases in performance primarily in terms of increased J_{SC} and FF, which were reinforced by a large increase in EQE across almost all wavelengths. The red RP films also showed that a balancing effect was at play between crystalline orientation and film compactness. PA and TETAH were very compact, but suffered from more hk0 orientation, while DGA and NTMP had very good orientation in the hk1 direction but had large grain boundaries. Overall, PA had the best balance of these effects, out-performing EDTA with an average PCE of 3.73 ±0.8% compared to 3.23 ±0.6% for EDTA (champion PCE of 4.67% compared to 4.14% for EDTA).

5.4. References

1. Svensson, C., Refinement of the Crystal Structure of Cubic Antimony Trioxide, Sb_2O_3. *Acta Crystallographica Section B* **1975,** *31* (8), 2016-2018.

6. Chemical Mechanisms of Additives in Antimony Sulfide

In *Chapters 4 and 5*, the efficacy of various additives was proven and some detail on how they might operate was indicated. In this chapter, the mechanisms by which they work will be examined in detail and chemical mechanisms for their operation will be proposed. Two main effects were of interest; the effect of the additive pH and the effect of the ability of an additive to bind to Sb. The effect of pH became of interest when it was observed that in general, acidic additives formed red RPs, while basic additives formed white RPs. The effect of an additive binding to Sb was originally proposed as a mechanism when EDTA was used previously[1], and direct evidence of the effect was observed via nuclear magnetic resonance (NMR) spectroscopy in *Chapter 4*. First, however, the composition of the red and white RPs needed to be confirmed.

6.1. Chemical and Morphological Identification of RPs

To lay a solid foundation for mechanistic analysis, the composition of the white and red resultant powders (RP) was confirmed using Raman spectroscopy (*Section 3.3.4*), and the red RP was also examined using thermogravimetric analysis (TGA; *Section 3.3.7*), scanning electron microscopy (SEM; *Section 3.3.3*) and SEM energy-dispersive X-ray spectroscopy (SEM-EDS; *Section 3.3.3*).

Raman spectroscopy was performed on each of the additives tested in *Figure 5.2*. The results are shown *Figure 6.1*. The red RP additives all display a very similar spectrum to one another, with a distinct broad peak at 290 cm^{-1}. The white RP additives also all display a similar spectrum to each other but instead of the broad peaks of the red RP, they have a few sharp peaks. The red RP additive spectrum matches very well with the literature spectrum for amorphous Sb_2S_3, and the white RP spectra match the literature spectrum for Sb_2O_3[2, 3].

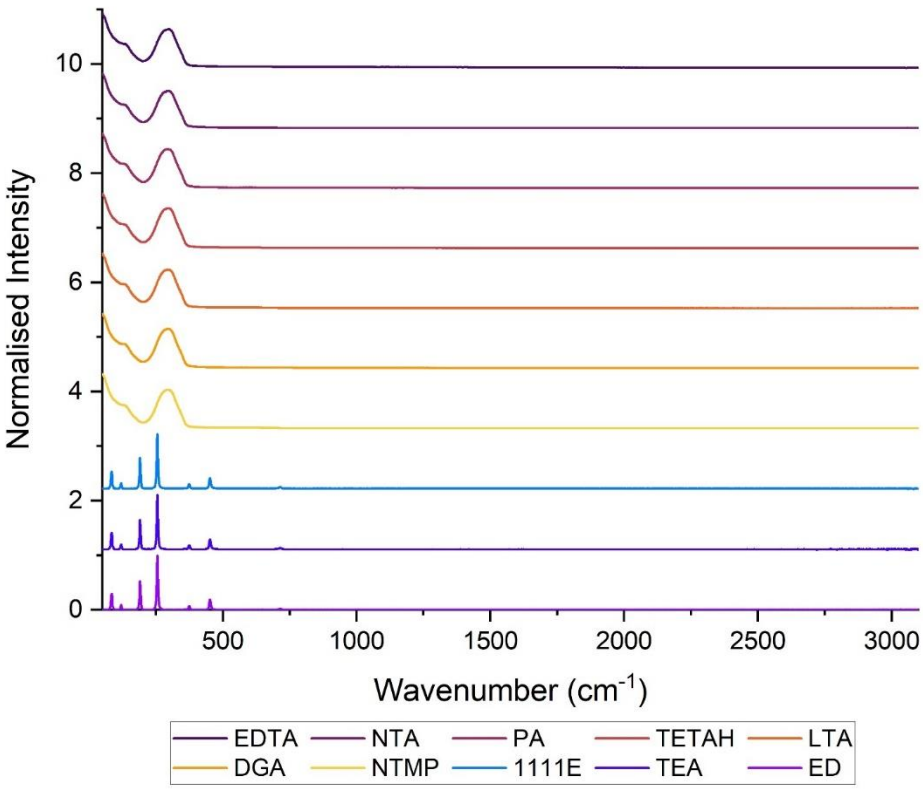

Figure 6.1: *Raman spectra of RPs of additives EDTA, NTA, PA, TETAH, LTA, DGA, NTMP, 1111E, TEA and ED; The spectra intensities have been normalised for easy comparison between them.*

SEM was used to observe the morphology of the red RPs, and SEM-EDS was used to determine the elemental composition, as some impurities may not have shown clearly in P-XRD or Raman spectroscopy. An SEM image of the EDTA RP and PA RP is shown in *Figure 6.2*.

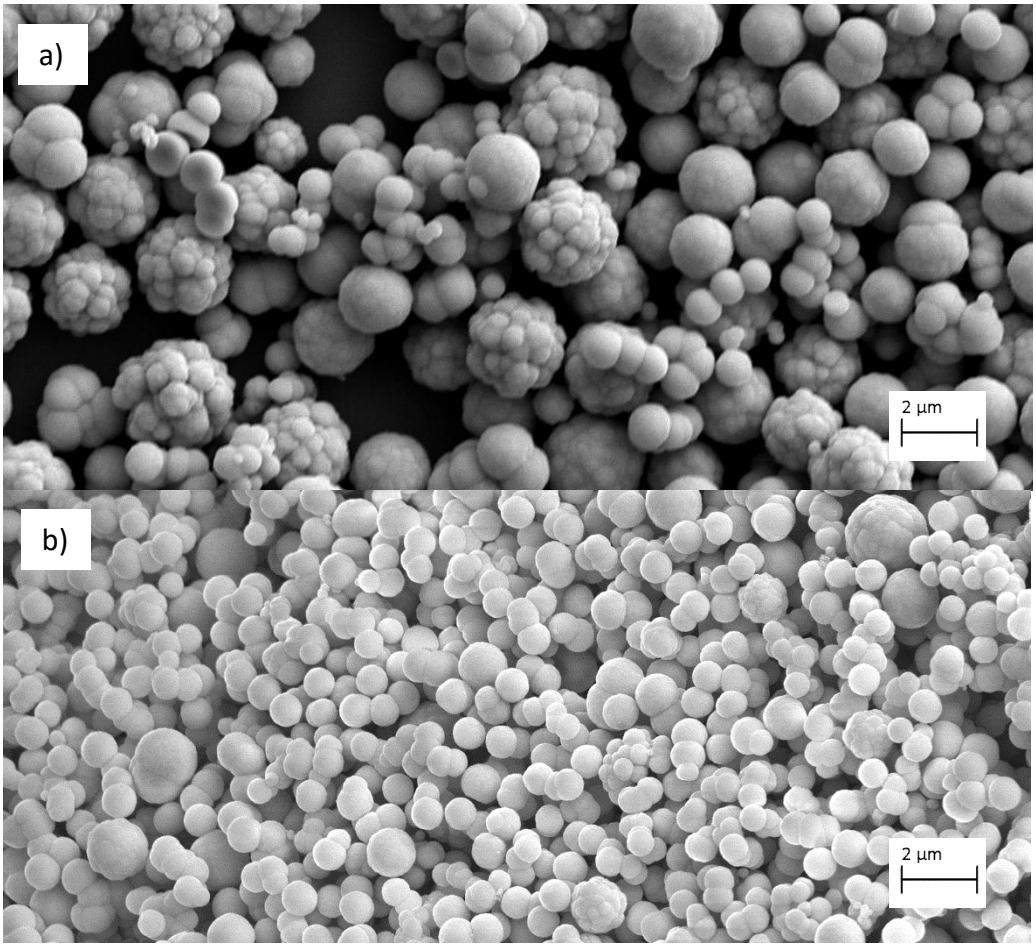

Figure 6.2: *SEM images of a) EDTA RP and b) PA RP; Each was taken at 10 kV at a magnification of 10,000x at a working distance of approximately 7 mm.*

The particles in each case were between spherical and 'cauliflower-like' in each case, with the larger particles being more 'cauliflower-like'. The EDTA RP had a much larger distribution of particle sizes between approx. 0.2 µm and 2 µm, with many of the larger 2 µm sized particles. The PA RP, on the other hand, was generally much smaller, with the largest being 1.5 µm, and the majority falling around the 0.5 µm range. This size difference made sense given the relative reaction speeds observed for EDTA and PA in the aggregation test, with PA changing colour much more quickly than EDTA. The PA aggregation mixture turned yellow-orange within the first minute of mixing, while the EDTA mixture took almost 10 minutes to change to a yellowish colour. The effect this difference ultimately had on solar cell performance was unknown, but if the RP incorporated into the film in some way, it would be favourable for the particles to be as small as possible to enable a compact film.

SEM-EDS was used to investigate the elemental composition of the EDTA and PA RPs, and the results are shown in *Table 6.1*.

Table 6.1: *SEM-EDS results of RPs of EDTA and PA; Values are shown first as a weight percentage of each element, then as a relative abundance (RA) of atoms (with Sb set as the baseline at a value of 2, to enable easy comparison of Sb_2S_3 ratios). Values were averaged over at least 4 measurements in different locations.*

Sample	**Sb (wt%)**	**S (wt%)**	**O (wt%)**	**C (wt%)**	**N (wt%)**	**Na (wt%)**
EDTA RP	69	24	2.8	3.7	0.24	0.17
PA RP	65	21	4.1	10	0.00	0.32
Sample	**Sb (set at 2)**	**S (RA)**	**O (RA)**	**C (RA)**	**N (RA)**	**Na (RA)**
EDTA RP	2.0	2.6	0.61	1.1	0.06	0.03
PA RP	2.0	2.4	0.96	3.2	0.00	0.05

The PA RP had a lower incorporation of S than the EDTA RP, as well as having a higher C and O content. The amount of carbon in both samples was quite high, with a larger atomic abundance of C in the PA sample than any other element. This suggested that the RP was not fully Sb_2S_3 but also had some incorporation of precursors and/or additives. Incorporation of C was seen for both the standard and EDTA films in *Table 4.1* and *Table 4.2*, suggesting that this was most likely common to all Sb_2S_3 formed from the precursors potassium antimony tartrate [PAT] and sodium thiosulfate [STS], and that the C came at least partially from these precursors. However, the larger amount in the PA sample suggested a difference in the deposition process, or perhaps PA itself getting trapped in the film.

TGA was used to examine the thermal degradation properties of the EDTA RP, and the results are shown in *Figure 6.3*. The key features are the mass drops around 250 °C and 600-800 °C. The dip at 250 °C corresponded to a loss of excess sulfur, while the drop from 600-800 °C corresponded to a decomposition of Sb_2S_3[4]. This matched the expected behaviour of Sb_2S_3, giving further evidence of the identity of the red RP.

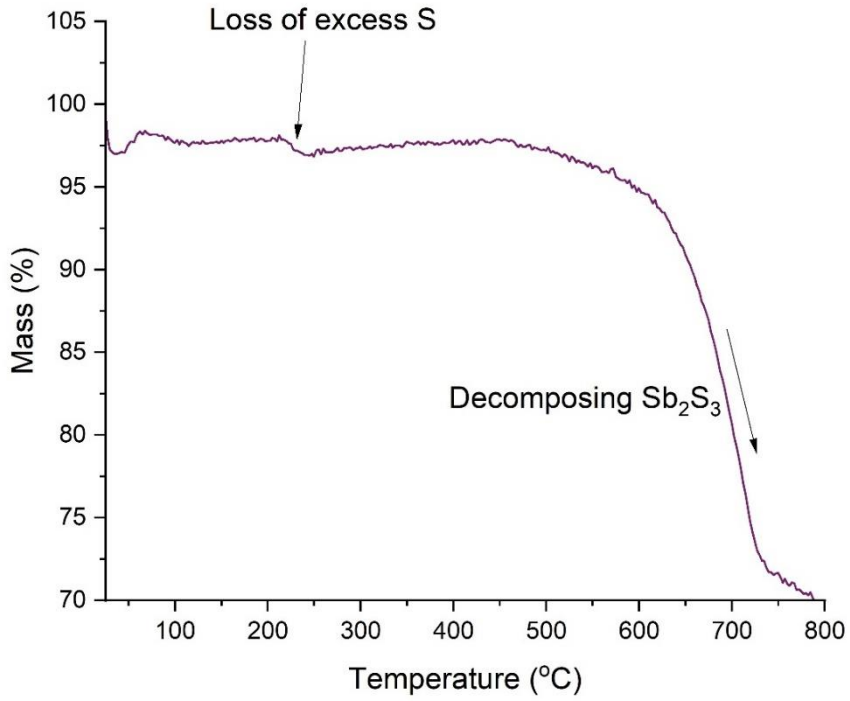

Figure 6.3: *TGA of EDTA RP, heated at 10 °C/min in air.*

The powder formed after TGA analysis had undergone a colour change from red to black, which was the same change observed for the Sb_2S_3 films during annealing, suggesting that the Sb_2S_3 had crystallised. Some EDTA RP was annealed under nitrogen at 350 °C for 10 minutes (same procedure as films), and it also turned black. The black powder was measured in P-XRD and the result is shown in *Figure 6.4*. It matched the standard for Sb_2S_3 exactly, giving yet further evidence that the red RP was amorphous Sb_2S_3.

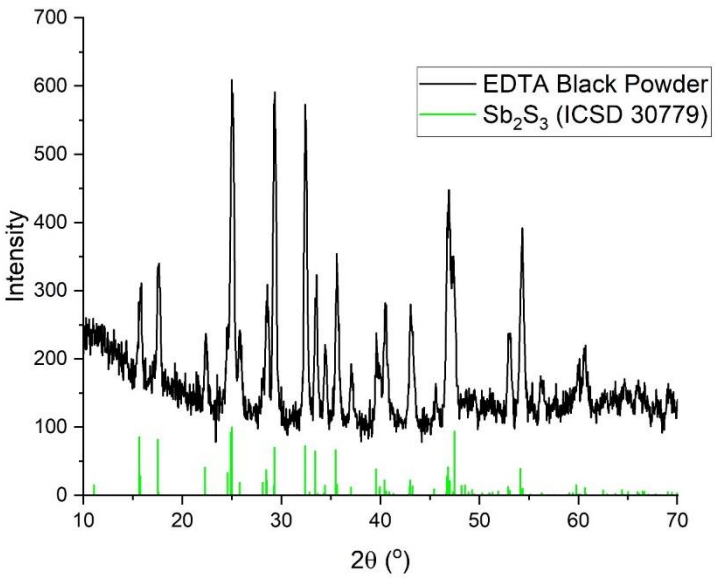

Figure 6.4: *P-XRD of black EDTA powder, formed by annealing EDTA RP under nitrogen at 350 °C for 10 mins; ICSD standard for Sb_2S_3 is shown as stick diagram (collection code 30779)[5].*

In addition to the prior powder X-ray diffraction (P-XRD) results shown in *Figure 4.13.b* and *Figure 5.2*, and X-ray fluorescence (XRF) results shown in *Section 4.3.2*, these results clearly proved that the red RP was amorphous Sb_2S_3 (with some organic contaminants), and the white RP was Sb_2O_3. The red RP consisted of spherical 'cauliflower-like' nanoparticles which were approximately 1 μm in size, though different additives yielded various sizes based, likely based on the rate of formation.

6.2. Effects of Additive pH

The acidic additives EDTA, NTA, PA, TETAH, LTA, DGA and NTMP formed a red RP (Sb_2S_3), while the basic 1111E, TEA and ED formed white RP (Sb_2O_3). This suggested that the pH of the additive was the primary reason why these RPs formed. Additionally, the formation of a red RP correlated to high performance, while the white RP correlated to low performance versus the standard, so investigating these correlations was of great importance for confirming the mechanisms by which the additives worked. In order to do so, three additional acids were added to the testing set, with the aim of having some additives with high acidity, but weaker chelation ability.

6.2.1. Testing of Additional Acids

The details of the three additional acidic additives are shown in *Table 6.2*. Acetic acid (AA), phosphoric acid (PHA) and hydrochloric acid (HCl) were chosen to have a selection of additives which were acidic, but had less chelation ability than those tested thus far.

Table 6.2: *Names, short names, key structural features and chemical structure of additional acidic additives.*

Additive Name	Short Name	Structural Features	Chemical Structure
Acetic acid	AA	Single -COOH group	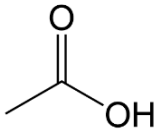
Phosphoric acid	PHA	Single PO_4H_3 group	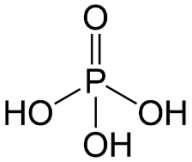
Hydrochloric acid	HCl	No chelating groups, strong acid	

These acids were first tested using the aggregation test (*Section 3.2*), whereby the additives were mixed with the Sb_2S_3 precursors and left in ambient conditions. The results are shown in *Figure 6.5*.

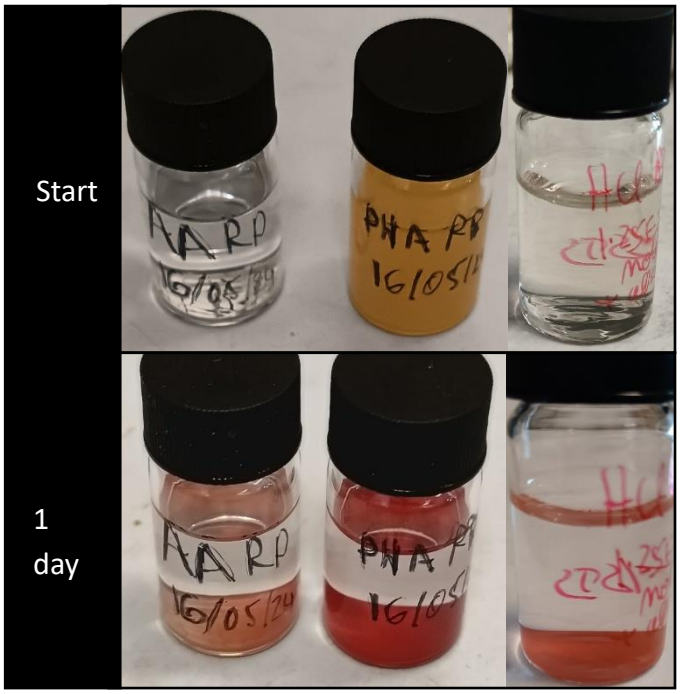

Figure 6.5: *Results of solution-based aggregation test for additives AA, PHA and HCl.*

The PHA sample almost instantly changed to a cloudy orange suspension, which was similar to the state seen for other red RP additives after a few minutes. AA and HCl both formed the red powder, but not as deeply coloured as PHA, likely due to the size and amount of Sb_2S_3 nanoparticles formed. It seemed, therefore that acidity did in fact cause the formation of the red amorphous Sb_2S_3 powder. These additives also displayed the same Sb_2O_3 suppression present in the other additives, shown by measuring the P-XRD spectra of Sb_2S_3 films deposited using the additives. The results are shown in *Figure 6.6*.

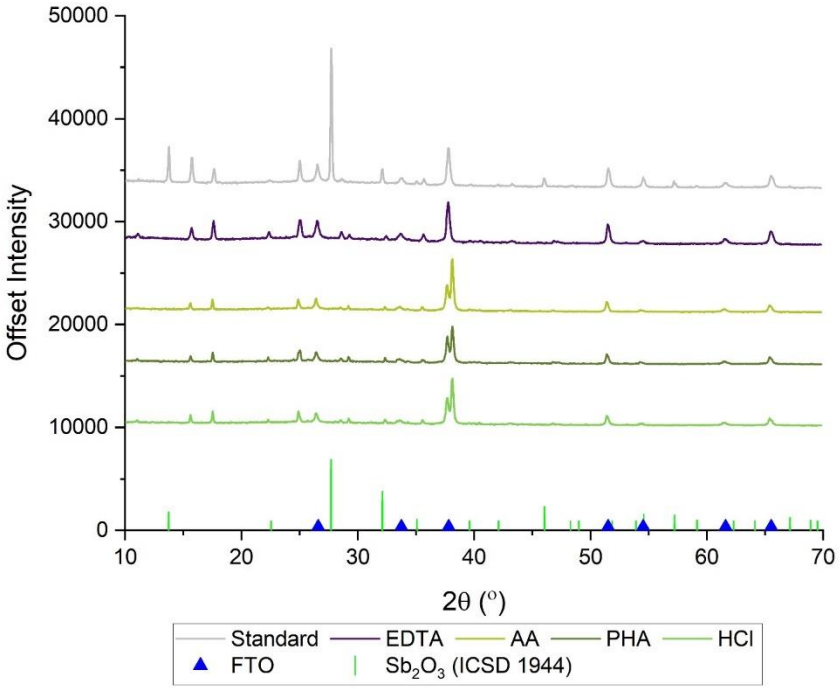

Figure 6.6: *P-XRD of Sb_2S_3 films deposited using additives AA, PHA and HCl; compared with equivalent standard (no additive) and EDTA films, and with standards for Sb_2O_3 (ICSD collection code 1944) and FTO (measured internally).*

Next, Sb_2S_3 solar cells were fabricated using AA, PHA and HCl. The current density-voltage (JV; *Section 3.4.1*) curves are shown in *Figure 6.7*, and the cell statistics are shown in *Figure 6.8*.

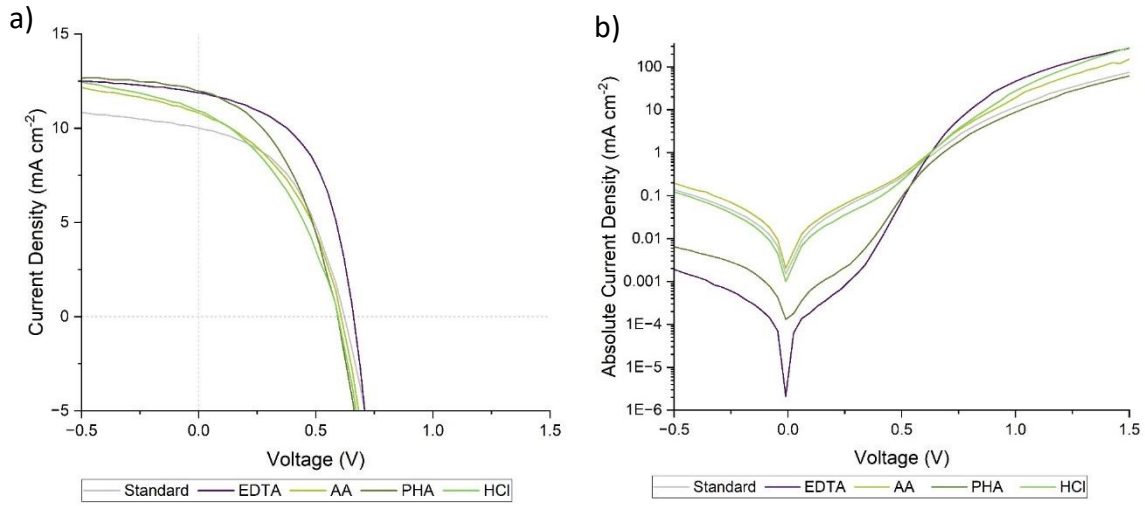

Figure 6.7: *JV curves of champion Sb_2S_3 solar cells fabricated using additives AA, PHA and HCl; compared with standard (no additive) and EDTA for a) light (AM1.5G, 100 mW cm^{-2}) and b) dark conditions.*

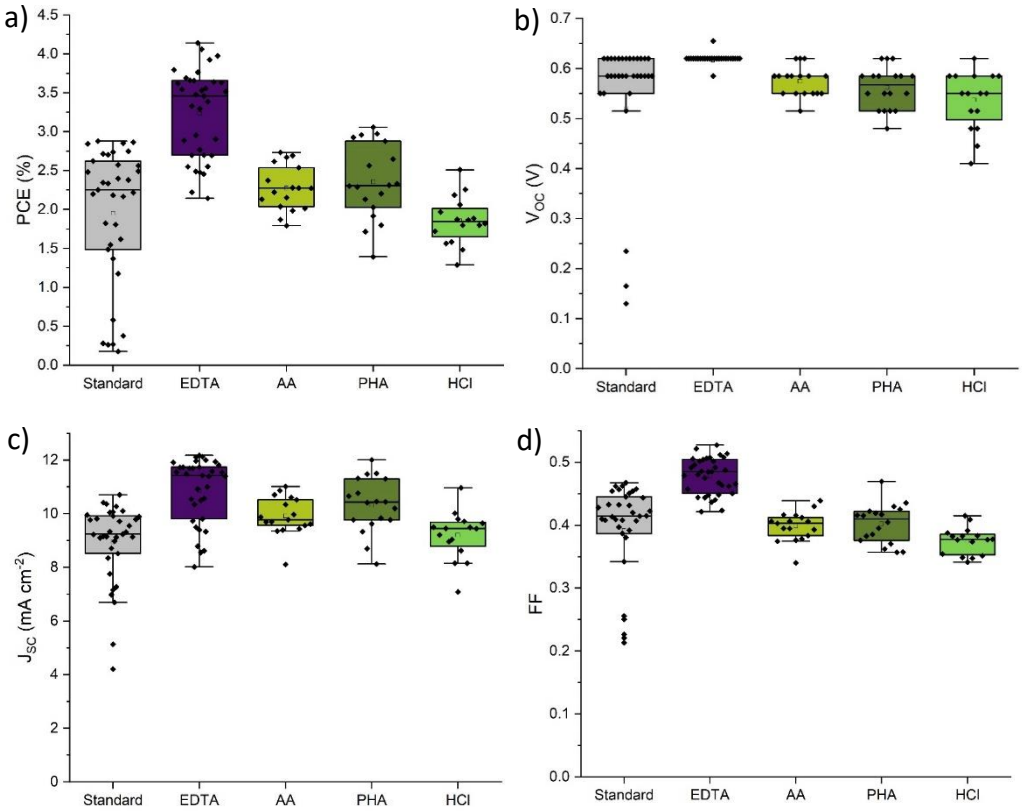

Figure 6.8: *Statistics for cell performance characteristics a) PCE, b) V_{OC}, c) J_{SC} and d) FF of Sb_2S_3 solar cells made using no additive (standard), EDTA, AA, PHA and HCl; 6 cells were tested for standard and EDTA, and 3 were tested for each other additive, made in a total of 6 experimental runs. Each cell had 6 pixels, giving a total of 36 pixels for standard and EDTA, and 18 for the other additives. Shunted pixels did not yield photovoltaic performance and so were excluded. In total, one pixel of the standard, EDTA and AA, and two pixels of HCl were fully shunted and thus excluded from the results.*

The corresponding performance metric values are also shown in *Table 6.3*.

Table 6.3: *Champion and average cell performance characteristics of PCE, V_{OC}, J_{SC} and FF with standard deviations for standard cell and cells made with EDTA, PHA, AA and HCl.*

Additive	**PCE (%) champion, (average ±s.d.)**	**V_{OC} (V) champion, (average ±s.d.)**	**J_{SC} (mA cm^{-2}) champion, (average ±s.d.)**	**FF champion, (average ±s.d.)**
Standard (none)	2.88 (1.95 ±0.9)	0.62 (0.52 ±0.2)	10.1 (8.94 ±2)	0.46 (0.39 ±0.08)
EDTA	4.14 (3.23 ±0.6)	0.66 (0.62 ±0.02)	12.1 (10.9 ±1)	0.52 (0.48 ±0.03)
AA	2.73 (2.27 ±0.3)	0.62 (0.57 ±0.03)	10.9 (9.91 ±0.7)	0.41 (0.40 ±0.02)
PHA	3.06 (2.36 ±0.5)	0.59 (0.56 ±0.04)	12.0 (10.3 ±1)	0.44 (0.40 ±0.03)
HCl	2.51 (1.85 ±0.3)	0.59 (0.54 ±0.06)	11.0 (9.20 ±0.9)	0.39 (0.37 ±0.02)

The acidic additives AA, PHA and HCl did not perform as well as the other additives tested in *Chapter 5*. In the case of HCl, it performed on average worse than the standard, with an average PCE of 1.85 ±0.3% compared to the 1.95 ±0.9% of the standard. However, with all of the red RP forming additives, the J_{SC} was increased from the standard; the champion J_{SC} values for AA and HCl were almost 1 mA cm^{-2} above. In contrast to the previous additives, however, the fill factor let the performance down, with it being about the same for AA, PHA HCl and the standard on average.

It appeared, therefore, that the formation of amorphous Sb_2S_3 in the aggregation test corresponded to an increase in the J_{SC} of the final cell. From *Figure 6.5*, it can be clearly seen that PHA was the most prominent additive of the three for forming the Sb_2S_3 powder, and it also had the highest increase in solar cell J_{SC}, reaching 12.0 mA cm^{-2} in its champion cell, and 10.3 ±1.0 mA cm^{-2} on average, almost on par with EDTA's 12.1 mA cm^{-2} and 10.9 ±1.2 mA cm^{-2} for champion and average, respectively.

6.2.2. Correlation of Cell Performance and pH of Additive

In order to clearly see the relationship between the pH of the additive and the performance of that additive in Sb_2S_3 solar cells, the pH of each additive was measured using a pH probe (*Section 3.3.8*) in a solution of deionised water, at the same concentration used in fabricating the solar cells and performing the aggregation test (2.5 mM). The results are shown in *Table 6.4*.

Table 6.4: *pH of additives; measured using a pH probe in deionised water at 2.5 mM concentration.*

Additive	pH of solution
EDTA	3.8
NTA	3.4
PA	3.5
TETAH	3.5
LTA	3.7
DGA	3.7
NTMP	3.5
1111E	9.1
TEA	8.7
ED	9.6
AA	4.7
PHA	3.9
HCl	2.6

These values were plotted against the average PCE achieved for Sb_2S_3 solar cells using those additives in order to clearly see any relationship. The results are shown in *Figure 6.9*.

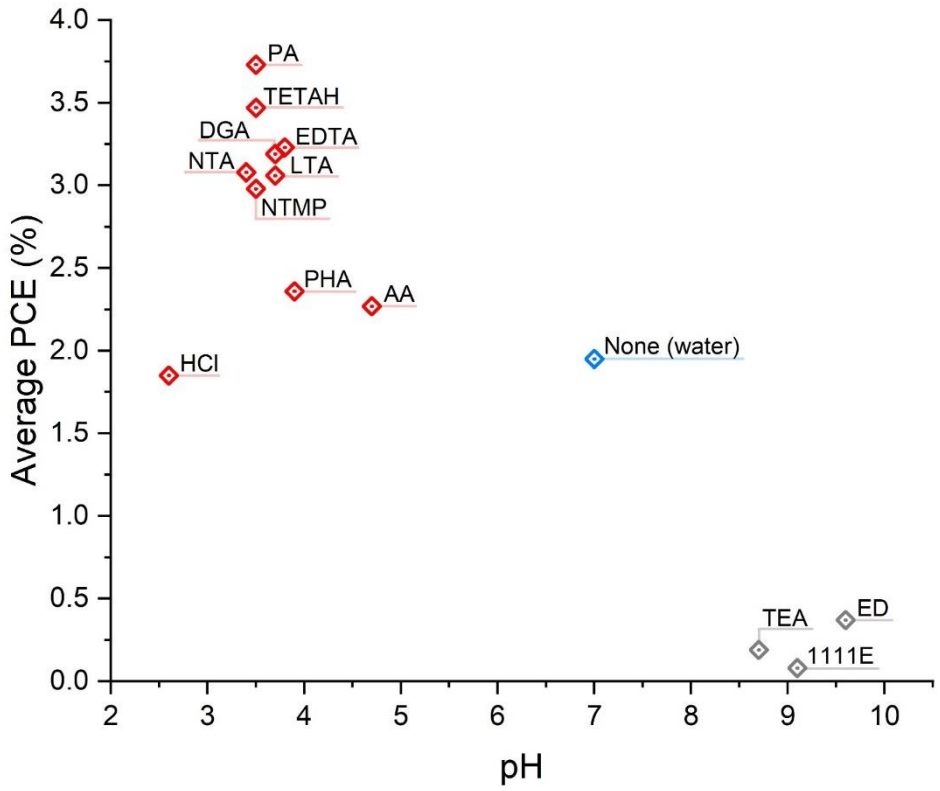

Figure 6.9: *Relationship between pH of 2.5 mM solution of an additive and its average PCE in Sb_2S_3 solar cells; the standard cell (no additive) is marked as None (water), as the equivalent solution for the standard would simply be water.*

It is evident that the high pH additives which formed white Sb_2O_3 in the aggregation test performed much more poorly than the standard, while almost all of the low pH additives which formed red Sb_2S_3 in the aggregation test performed better than the standard. HCl was an outlier in the low pH additives, and this is explored in *Section 6.2.3.* There is also some variation overall in the performance of the low pH additives, which is explored in *Section 6.2.4*.

6.2.3. Proposed Chemical Mechanisms

Using the knowledge that pH was playing a part in controlling Sb_2O_3 formation, this thesis proposes a set of mechanisms for the suppression of Sb_2O_3 during hydrothermal synthesis by acidic additives. It begins with the release of reactive sulfur species H_2S from STS in the presence of acid[6] (*Equation 6.1*), followed by the hydrolysis of Sb_2O_3 in the presence of acid[7] (*Equation 6.2*), and finally the combined reaction of $Sb(OH)_2^+$ and H_2S to form Sb_2S_3, which we observe as the red RP (*Equation 6.3*).

$$S_2O_3^{2-} + 2\ H^+ \rightleftharpoons H_2S + SO_3 \qquad \textit{(Equation 6.1)}$$

$$Sb_2O_3 + H_2O + 2\ H^+ \rightleftharpoons 2\ Sb(OH)_2^+ \qquad \textit{(Equation 6.2)}$$

$$2\ Sb(OH)_2^+ + 3\ H_2S \rightarrow Sb_2S_3 + 4\ H_2O + 2\ H^+ \qquad \textit{(Equation 6.3)}$$

PAT is known to decompose into Sb_2O_3 and so would act as the source of Sb_2O_3[8]. At high pH, *Equation 6.2* illustrates that Sb_2O_3 will be the predominant form over the more soluble $Sb(OH)_2^+$, as an abundance of OH^- will push the equilibrium to the left, leading to a white precipitate of Sb_2O_3, which was seen as the white RP. At low pH, the soluble $Sb(OH)_2^+$ form dominates. Since the $Sb(OH)_2^+$ is also being removed from solution through conversion to Sb_2S_3, as in *Equation 6.3*, the equilibrium continually converts any remaining Sb_2O_3 to $Sb(OH)_2^+$, leading to a suppression of Sb_2O_3 as a whole by forming a precipitate of Sb_2S_3, which was seen as the red RP.

To investigate whether these mechanisms were logical, the pH of some mixed precursor and acid solutions were measured before and after being allowed to react. PA was chosen as the acid, as it was more easily soluble than EDTA and performed very well in solar cells. A solution of STS and PA behaved as expected. The pH increased from 3.9 to 4.3 over one day, which agrees with the consumption of H^+ illustrated in *Equation 6.1*. Unexpectedly, a solution of PAT and PA became more acidic over the same time period, with the pH changing from 3.9 to 3.7. This change was likely due to the release of tartaric acid upon the decomposition of PAT[4]. A solution of all three of STS, PAT and PA yielded a larger pH increase than for STS and PA, going from 4.2 to 4.7. This can be explained by the removal of H_2S from solution in *Equation 6.3*. As Sb_2S_3 is formed, the equilibrium of *Equation 6.3* is disrupted, and more H_2S is formed to compensate. As such, more H^+ is consumed, raising the pH. It might be expected, therefore, that the pH rise would be even higher than it was, however, the negative pH change seen due to the formation of tartaric acid from PAT would have reduced the final pH.

In literature, multiple examples of acidic additives suppressing Sb_2O_3 can be found, though none of them suggest the above mechanism as being the reason why. One such example is phosphotungstic acid, used in Sb_2S_3 solar cells by Chen *et al.* for the suppression of Sb_2O_3[9]. They explore the trends of acidity and oxidation potential, but do not propose a mechanism for their operation, or explain why these effects are important. In a different example thioacetamide (TA), another acidic reagent, was used in conjunction with STS as a dual sulfur source for Sb_2S_3 solar cells by Xiao *et al*. and was again observed to suppress Sb_2O_3 formation[10]. They explain their reasoning well with a boosted S^{2-} release mechanism, though the mechanism proposed above likely also played a role, as in their study Sb_2O_3 formation was significantly reduced whenever STS was used in conjunction with the acidic TA. In another example, Sb_2O_3 was even used as an Sb precursor when Chen *et al.* used $Al_2(SO_4)_3$ and EDTA-2Na, both of which are acidic to some degree[7]. It was this work which proposed *Equation 6.2*, though any conversion to Sb_2S_3 was not mentioned. Therefore, with this newly proposed mechanism, the formation and suppression of Sb_2O_3 in Sb_2S_3 solar cells can be more deeply understood, and this logic can even be combined with the understanding of prior works.

The one outlier to the trend of performance vs pH highlighted in *Figure 6.9* was HCl. This was likely due to a side reaction observed during the aggregation test, whereby the HCl sample turned a faint light-yellow colour prior to forming the red Sb_2S_3 RP, a colour which was lighter than was observed for any other additive, and which persisted for some minutes. This indicated the formation of elemental sulfur, which is consistent with the common reaction shown in *Equation 6.4*.

$$Na_2S_2O_3\,(s) + 2\,HCl\,(aq.) \rightarrow 2\,NaCl\,(aq.) + H_2O\,(l) + SO_2\,(g) + S\,(s) \qquad (Equation\ 6.4)$$

This reaction, therefore, would remove useable sulfur from the solution as a solid, negatively impacting the Sb:S ratio in the final film, which would affect performance due to the introduction of vacancy defects, which can act as recombination centres. This reaction occurs and is catalysed by H^+, so the question occurs as to why it would not occur for the other acidic additives. In fact, it is likely that it does, however it may be a kinetically driven reaction, requiring a large concentration to occur noticeably. Due to HCl being a strong acid, the pH of

HCl is almost 1 lower than the weaker acids at the same concentration. This means there are approximately ten times the H^+ ions in the HCl aggregation test solution, and the sulfur-forming reaction can occur at a noticeable level. In the weak acid aggregation test solutions, the reaction to form Sb_2S_3 precipitate may be thermodynamically favoured, so occurs more noticeably at lower acidity. This would explain why eventually, after the HCl aggregation test solution sat as yellow and turbid, it eventually transitioned to a red colour like the other additives. The final colour of the HCl red RP also more closely matched AA (*Figure 6.5*), which was the highest pH of the acidic additives. This makes sense if the majority of the available H^+ was instead used to form bright yellow elemental sulfur, instead of the deep red Sb_2S_3. Therefore, in order to suppress Sb_2O_3, a balance of pH must be struck, whereby it is low enough to convert Sb_2S_3 to Sb_2O_3, but not so low that it forms elemental sulfur, which detriments solar cell performance.

6.2.4. Effects of RP on Cell Performance

The formation of the red Sb_2S_3 powder by the addition of an acidic additive was correlated with higher performance in Sb_2S_3 solar cells, however, it was still unclear whether the Sb_2S_3 powder was incorporating into the film, acting as a source of precursors, or reducing the available resources for film formation. To test this, three scenarios were compared:

1) A regular Sb_2S_3 solar cell made using EDTA as an additive
2) A standard EDTA cell, as above, for which the mixed hydrothermal solution of STS, PAT and EDTA was left in ambient conditions for a day, and then the substrate was added and hydrothermal synthesis proceeded as normal (‘settled’).
3) A settled solution which, for the hydrothermal synthesis, used only the liquid decanted from the top of the settled solution, thereby removing the red powder which had formed (‘settled+filtered’).

The cell performance statistics of the solar cells fabricated for these three scenarios are shown in *Figure 6.10*.

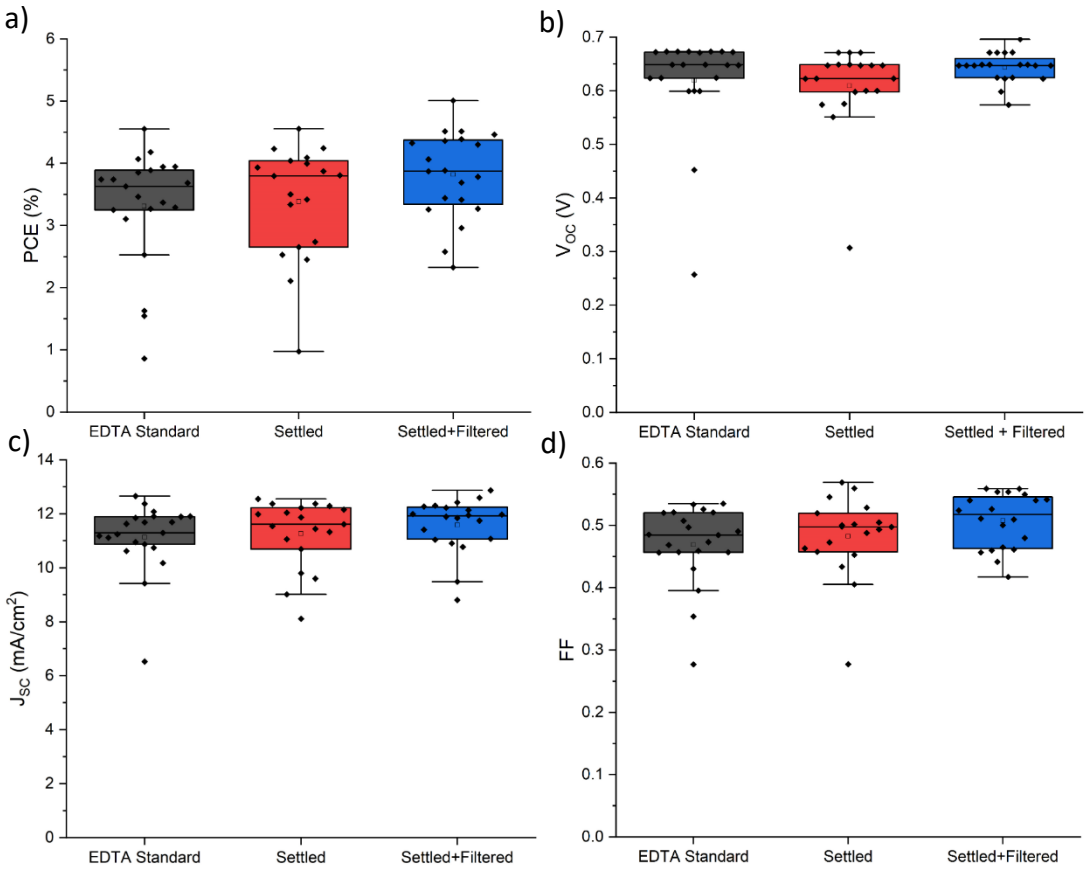

Figure 6.10: *Performance statistics a) PCE, b) V_{OC}, c) J_{SC} and d) FF for solar cells fabricated using EDTA as an additive, with different conditions of precursor solution; Three scenarios are presented: 1) 'EDTA standard' with no change, 2) 'settled', whereby the aggregation of Sb_2S_3 in the mixed precursor and additive solution was allowed to proceed over a day before the hydrothermal mixture was used, and 3) 'settled+filtered', whereby after creating a 'settled' solution the liquid was extracted and only that liquid was used for hydrothermal synthesis, effectively removing the aggregate. 4 cells were made for each condition, made in a total of 3 experimental runs. Each cell had 6 pixels, totalling 24 pixels per scenario. A total of 3 pixels for the EDTA standard, 5 pixels for settled and 4 pixels for settled+filtered were shunted and gave no photovoltaic performance and thus were excluded from the analysis.*

The performance of the cells overall was unchanged by the presence of the precipitate, with the average PCE (± standard deviation) for the EDTA standard being 3.31 ±0.9%, and the settled being 3.38 ±0.9%. Additionally, the champion values were the same at 4.55%. This suggested that the presence of the Sb_2S_3 had very little effect on the film process, though the settled scenario had five total shunted cells while EDTA standard only had three, so the

reproducibility may have been affected by the presence of the powder. The V_{OC} stayed very similar as well, with 0.62 ±0.09 V for the EDTA standard and 0.61 ±0.08 V for the settled. The FF also stayed largely the same, with averages of 0.47 ±0.06 and 0.48 ±0.06. The J_{SC} had only a slight increase from 11.1 ±1 mA cm^{-2} to 11.3 ±1 mA cm^{-2}, a difference which fell well within standard deviation; thus, the difference is likely not significant.

The settled and filtered sample, on the other hand, was interesting as the performance was clearly improved from both other scenarios, with an average PCE of 3.82 ±0.7% and a champion of 5.01%. This was due to an increase in all three of V_{OC} (average 0.64 ±0.03 V), FF (average 0.51 ±0.04) and J_{SC} (average 11.6 ±1 mA cm^{-2}).

So, the formation and then removal of the Sb_2S_3 particulate not only still allows for the formation of an Sb_2S_3 film, but in fact improves the end result. This may be due to the fact that the prior two scenarios would largely end with the same result; loose Sb_2S_3 particulate in solution during deposition. The EDTA standard would still form the precipitate, but over the course of hydrothermal synthesis instead of prior to it. The settled has already formed it, but it is present in solution and may cause the same potential problems as it would in the EDTA standard, such as incorporating large particles into the film instead of individual Sb/S ions. By allowing the precipitate to form and then removing it, the precursors which are actually forming the film (i.e. not the Sb or S now incorporated into an aggregate, but that bound to EDTA, etc or free in solution) are able to form the film more effectively.

6.3. Effects of Chelating Functional Groups

Within the low pH, red RP-forming additives, there was a lot of variation in performance. HCl was poorly performing due to a side reaction, but the other additives, which did not have any obvious side reactions, also had varied performance. These differences were instead attributed to the ability of the additive to bind to and chelate Sb^{3+} in solution. This was the originally proposed mechanism for the operation of EDTA as an additive[1], and it has been shown that by reducing the available Sb^{3+} in the hydrothermal deposition solution, favourable film quality can be achieved[1, 11]. Therefore, whichever additive can most effectively chelate and hold on to Sb^{3+} in solution should improve the film quality the most. Oxygen has a strong affinity for Sb^{3+}, so deprotonated carboxylic and phosphoric acids are well suited to binding to

Sb^{3+}. *Figure 6.11* shows the correlation between the number of oxygen atoms in the additive which are able to potentially bind to Sb, and the performance of said additive in Sb_2S_3 solar cells. It assumes full deprotonation of the acid groups, with only one O atom of each group involved in binding. OH groups are not included, as they would be unlikely to be deprotonated at the low solution pH in the compounds listed, and so would not contribute greatly to the chelation ability[12].

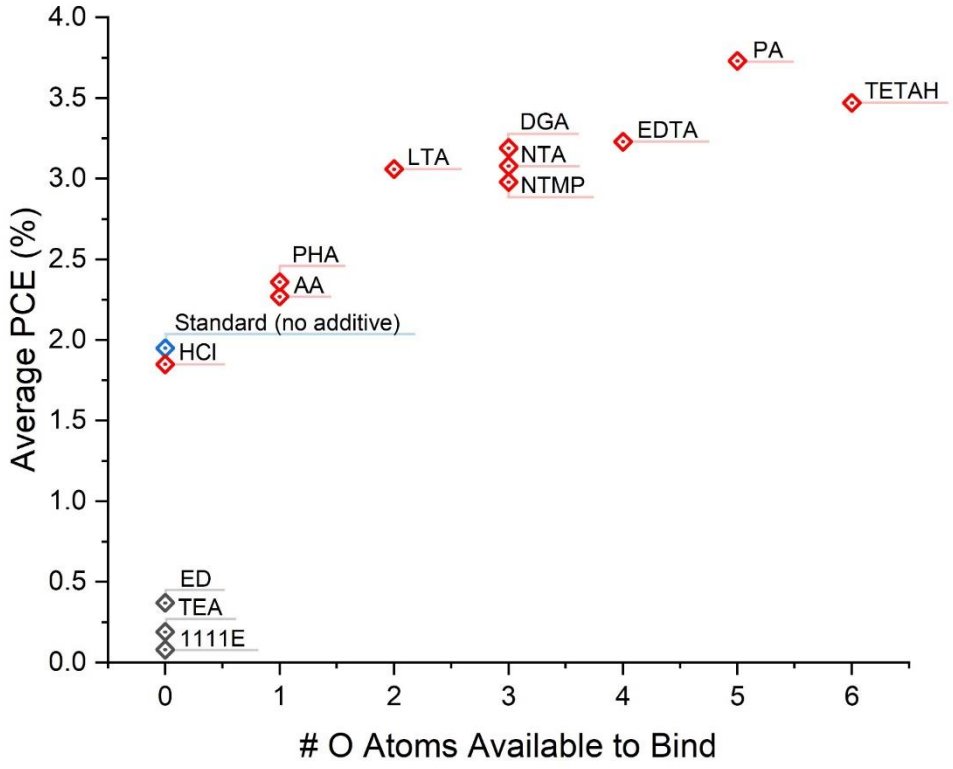

Figure 6.11: *Number of oxygen atoms on additive available to bind to Sb^{3+} vs the average PCE of Sb_2S_3 solar cells made using that additive.*

It is clear to see that going from HCl, which has no oxygens capable of binding to Sb^{3+}, to TETAH, which has 6 such atoms, the PCE steadily increases with some slight variation, with a noticeable jump from having only one to multiple available O atoms. Multiple O atoms available to bind allow for chelation, greatly strengthening the binding overall. This trend indicates that both the pH and ability of the additive to bind to and thus restrict Sb^{3+} availability play a tandem role in improving efficiency.

6.4. Conclusions

Overall, through detailed study of the mechanisms behind the operation of EDTA and the study of similarly structured additives, a promising mechanism was found for the conversion of insulating Sb_2O_3 to Sb_2S_3 in the hydrothermal solution of PAT and STS through pH control. At low pH, the Sb_2O_3 becomes hydrolysed, and reacts with H_2S, which forms from STS in an acidic medium, to form Sb_2S_3. This greatly improved cell efficiencies by reducing potential charge trap sites from Sb_2O_3. Additionally, the raising of the pH caused the hydrolysed $Sb(OH)_2^+$ to crash out of solution as Sb_2O_3. This then incorporated into the film and caused the performance of the solar cell to plummet by introducing new trap sites. The control of pH, therefore, is of great importance in the hydrothermal synthesis of Sb_2S_3.

6.5. References

1. Wang, X.; Tang, R.; Jiang, C.; Lian, W.; Ju, H.; Jiang, G.; Li, Z.; Zhu, C.; Chen, T., Manipulating the Electrical Properties of $Sb_2(S,Se)_3$ Film for High-Efficiency Solar Cell. *Advanced Energy Materials* **2020,** *10* (40), 2002341.

2. Diliegros Godines, C.; Santos, J.; Mathews, N.; Pal, M., Effect of Ag Doping on Structural, Optical and Electrical Properties of Antimony Sulfide Thin Films. *Journal of Materials Science* **2018,** *53*.

3. Sui, Z.; Hu, S.; Chen, H.; Gao, C.; Su, H.; Rahman, A.; Dai, R.; Wang, Z.; Zheng, X.; Zhang, Z., Laser Effects on Phase Transition for Cubic Sb_2O_3 Microcrystals under High Pressure. *Journal of Materials Chemistry C* **2017,** *5* (22), 5451-5457.

4. Huang, Y.; Tang, R.; Wang, G.; Li, G.; Che, B.; Wang, Y.; Lian, W.; Zhu, C.; Chen, T., Chemical Insight into the Hydrothermal Deposition of $Sb_2(S,Se)_3$ Towards Delicate Microstructure Engineering. *Journal of Materials Chemistry A* **2022,** *10* (18), 9892-9901.

5. Šćavničar, S., The Crystal Structure of Stibnite. A Redetermination of Atomic Positions. **1960,** *114* (1-6), 85-97.

6. Pryor, W. A., The Kinetics of the Disproportionation of Sodium Thiosulfate to Sodium Sulfide and Sulfate. *Journal of the American Chemical Society* **1960,** *82* (18), 4794-4797.

7. Zhang, L.; Xiao, P.; Che, B.; Yang, J.; Cai, Z.; Wang, H.; Gao, J.; Liang, W.; Wu, C.; Chen, T., Mechanistic Study of the Transition from Antimony Oxide to Antimony Sulfide in the Hydrothermal Process to Obtain Highly Efficient Solar Cells. *ChemSusChem* **2023,** *16* (7), e202202049.

8. Reddy, J. R.; Ravi, G.; Suresh, P.; Veldurthi, N. K.; Velchuri, R.; Vithal, M., Antimony Potassium Tartrate. *Journal of Thermal Analysis and Calorimetry* **2014,** *115* (2), 1321-1327.

9. Zhang, Y.; Li, S. a.; Tang, R.; Wang, X.; Chen, C.; Lian, W.; Zhu, C.; Chen, T., Phosphotungstic Acid Regulated Chemical Bath Deposition of Sb_2S_3 for High-Efficiency Planar Heterojunction Solar Cell. *Energy Technology* **2018,** *6* (11), 2126-2131.

10. Wang, S.; Zhao, Y.; Che, B.; Li, C.; Chen, X.; Tang, R.; Gong, J.; Wang, X.; Chen, G.; Chen, T.; Li, J.; Xiao, X., A Novel Multi-Sulfur Source Collaborative Chemical Bath Deposition Technology Enables 8%-Efficiency Sb_2S_3 Planar Solar Cells. *Advanced Materials* **2022,** *34* (41), 2206242.

11. Chen, X.; Che, B.; Zhao, Y.; Wang, S.; Li, H.; Gong, J.; Chen, G.; Chen, T.; Xiao, X.; Li, J., Solvent-Assisted Hydrothermal Deposition Approach for Highly-Efficient $Sb_2(S,Se)_3$ Thin-Film Solar Cells. *Advanced Energy Materials* **2023,** *13* (21), 2300391.

12. Silva, A. M. N.; Kong, X.; Hider, R. C., Determination of the Pka Value of the Hydroxyl Group in the A-Hydroxycarboxylates Citrate, Malate and Lactate by 13C NMR: Implications for Metal Coordination in Biological Systems. *BioMetals* **2009,** *22* (5), 771-778.

7. Conclusions and Future Work

In this thesis, ethylenediaminetetraacetic acid (EDTA) was shown to improve the efficiency of Sb_2S_3 solar cells prepared on the benign electron transport layer of TiO_2, similarly to how it had improved efficiency for the leading $Sb_2(S, Se)_3$ on CdS cells. In addition, however, a suppression of Sb_2O_3 formation by EDTA was observed for the first time. This suppression of Sb_2O_3 was also accompanied with the formation of a red powder while in solution with the precursors potassium antimony tartrate (PAT) and sodium thiosulfate (STS). By using this red powder formation as a screening process to find new additives, it was discovered that additional additives such as diglycolic acid (DGA) and pentetic acid (PA) also formed this red powder. The use of this screening process enabled the discovery of a range of additives, almost all of which surpassed the standard (no additive) cell efficiency. A few, such as PA, even exceeded the established EDTA.

Due to the success of the powder formation as a screening process, the powder itself was more deeply investigated, and was found to be amorphous Sb_2S_3. This suggested that the process by which Sb_2O_3 was being suppressed was creating amorphous Sb_2S_3 as a byproduct. Due to the acidic nature of many of the successful additives, pH testing of each additive was used to determine the effects of pH on performance, and to determine a mechanism for the observed Sb_2O_3 suppression. The low pH additives correlated directly with higher performance than the standard, and the formation of amorphous Sb_2S_3 when the additive was in solution with STS and PAT, while a high pH additive instead yielded Sb_2O_3 powder and poor performance. Through this, a potential mechanism was developed involving the release of H_2S from STS, followed by reaction of H_2S with hydrolysed Sb_2O_3 (released from PAT), through which Sb_2O_3 in solution could be converted irreversibly to Sb_2S_3. Both the hydrolysis of Sb_2O_3 and release of H_2S were promoted by the presence of acid, thus leading to the results observed whereby acidic additives promoted the conversion mechanism. Additionally, the discrepancy between the efficiencies of the low pH additives could be explained by their ability to chelate and hold onto Sb^{3+} in solution, effectively controlling the deposition of Sb_2S_3. The number of available sites on the additive which could bind to Sb^{3+} followed an almost linear relationship with the final performance of the solar cell made using the additive. As such, clear relationships were demonstrated between both the acidity and Sb chelation ability

of an additive, and its performance in solar cells prepared using the leading method of hydrothermal synthesis using PAT and STS precursors. Due to the widely applicable nature of these findings, direct lessons for the future development and design of additives for antimony chalcogenide solar cells can be taken from this thesis and applied to new and upcoming research.

In general, future additive designs should seek to balance the pH of the hydrothermal mixture carefully, in order to avoid the formation of Sb_2O_3, and to avoid potential sulfur-forming side reactions seen at very low pH. For example, a basic additive may hold quite promising theoretical benefits for the cell, but it forms Sb_2O_3 in solution. However, as presented in this thesis, this formation may be remedied through an additional acidic co-additive.

Another future endeavour may be to attempt the same 'settled and filtered' tests conducted for the red RP forming additives in *Chapter* 6, but instead for the white RP forming additives. The rationale behind this would be that if the Sb_2O_3 can be formed by allowing it to crash out of solution in ambient conditions, and then removed, perhaps some basic additives with alternate purposes could be explored without the need for a co-additive, or the deposition of Sb_2S_3 under high pH conditions could be explored without the need for additional reagents to prevent Sb_2O_3 formation.

In terms of Sb^{3+} binding capability, it was found that by increasing the amount of available oxygen atoms (thereby in theory increasing the ability of the additive to bind Sb^{3+}), the performance of the solar cell increased. This was determined to be largely due to more compact films with smaller crystal grains. However, further tests are definitely required to determine the effectiveness of this approach, and the deeper mechanisms behind it. For example, further use of NMR spectroscopy to examine the binding of additives other than EDTA to Sb^{3+} would provide further evidence for a wider set of reagents than just EDTA. Additionally, computational modelling of the favourability of Sb^{3+} binding in various additives could allow for optimisation of a structure to perform this task more effectively.

The rate of reaction in the aggregation test was not fully explored in this thesis and may also be of note. The highest performing additive, PA, had a very high rate of formation of the RP, while EDTA and TETAH were lower. The SEM images showed a smaller average particle size which may explain the improved performance if these particles were incorporating into the

film, however, the reason as to why the rate of reaction was higher is unknown and may be worthy of exploration.

While this research was conducted on Sb_2S_3 solar cells, the implications should be considered for any additive design used in antimony chalcogenide cells which are planning to use the most common and successful method of hydrothermal synthesis with PAT and STS. A careful control of pH and the availability of Sb will lead to the avoidance of the formation of Sb_2O_3 and the improvement of overall film quality, leading to efficient antimony chalcogenide solar cells.

Future researchers looking to work on this topic should also explore the opportunities presented by some additional characterisation techniques not employed in this study. For example, the use of film thickness measurement techniques including cross-sectional SEM and transmission electron microscopy (TEM) would allow for the determination of the effect of the additives on film thickness and thus given more information on the impact of the additives on the film growth process. TEM would also yield greater information on crystalline grain sizes and grain boundaries, as SEM/AFM are only surface techniques and so only see a part of the picture. X-ray photoelectron spectroscopy (XPS) could have been used to determine compositional information, including further information about the chemical states of the material, and the ratio of Sb_2O_3/Sb_2S_3 and may potentially shine some light on why the Sb:S ratio was not exactly 2:3 in our samples. Photoluminescence spectroscopy (PL) would give bandgap information, as well as insights into recombination kinetics. Finally, some form of conductivity testing to determine the impacts of the presence of Sb_2O_3 and the orientation of the antimony chalcogenide absorber would be beneficial to see to what extent these effects impact charge transport within the solar cell.

In addition to the techniques employed in this study, the techniques listed above could shine some light on not only the chemical function of the additives, but also their effect on the material and solar performance, and so future studies are urged to explore these options to gain even greater insights into the role these additives play within the antimony chalcogenide solar cell system.

Appendix 1: Publications

Establishing Design Principles for Functional Additives in Antimony Chalcogenide Solar Cells

Matthew Sutton, Prof. Tayebeh Ameri, Prof. Neil Robertson – ***J. Mater. Chem. A***, 2025, Advance Article, *available at https://doi.org/10.1039/D5TA00947B*

Additive Engineering Mechanisms for Antimony Chalcogenide Solar Cells

Matthew Sutton, Prof. Tayebeh Ameri, *publication submitted to EES Solar*

Appendix 2: Poster Presentation

Additive Engineering Mechanisms for Antimony Chalcogenide Solar Cells

Matthew Sutton, Prof. Tayebeh Ameri, Prof. Prashant Valluri, Prof. Neil Robertson, Dr. Jane Blackford

E-MRS Spring Meeting, Strasbourg 2024